

Surface states and Fermi-level pinning on non-polar binary and ternary (Al,Ga)N surfaces

Lars Freter

Information

Band / Volume 84

ISBN 978-3-95806-644-1

Forschungszentrum Jülich GmbH
Ernst Ruska-Centrum für Mikroskopie und Spektroskopie mit Elektronen (ER-C)
Physik Nanoskaliger Systeme (ER-C-1/PGI-5)

Surface states and Fermi-level pinning on non-polar binary and ternary (Al,Ga)N surfaces

Lars Freter

Schriften des Forschungszentrums Jülich
Reihe Information / Information

Band / Volume 84

ISSN 1866-1777

ISBN 978-3-95806-644-1

Bibliografische Information der Deutschen Nationalbibliothek.
Die Deutsche Nationalbibliothek verzeichnet diese Publikation in der
Deutschen Nationalbibliografie; detaillierte Bibliografische Daten
sind im Internet über <http://dnb.d-nb.de> abrufbar.

Herausgeber und Vertrieb: Forschungszentrum Jülich GmbH
Zentralbibliothek, Verlag
52425 Jülich
Tel.: +49 2461 61-5368
Fax: +49 2461 61-6103
zb-publikation@fz-juelich.de
www.fz-juelich.de/zb

Umschlaggestaltung: Grafische Medien, Forschungszentrum Jülich GmbH

Druck: Grafische Medien, Forschungszentrum Jülich GmbH

Copyright: Forschungszentrum Jülich 2022

Schriften des Forschungszentrums Jülich
Reihe Information / Information, Band / Volume 84

D 82 (Diss. RWTH Aachen University, 2022)

ISSN 1866-1777
ISBN 978-3-95806-644-1

Vollständig frei verfügbar über das Publikationsportal des Forschungszentrums Jülich (JuSER)
unter www.fz-juelich.de/zb/openaccess.



This is an Open Access publication distributed under the terms of the [Creative Commons Attribution License 4.0](https://creativecommons.org/licenses/by/4.0/), which permits unrestricted use, distribution, and reproduction in any medium, provided the original work is properly cited.

Contents

1	Introduction	5
2	Theory	9
2.1	One-dimensional tunneling effect of a single particle	10
2.2	Tunneling between materials with a different work function	13
2.3	Towards many-particle tunneling	15
2.3.1	Density of states	16
2.3.2	Bardeen approach of tunneling theory	17
2.3.3	Tersoff and Hamann approximation	20
2.4	Tunneling in semiconductors	23
2.4.1	Tip-induced band bending	24
2.4.2	Band bending due to surface states	26
2.5	Band structure and surface state position of III-nitride ($10\bar{1}0$) according to DFT calculations	29
3	Experimental setup	33
3.1	Tip preparation	33
3.2	Sample preparation	35
3.3	Scanning tunneling microscope	36
3.4	Samples	38
3.4.1	Structure of sample A3782/A3787	38
3.4.2	Structure of the LED sample	40
4	Investigation of the influence of various physical parameters on tunnel currents simulated for n-type III-nitride ($10\bar{1}0$) semiconductor surfaces	43
4.1	Introduction	44
4.2	General remarks on the simulation packages used	45
4.3	Exponential dependence of the tunnel current on the tip-sample separation	47
4.4	Effects of sample parameters on the tunnel current	50
4.4.1	Variations in the band gap	50
4.4.2	Effect of the variation in the energy of surface states	52
4.4.3	Effect of the variation in the doping concentration	53

4.4.4	Electron affinity	56
4.5	Tip specific parameters	57
4.5.1	Tip radius	58
4.5.2	Tip work function	60
4.6	Conclusion	62
5	Investigation of Fermi-level pinning induced by intrinsic and ex-	
	trinsic surface states at <i>n</i>- and <i>p</i>-type GaN (10$\bar{1}$0) surfaces	65
5.1	Experimental results	66
5.1.1	SIMS investigation	66
5.1.2	Microscopic characterization	71
5.1.3	Tunneling spectroscopy obtained at clean GaN (10 $\bar{1}$ 0) cleav-	
	age surfaces in UHV	73
5.1.4	Discussion of the origin of Fermi-level pinning	78
5.1.5	Tunneling spectroscopy on surfaces after exposure to ambient	
	conditions	80
5.2	Discussion of the effect of air exposure	85
5.3	Conclusion	89
6	Intrinsic surface states of ternary (Al,Ga)N (10$\bar{1}$0) surfaces	91
6.1	Experiment	91
6.2	Experimental results	91
6.3	Discussion	97
6.3.1	Empty surface state of (Al,Ga)N	99
6.3.2	Empty surface state of AlN	102
6.3.3	Position of the empty surface state in DFT calculations . . .	109
6.4	Conclusion	110
7	Summary	113
	Bibliography	117
	List of own publications	135
	Acknowledgment	137

Chapter 1

Introduction

The need for optical devices (optoelectronics) and lighting applications triggered a huge effort in understanding as well as tailoring the properties of semiconductor materials, in particular the band gap and the conductivity. The most promising group of materials are compound semiconductors, since their band gap can be modified over a wide range through alloying of two or more binary compounds, while controlling conductivity appropriately [1–9]. Unfortunately, in planar growth, alloying introduces large strain, due to lattice mismatch between most binary compounds [5,6,8,10]. This limits the range of band gaps accessible in practical planar growth schemes and carries the inherent danger of flipping from two to three-dimensional growth and phase separation [11–14]. Hence, strain management is inherently important and critical for device manufacturing.

An approach for accommodating larger strain in devices is taking advantage of nanostructures, such as nanowires [15–19]. Due to the small growth surfaces on the nanowires' cross-section, strain can relax over a much wider range, allowing defect-free growth of material combinations with larger lattice mismatch. Ultimately, this allows tuning the electronic properties of compound semiconductors over a much wider range [17–19].

Depending on the crystal structure of the used compound semiconductors, nanowires exhibit different types of facets. For zincblende materials, the dominant side-wall facets of (111) grown nanowires are non-polar $\{110\}$ facets with minor polar

facets [20, 21]. The III-V $\{110\}$ surfaces have been characterized exhaustively since the mid-70s, and most fundamental physics is well understood [22–27].

In contrast, the most promising compound semiconductors for lighting, the group III nitrides [28–31], preferentially crystallize in the wurtzite structure, which, however, leads to dominant non-polar $\{10\bar{1}0\}$ (called *m*-plane) and minor non-polar $\{11\bar{2}0\}$ (called *a*-plane) facets [32]. Thus far, the knowledge about these surfaces is limited to GaN [33–39], InN [33, 40], AlN [41], and a single lattice-matched ternary compound $\text{Al}_{0.8}\text{In}_{0.2}\text{N}$ [42]. Hence, a detailed understanding of the non-polar surface’s properties of ternary III-N semiconductors is lacking. Furthermore, only the surfaces of *n*-doped materials have been investigated thus far, and no knowledge exists about the properties of their *p*-doped counterparts.

Non-polar III-N surfaces also lack out-of-plane polarization fields [43–45], which makes them attractive for polarization-free growth [46]. This is particularly relevant in view of the fact that polarization fields along the standard polar (0001) growth direction separate hole and electron wave functions, affecting the quantum efficiency of light-emitting devices detrimentally.

Therefore, the aim of this thesis is to investigate the electronic properties of $(10\bar{1}0)$ surfaces of (Al,Ga)N with different compositions ranging from the binaries GaN to AlN as well as for *n*- and *p*-type doping using cross-sectional scanning tunneling microscopy (XSTM) and spectroscopy (XSTS), aided by tunnel current simulations. Particular emphasis will be placed on the characterization of the intrinsic as well as extrinsic surface states and their effect on the Fermi-level pinning. This includes the investigation of the influence of air exposure on the surfaces’ electronic structure.

This thesis is structured as follows: Chapter 2 illustrates the tunnel effect, the fundamental effect behind the STM, as well as the influence of band structure and surface properties on the measured tunnel current. The setup of the STM and the sample structure is described in Chapter 3. Chapter 4 investigates the effect of all relevant semiconductor and tip’s materials properties on the tunneling spectra with help of self-consistent simulations of the tunnel current. In Chapter 5 the surface states of freshly cleaved as well as air-exposed non-polar *p*- and *n*-doped GaN surfaces are investigated. the interplay between intrinsic and extrinsic surface states and their effect on the surfaces’ electronic properties as a function of doping,

e.g., Fermi-level pinning, is derived from tunneling spectra. It is found that *n*-type surfaces are governed by the intrinsic and empty dangling bond state, whereas the Fermi-level pinning at *p*-type surfaces originates primarily from extrinsic defect states at step edges. Chapter 6 addresses the compositional dependence of the surface states and related properties of the ternary (Al,Ga)N solid solution (10 $\bar{1}$ 0) surfaces. A detailed description of the methodologies for the determination of the energy position of surface states is provided. A linear shift of the surface state with composition is found experimentally and compared with DFT calculations. Finally, in Chapter 7 the achieved results will be summarized.

Chapter 2

Theory

The scanning tunneling microscope (STM), first developed by Binnig *et al.* [47–51], is based on the quantum mechanic tunneling effect. The basic idea behind the STM is to approach a metal tip so close to a sample that a tunnel current can be measured. Then the tunnel current is probed as a function of the spatial position on the sample, creating a surface image.

An early description of the phenomenon later known as the tunnel effect was given by Hund in 1927 [52–54], who studied molecular spectra, their underlying molecular states, and the potential barrier between these different states. Hund treated the transition probability between left and right turning molecules as potential barrier dependent.

The theory describing one-dimensional tunneling through potential barriers was first found by Gamow in 1928 [55]. Using this theory, he was able to explain and describe radioactive alpha decay. In addition, Wentzel, Kramers, and Brillouin (WKB) [56–58] contributed to the general applicability of the tunneling effect by developing a numerical solution to the approximation of the one-dimensional time-independent Schrödinger equation for slowly varying potential barriers, also known as WKB approximation.

This Chapter is structured as follows: The simple case of tunneling through a constant potential barrier is explained in the first section (cf. Sec. 2.1). A general description of electron tunneling through non-constant potential barriers using the WKB approximation can be found in the second section (cf. Sec. 2.2). These

simplified models are sufficient to explain the exponential dependency of the tunnel current on barrier width. A more general model that incorporates a many-particle approach and which has been developed by Bardeen is illuminated in Sec. 2.3.2. Finally, the Tersoff-Hamann approximation, which models the tip states as s-states and enables more practical use of the Bardeen approach, is discussed in Sec. 2.3.3.

2.1 One-dimensional tunneling effect of a single particle

In classical mechanics, a particle with the energy E cannot pass through a barrier if its energy is lower than the barrier height V . Hence, quantum mechanics is mandatory to describe the tunnel effect. By solving the Schrödinger equation, a non-zero probability density of a particle behind the potential barrier is obtained. For a single particle, the one-dimensional Schrödinger equation is represented by:

$$i\hbar \frac{\partial}{\partial t} \psi(x, t) = \left[-\frac{\hbar^2}{2m} \frac{\partial^2}{\partial x^2} + V(x, t) \right] \psi(x, t). \quad (2.1)$$

Since the particle's probability of tunneling through a potential barrier is a stationary problem, it is sufficient enough to describe the tunneling from tip to sample or vice versa through the vacuum using the time-independent Schrödinger equation

$$E\psi(x) = \left[-\frac{\hbar^2}{2m} \frac{\partial^2}{\partial x^2} + V(x) \right] \psi(x). \quad (2.2)$$

The tunneling barrier can be described in first approximation by a rectangular potential barrier with a value of V_0 in the region between 0 and d and zero elsewhere (cf. Fig. 2.1a)

$$V(x) = \begin{cases} 0 & \text{if } x < 0 \\ V_0 & \text{if } 0 < x < d \\ 0 & \text{if } x > d \end{cases}. \quad (2.3)$$

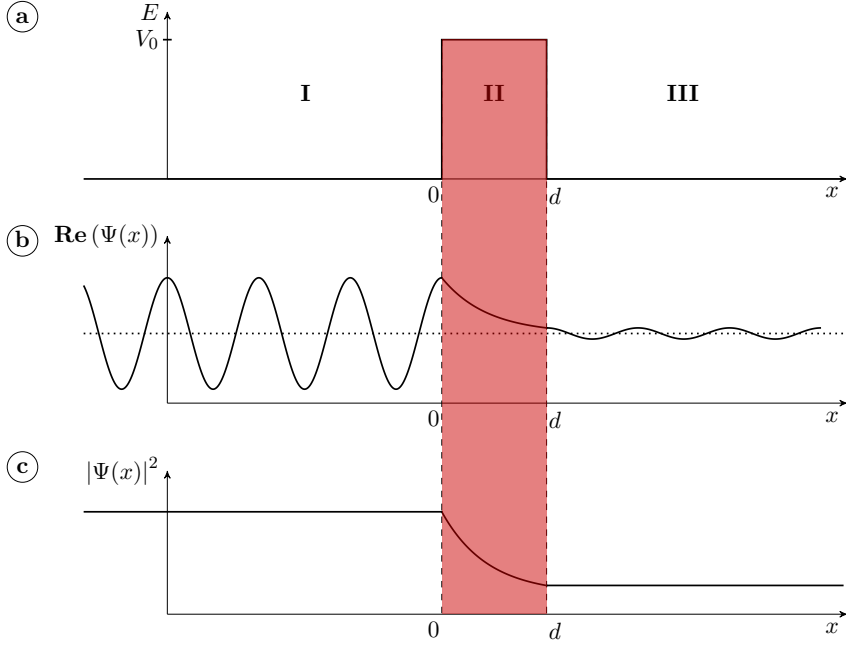


Figure 2.1: One-dimensional tunneling effect for an electron coming from $x = -\infty$. (a) Rectangular potential barrier with the height V_0 between 0 and d . (b) Schematic of the real part of the wave function that solves the Schrödinger equation for a potential barrier shown in (a). (c) Probability density of the wave function. Although the probability density exponentially decreases inside the potential barrier, a significant remnant can be found behind the barrier in region **III** for relatively small vacuum gaps. Adapted from Ref. [59].

In Fig. 2.1a the regions before, in, and after the potential barrier are labeled **I**, **II**, and **III**, respectively. For the STM, region **I** can be interpreted as the tip, **II** as the vacuum, and **III** as the sample. For the regions where the energy E is larger than the potential $V(x)$, the general plane wave ansatz for a free particle (or electron) can be assumed (cf. Fig. 2.1)

$$\psi(x) = A \cdot e^{ikx} + B \cdot e^{-ikx} . \quad (2.4)$$

2.1 One-dimensional tunneling effect of a single particle

A is the amplitude of the wave traveling in x direction, while B is the amplitude of the wave that moves in $-x$ direction. k is the wave vector given by

$$k = \frac{\sqrt{2m_e(E - V(x))}}{\hbar}. \quad (2.5)$$

The potential $V(x)$ is zero in region **I**, and the potential barrier partly reflects the incoming free particle wave. The amplitude of the incoming wave can be normalized to 1, while the amplitude of the reflected wave is labeled R

$$\psi_{\mathbf{I}}(x) = 1 \cdot e^{ikx} + R \cdot e^{-ikx}. \quad (2.6)$$

When the electron passes the potential barrier and reached region **III**, no further reflection occurs. Thus, the wave function is composed of the transmitted part with amplitude T

$$\psi_{\mathbf{III}}(x) = T \cdot e^{ikx}. \quad (2.7)$$

For region **II** the energy of the particle is smaller than the potential barrier $V_0 > E$. This leads on the basis of Eq. 2.3, and 2.4 to an exponential decay of the wave function

$$\psi_{\mathbf{II}}(x) = \psi(0)e^{-\kappa x}, \quad (2.8)$$

with κ being

$$\kappa = \frac{\sqrt{2m(V_0 - E)}}{\hbar}. \quad (2.9)$$

Continuity conditions must be fulfilled at the boundaries between **I** and **II**, and additionally **II** and **III**. These conditions are $\psi_{\mathbf{I}}(0) = \psi_{\mathbf{II}}(0)$ and $\psi'_{\mathbf{I}}(0) = \psi'_{\mathbf{II}}(0)$ as well as $\psi_{\mathbf{II}}(d) = \psi_{\mathbf{III}}(d)$ and $\psi'_{\mathbf{II}}(d) = \psi'_{\mathbf{III}}(d)$. They can be employed to determine the amplitudes R , T as well as $\psi(0)$. A detailed derivation of these quantities can be found in refs. [60–62]. Here the transmission amplitude

$$T = e^{-ikd} \frac{2k\kappa}{2k\kappa \cosh(\kappa d) - i(k^2 - \kappa^2) \sinh(\kappa d)}, \quad (2.10)$$

is of particular interest because the square of its absolute value corresponds to the transmission probability

$$|T|^2 = \frac{1}{1 + \frac{V_0^2}{4E(V_0 - E)} \sinh^2(\kappa d)}. \quad (2.11)$$

$|T|^2$ can be interpreted as the particle flux through the potential barrier [63]. For a barrier width d and the assumption $\kappa d \gg 1$, the transmission probability (Eq. 2.11) can be simplified using the approximation [63]

$$\sinh^2 \kappa d \approx \frac{1}{4} e^{2\kappa d} \gg 1, \quad (2.12)$$

to

$$|T|^2 \approx \frac{16E(V_0 - E)}{V_0^2} e^{-2d\kappa}. \quad (2.13)$$

The transmission probability thus depends exponentially on the potential barrier width d . The prefactor depends only on the energy of the particle E and the potential height V_0 . Additionally, these are also included in the exponent via the decay constant κ .

In conclusion, an electron with an energy lower than a finite potential barrier $E < V_0$ has a non-zero transmission probability for finite barrier widths. This is in strong contrast to classical mechanics, where no transmission probability is found. For all practical applications, one has to consider that the wave function in region **II** decays exponentially. This exponential decay limits the barrier widths for which a significant tunneling current can be obtained to the nanometer regime.

2.2 Tunneling between materials with a different work function

Thus far, only equal work functions in the region **I** and **III** were assumed. This assumption is viable between similar materials, e.g., for metals. For materials with

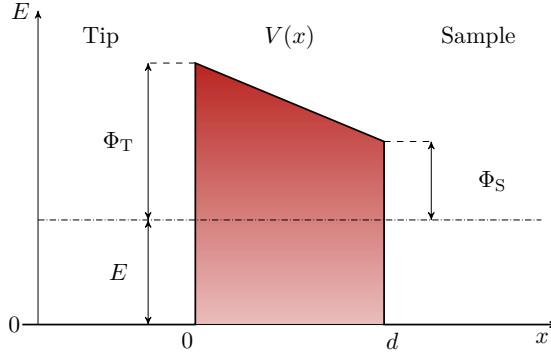


Figure 2.2: Trapezoidal barrier caused by different work functions of sample Φ_S and tip Φ_T . Adapted from Ref. [63].

different work functions trapezoid barriers need to be considered. However, analytical solutions of the Schrödinger equation are only known for a few specific potential barriers. For an accurate description of tunneling between various materials and under manifold conditions, a generalized solution of the one-dimensional Schrödinger equation for arbitrary potential barrier shapes is required [63]. The so-called WKB approximation achieves this.

In Sec. 2.1 an exponential decay in the region of the constant potential barrier V was derived. If the potential barrier height $V(x)$ varies over x , the ansatz must be rewritten as

$$\psi(x) = Ae^{ik(x)x}, \quad (2.14)$$

with a wave vector $k(x) = \frac{\sqrt{2m(E-V(x))}}{\hbar}$ that is no longer independent of x (cf. Eq. 2.5). If the one-dimensional potential barrier $V(x)$ varies only slowly with x (cf. Fig. 2.2), one can approximate it by small segments with constant potential [63]. Such infinitesimal rectangular barriers exhibit heights $V(x)$ and thicknesses dx . Following this idea, the approximated wave function can be calculated by integration over

the infinitesimal wave vector changes

$$\psi(x_1) = \psi(x_0) \exp \left[\pm i \int_0^d k(x) dx \right]. \quad (2.15)$$

Considering only the leading exponential term in Eq. 2.13, the transmission probability can be found to

$$|T|^2 \propto \exp \left[-\frac{2\sqrt{2m_e}}{\hbar} \int_0^d \sqrt{V(x) - E} dx \right]. \quad (2.16)$$

Applying this approximation to the trapezoidal barrier (cf. Fig. 2.2) $V(x) = E + \Phi_T - \frac{x}{d}(\Phi_T - \Phi_S)$ [63], the integral within the exponential function on the right hand side of Eq. 2.16 yields

$$\int_0^d \sqrt{\Phi_T - \frac{x}{d}(\Phi_T - \Phi_S)} dx = \frac{2d}{3} \cdot \frac{\Phi_T^{\frac{3}{2}} - \Phi_S^{\frac{3}{2}}}{\Phi_T - \Phi_S}. \quad (2.17)$$

Hence the solution for the transmission probability considering a trapezoid potential barrier is then given as

$$|T|^2 \propto \exp \left[-\frac{4d\sqrt{2m_e}}{3\hbar} \cdot \frac{\Phi_T^{\frac{3}{2}} - \Phi_S^{\frac{3}{2}}}{\Phi_T - \Phi_S} \right]. \quad (2.18)$$

The transmission probability, therefore, depends on the difference in the work functions, the work functions in the numerator even have a $\frac{3}{2}$ exponent.

2.3 Towards many-particle tunneling

The Bardeen approach takes into account the fact that a current usually consists of more than one electron. While the equations obtained for the transmission probabilities of single-particle tunneling through a one-dimensional rectangular (cf. Sec. 2.1) or trapezoidal (cf. Sec. 2.2) potential barrier are adequate in their limits, the derivation of actual tunnel currents requires the incorporation of

multiple particles with slightly deviating energies. Finally, the Tersoff-Hamann approximation of the Bardeen approach will be introduced in Sec. 2.3.3. In this approximation, certain assumptions of the front-most tip states are employed to obtain a tunnel current equation that depends only on the sample properties.

2.3.1 Density of states

For the description of many-particle tunneling, it is necessary to define a density of electron states. The density of states $\rho(E)$ is defined as a distribution function that specifies the sum of all electronic states dN in an energy range between E and $E + dE$ [63–65]:

$$dN(E, E + dE) = \rho(E)dE. \quad (2.19)$$

To obtain the sum over all states N in a finite energy element between E_1 and E_2 the expression has to be integrated

$$N(E_1, E_2) = \int_{E_1}^{E_2} \rho(E) dE. \quad (2.20)$$

Under the assumption that all n states (n being the running index) are discrete, the density of states is given by a sum over n delta functions at the states' corresponding energy levels E_n [63]. If all energy states E_n are in the range between E_1 and E_2 , Eq. 2.20 can be rewritten as

$$N(E_1, E_2) = \int_{E_1}^{E_2} \sum_n \delta(E - E_n) dE = \sum_n 1. \quad (2.21)$$

This equation refers to either the whole system or a unit volume of a periodic system [63]. In addition, the local density of states (LDOS) takes the probability density $|\psi(r)|^2$ of every state at a spatial position r into account and is defined as

$$\text{LDOS} = \sum_n |\psi_n(r)|^2 \delta(E - E_n). \quad (2.22)$$

In thermal equilibrium, the occupation probabilities of filled states are given by the Fermi-Dirac equation

$$f(E) = \frac{1}{\exp\left[\frac{E-E_F}{k_B T}\right] + 1}, \quad (2.23)$$

where k_B is the Boltzmann constant and T is the temperature. Hence the number of filled electron states N is determined by the integral over the (local) density of states, multiplied by the occupation probability $f(E)$, as indicated by the equation

$$N = \int_0^{\infty} \rho(E) f(E) dE. \quad (2.24)$$

2.3.2 Bardeen approach of tunneling theory

The Bardeen tunneling model from 1961 was the first practical approach for tunneling between solids [66]. At that time, the considered tunneling system was a metal-insulator-metal junction. A similar approach was also made by Simmons for a more general potential barrier but in the limit of small voltages [67]. The theory is also applicable for the later developed STM and can properly describe the process of tunneling between a sample and a tip through a vacuum barrier.

This approach assumes separate free subsystems for sample and tip with associated wave functions ψ_S and ψ_T , respectively. The two subsystems and the corresponding wave functions are illustrated in Fig. 2.3b for the sample and in Fig. 2.3c for the tip. These wave functions extend in their subsystems into infinitely wide potential barriers [63,66,68]. Figure 2.3a schematically depicts the sample and tip's density of states and occupations under an applied voltage V . Bardeen used a time-dependent perturbation theory to calculate the transfer rate of an electron from one electrode to another [66, 68]. As a result, the tunneling matrix element M is given by the overlap of the wave functions of the two subsystems at an arbitrary surface which lies entirely within the potential barrier [66,68]. Hence the tunneling matrix element

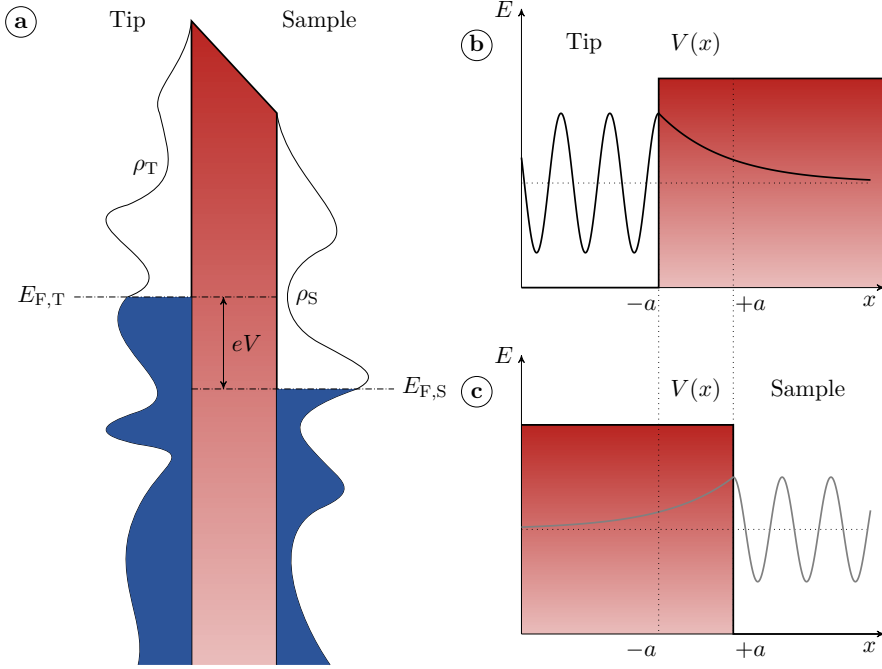


Figure 2.3: (a) Both tip and sample states are filled up to the Fermi level E_F . The applied voltage V leads to an energy difference eV between the occupied sample and tip states. The Bardeen approach starts with two independent subsystems for sample (b) and tip (c). The tunneling current is given by Fermi's golden rule and the overlap of both wave functions. Adapted from Ref. [68].

can be expressed as a surface integral over that surface.

$$M_{TS} = \frac{\hbar^2}{2\pi} \int \psi_T \nabla \psi_S^* - \psi_S^* \nabla \psi_T dS. \quad (2.25)$$

The electron transition probability $\Gamma_{T \rightarrow S}$ between the two wave functions is given by Fermi's golden rule

$$\Gamma_{T \rightarrow S} = \frac{2\pi}{\hbar} |M_{TS}|^2 \delta(E_S - E_T), \quad (2.26)$$

where E_T and E_S are the energies of the tip and sample state, respectively. For ob-

taining the tunnel current, one has to sum over all states and multiply by $2e$ because of the spin degeneracy [63, 68]. Taking into account the Fermi-Dirac distributions as well as the density of states of both tip and sample, this leads to

$$I = \frac{4\pi e}{\hbar} \int_{-\infty}^{+\infty} [f(E_F - eV + \varepsilon) - f(E_F + \varepsilon)] \rho_T(E_F - eV + \varepsilon) \rho_S(E_F + \varepsilon) |M|^2 d\varepsilon. \quad (2.27)$$

In the following, the Fermi energy of the sample is defined as reference energy, i.e., $E_{F,S} = 0$. In the limit of low temperatures, the Fermi-Dirac distribution can be replaced by a step-function which translates into new integration limits and thus simplifies Eq. 2.27 further [63, 68, 69]:

$$I = \frac{4\pi e}{\hbar} \int_0^{eV} \rho_T(\varepsilon - eV) \rho_S(\varepsilon) |M|^2 d\varepsilon. \quad (2.28)$$

In order to obtain the matrix element in the one-dimensional case, the ansatz of the exponential decay (cf. Eq. 2.8) can be used inside the potential barrier for both tip's and sample's wave function. Different starting positions $-a$ and a for the exponential decay of the tip's (cf. Fig. 2.3b) and sample's (cf. Fig. 2.3c) wave function, respectively, need to be considered. Assuming only elastic tunneling, the tunneling matrix element becomes $M_{TS} = M(\varepsilon)$. In addition, the tunneling matrix is reduced to only one dimension. Hence the transmission probability equals the tunneling matrix element $|T(\Phi, d)|^2 = |M(\varepsilon)|^2$. Evaluating the integral inside of the potential barrier results in the same exponential dependency for the transmission probability

$$|T(\Phi, d)|^2 = \propto \exp \left[-2d \sqrt{\frac{2m}{\hbar^2} \Phi} \right]. \quad (2.29)$$

Hence, in the one-dimensional limit, the results of Bardeen's approach merge into that of the simple one-dimensional approach (cf. Eq. 2.11) as discussed in Sec. 2.1.

To include the WKB approximation (cf. Sec. 2.2) in the one-dimensional Bardeen-approach the trapezoidal potential barrier is approximated by the effective potential

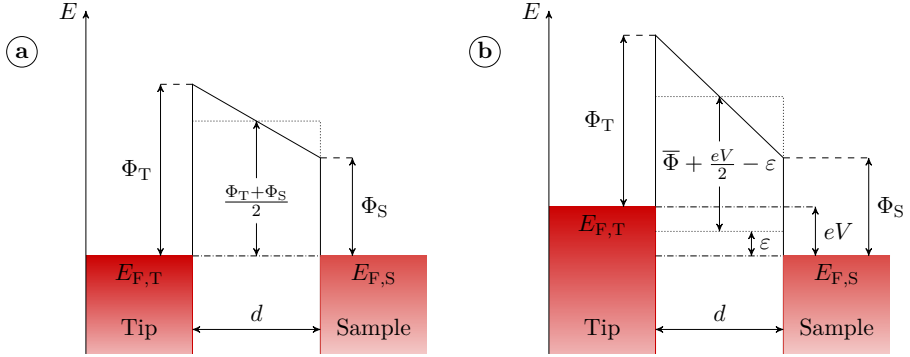


Figure 2.4: (a) Potential barrier for a tip-sample system with different tip and sample workfunctions Φ_T and Φ_S , respectively. (b) Same system with an additional applied voltage V . Adapted from Ref. [63].

barrier height $\bar{\Phi} = (\Phi_T + \Phi_S)/2$. Note that this approximation is not well justified because it neglects the exponential dependency of the transmission probability. Nevertheless, it is generally used, even though it underestimates the current [63].

The above-discussed case is illustrated in Fig. 2.4a for thermal equilibrium and without bias. Applying an additional voltage between tip and sample alters the effective barrier height by $eV/2$ (cf. Fig. 2.4b). For a sample state at an energy ϵ (relative to the sample's Fermi level), the effective potential barrier height changes to $\Phi_{\text{eff}}(\epsilon, V) = \bar{\Phi} + \frac{eV}{2} - \epsilon$. Substituting this effective potential barrier height into the transmission probability for the constant potential barrier (cf. Eq. 2.29) leads to a transmission probability for the trapezoid potential barrier, which is given by

$$|T(\epsilon, V, d)|^2 \propto \exp \left[-2d \sqrt{\frac{2m}{\hbar^2}} \sqrt{\frac{\Phi_S + \Phi_T}{2} + \frac{|eV|}{2} - \epsilon} \right]. \quad (2.30)$$

2.3.3 Tersoff and Hamann approximation

In 1983, one year after Binnig *et al.* developed the first STM in 1982 [47], Tersoff and Hamann adapted the theoretical understanding by introducing a localized tip of the STM [70]. Thus far, theory considered only tunneling between two-dimensional

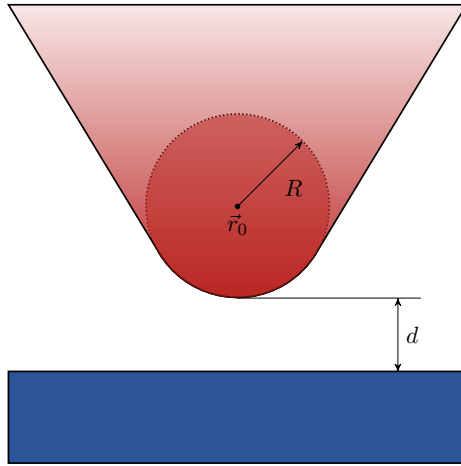


Figure 2.5: Tersoff-Hamann approximation of the STM tip. The tip states are modeled as s-wave functions with radius R and centered at \vec{r}_0 . Adapted from Refs. [68,70].

plates [66, 67, 69]. The spherical shape of the tip, as shown in Fig. 2.5, confines the tunneling process spatially due to the exponential decaying tunnel probability. This allows the incorporation of further useful approximations. Bardeen's approach of the tunnel current requires the knowledge of the density of states of both sample and tip. Since the tip's density of states usually remains unknown, no information of the sample's density of states can be revealed using this approach. In contrast, by modeling the tip states as s-wave functions, the approximation by Tersoff and Hamann allows getting information about the sample's density of states.

The tunnel current equation derived by Tersoff and Hamann is based on first order perturbation theory [71], applied to the results of Bardeen [66], i.e., Eq. 2.27

$$I = \frac{2\pi e}{\hbar} \sum_{T,S} f(E_T) [1 - f(E_S + eV)] |M_{TS}|^2 \delta(E_T - E_S). \quad (2.31)$$

In the limit of low temperatures and small voltages, this equation simplifies to:

$$I = \frac{2\pi e^2 V}{\hbar} \sum_{T,S} |M_{TS}|^2 \delta(E_S - E_F) \delta(E_T - E_F). \quad (2.32)$$

At this stage, Tersoff and Hamann noted [71] that treating the tip as a point only

would be an oversimplification since it leads to an arbitrarily localized tip wave function. This, in turn, would result in a matrix element that is only proportional to the amplitude of the sample wave function ψ_S and the tip position \vec{r}_0 . Therefore, the current would be proportional to

$$I \propto \sum_S |\psi_S(\vec{r}_0)|^2 \delta(E_S - E_F), \quad (2.33)$$

The right-hand side of the equation can directly be identified as the sample's LDOS (cf. Eq. 2.22). However, due to the finite dimension of the tip, this assumption can obviously not be upheld. Therefore, Tersoff and Hamann introduced other approximations for the sample and tip wave functions ψ_S and ψ_T . They expanded the sample wave function to

$$\psi_S = \frac{1}{\sqrt{\Omega_S}} \cdot \sum_G a_G \cdot \exp \left[\sqrt{\kappa^2 + |\vec{\kappa}_G|^2} \cdot z \right] \cdot \exp [i\vec{\kappa}_G \cdot \vec{x}], \quad (2.34)$$

which is a general expression for a wave function in a region with negligible potential [71]. Ω_S is the sample volume, κ the usual decay constant $\kappa = \sqrt{2m\Phi}/\hbar$, and a_G the normalization coefficients. $\vec{\kappa}_G = \vec{k}_{\parallel} + \vec{G}$ is defined as the sum of the surface parallel wave vector of the state \vec{k}_{\parallel} and the surface reciprocal-lattice vector \vec{G} .

The tip wave function is modeled as a spherical potential well (cf. Fig. 2.5) where R is the radius of the tip, \vec{r}_0 the center, and d is the smallest distance between the sample surface and the spherical tip [71]. With this asymptotic spherical form, the wave function of the tip results in

$$\psi_T = \frac{1}{\sqrt{\Omega_T}} \cdot c_T \kappa R \exp [\kappa R] \cdot \frac{\exp [-\kappa |\vec{r} - \vec{r}_0|]}{\kappa |\vec{r} - \vec{r}_0|} \quad (2.35)$$

with Ω_T being the tip volume and c_T the normalization coefficient. For simplicity reasons, the work function Φ is assumed to be identical for tip and sample. Thus at low voltages, the tip states can be approximated as s-orbital wave functions with spherical symmetry [70, 71]. Substituting the above-defined wave function into the tunneling matrix element (cf. Eq. 2.25) yields:

$$M_{TS} = \frac{\hbar^2}{2m} \frac{4\pi}{\kappa \sqrt{\Omega_T}} \cdot \kappa R \exp [\kappa R] \cdot \psi_S(\vec{r}_0). \quad (2.36)$$

Eventually, the tunnel current in the Tersoff-Hamann approximation is obtained:

$$I = \frac{32\pi^3 \cdot e^2 V}{\hbar} \Phi^2 D_T(E_F) \cdot \frac{R^2}{\kappa^4} \exp[2\kappa R] \cdot \sum_S |\psi_S(\vec{r}_0)|^2 \delta(E_S - E_F). \quad (2.37)$$

The last part of the equation's right-hand side equals the LDOS (cf. Eq. 2.22). From this, it follows that the current is directly proportional to the sample density of states

$$I \propto \rho_S(E_F, \vec{r}_0), \quad (2.38)$$

taking into account the exponentially decaying tip.

This approximation is the main theory explaining why the STM predominantly measures the sample's local density of states, even though it can not really explain the spatial resolution. Further in-detail analysis of tip-sample interactions was done by Chen *et al.* [72], including more than just s-wave functions. Stronger localized orbitals can then explain the high spatial resolution.

2.4 Tunneling in semiconductors

Up to now, tunneling was described for metals and metal-like materials. These are characterized by a high charge carrier concentration. In contrast, semiconductors have a low to zero density of states close to the Fermi level. Therefore, the electrostatic screening is weaker, and the electrostatic potential can penetrate into the material, leading to a band bending. A variety of effects can have an impact on band bending in semiconductors. If metals are in direct contact with semiconductors, a contact potential arises from the difference in their work functions. In the simplest case, the Schottky-Mott rule is sufficient to describe the contact potential and hence the band bending [73, 74]. However, the existence of interface states can considerably complicate the potential at the interface, as these can lead to Fermi-level pinning [75].

Similarly, a band bending can be observed at semiconductor surfaces, where surface states can pin the Fermi level. In addition to surface states, the presence of a metal

probe tip near the semiconductor surface modifies its band bending, too. This effect is commonly referred to as tip-induced band bending.

The following two sections introduce tip-induced band bending (cf. Sec. 2.4.1) and the impact of surface Fermi-level pinning induced by extrinsic and intrinsic surface states (cf. Sec. 2.4.2).

2.4.1 Tip-induced band bending

If a metal tip is brought in contact with a semiconductor, a contact potential arises, which is defined by the difference of the metal's (Φ_T) and semiconductor's work function ($\chi - (E_C - E_F)$)

$$\Delta\Phi = \Phi_T - \chi - (E_C - E_F), \quad (2.39)$$

where χ is the electron affinity, and E_C is the conduction band minimum of the semiconductor [76]. This contact potential is screened by few charge carriers only and can therefore penetrate the surface into its sub-surface region. The penetration length (or screening length) depends on the concentration of fixed and free carriers present in the sub-surface region [22, 76]. In first approximation, the applied voltage shifts the Fermi energy of the tip by eV relative to the Fermi level of the semiconductor (cf. Fig. 2.6). Hence, the electrostatic potential of the probe tip relative to the semiconductor for the biased system is given by:

$$\phi_{\text{Tip}} = V + (\Delta\Phi)/e. \quad (2.40)$$

The electrostatic potential profile in the vacuum region between tip and semiconductor as well as in the sub-surface region of the semiconductor (i.e., the band bending) can be derived by solving the Poisson equation under consideration of standard semiconductor equations for the description of the charge carrier distribution $n(x, y, z)$ and $p(x, y, z)$ for electrons and holes, respectively, and the ionized donor N_D^+ and acceptor N_A^- concentrations. In three dimensions, this yields the

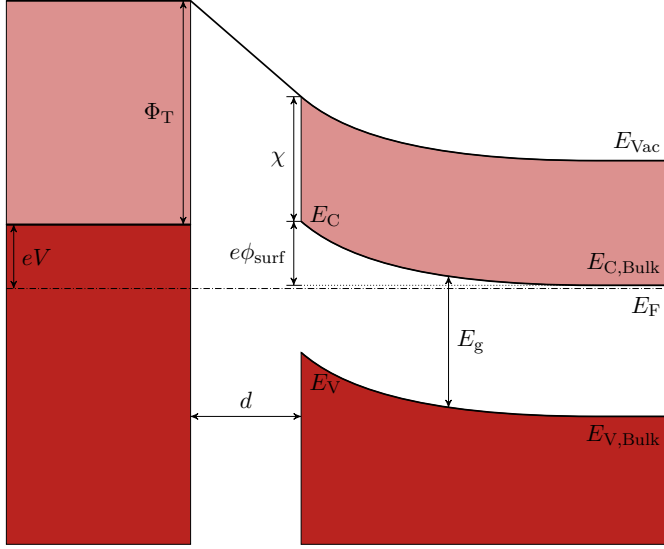


Figure 2.6: Tip-induced band bending with applied voltage eV in the tip-sample system.

following equation:

$$\Delta\phi(x, y, z) + \frac{e}{\varepsilon_0\varepsilon_r} \left(p(x, y, z) - n(x, y, z) + N_D^+ - N_A^- \right) = 0, \quad (2.41)$$

where ε_r is the relative permittivity of the semiconductor and ε_0 is that of the vacuum. The ionized donor and acceptor concentration is defined employing the Fermi-Dirac distribution [77, 78]

$$N_D^+ = \frac{N_D}{1 + 2 \exp\left(\frac{E_F - E_D}{k_B T}\right)}, \quad \text{and} \quad (2.42)$$

$$N_A^- = \frac{N_A}{1 + 2 \exp\left(\frac{E_A - E_F}{k_B T}\right)}, \quad (2.43)$$

where E_D and E_A are the ionization energy levels of the respective donor and acceptor states.

At the vacuum-semiconductor interface, the permittivity usually changes by a factor of ≈ 10 . This leads to continuity/boundary conditions similar to those of light refraction at the air-water interface. This effect needs to be taken into account

by employing the interface condition that the dielectric displacement density $\vec{D} = -\varepsilon_0\varepsilon_r\nabla\phi$ in normal direction \vec{n} to the interface remains constant

$$\vec{n} \cdot (\vec{D}_{\text{vac}} - \vec{D}_{\text{semi}}) = 0. \quad (2.44)$$

If a surface charge density is present at this interface, the interface condition becomes

$$\vec{n} \cdot (\vec{D}_{\text{vac}} - \vec{D}_{\text{semi}}) = \sigma, \quad (2.45)$$

where σ is the surface charge density.

Due to the complexity of the above described tip-vacuum-semiconductor system in three spatial dimensions and the interface condition that commonly includes surface charges, this electrostatic problem can be solved numerically only, using standard Poisson solvers, either based on the finite element or finite difference method [76, 79].

Further insight on the simulation of tunnel currents and spectra is given in Sec. 4 for III-N semiconductors like GaN, which are mainly addressed in this work. In particular, the influence of typical parameters such as tip-sample separation, dopant concentration, surface states (cf. Sec. 2.4.2), electron affinity, and tip-dependent parameters such as tip radius and work function.

2.4.2 Band bending due to surface states

The electrical and structural properties of surfaces and interfaces are fundamentally different from those of bulk materials. This stems from the fact that the theoretical description via Bloch waves reaches its limit for surfaces and interfaces since the infinite periodic expansion is no longer given [80, 81].

Surface states at an ideal semiconductor surface may arise from unsatisfied valence electrons of the surface atoms (i.e., dangling bond states). These states are commonly called intrinsic surface states since they are inherently connected to the sudden interruption of the material at the surface. On the other hand, extrinsic

surface states can arise from many different origins. For example, adsorbate surface states originate from the bonds between adsorbates and the semiconductor surface [82]. Furthermore, extrinsic surface states can be caused by defects.

Fundamentally, the charge of the surface states must be compensated by a space charge region such that the system is uncharged at thermal equilibrium [75, 77, 83–87]. This charge neutrality condition can be written as

$$Q_{\text{ss}} + Q_{\text{sc}} = 0. \quad (2.46)$$

where Q_{ss} and Q_{sc} are the charge of the surface state and the space charge region, respectively.

The type of surface states differs depending on their physical origin. On the one hand, acceptor-like surface states exist, which are considered to be electrically neutral if they are below the semiconductor's Fermi level (cf. Fig. 2.7b). However, if these states are above the Fermi level, they become negatively charged (cf. Fig. 2.7a).

On the other hand, donor-like surface states exhibit a contrary behavior: If they are situated above the Fermi level, they are positively charged (cf. Fig. 2.7d), while they remain uncharged and thus electrically neutral below the Fermi level (cf. Fig. 2.7c). Figure 2.7 illustrates the band bending of both p - and n -type semiconductors in the presence of midgap acceptor-like and donor-like surface states in thermal equilibrium. Extrinsic and defect states are commonly considered to be composed of multiple states, which have either acceptor- or donor-like character. The electronic interplay of these different states then commonly results in Fermi-level pinning.

Electrical passivation of surface states can be achieved by adsorbates. For example, a surface treatment with hydrogen leads in many cases to the creation of adsorbate surface states outside of the fundamental band gap [88–90].

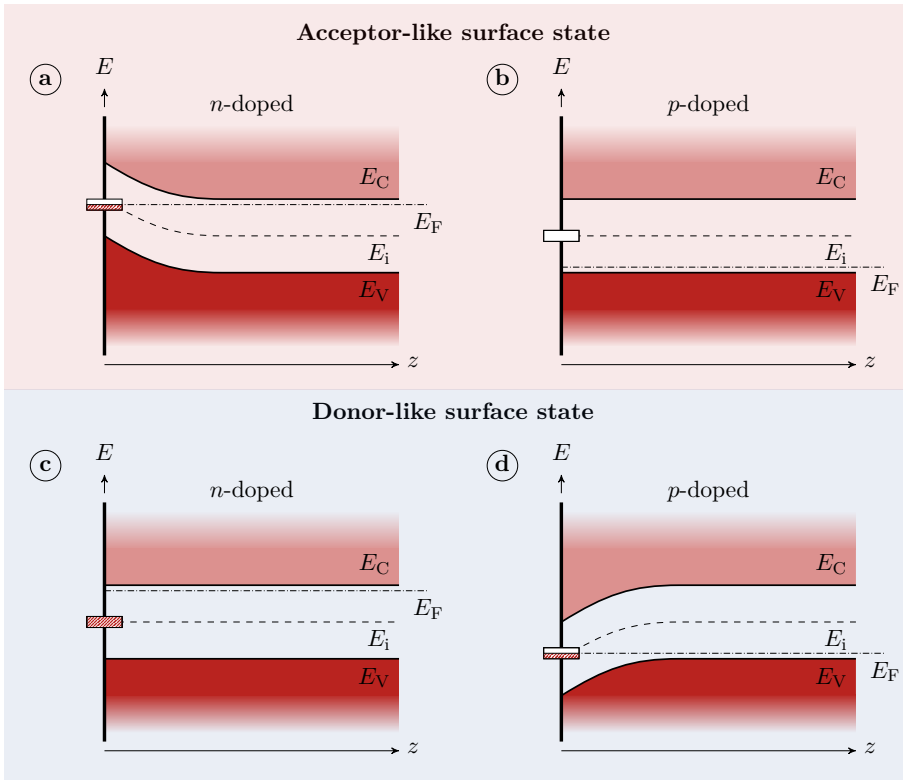


Figure 2.7: Comparison between acceptor- and donor-like surface states, each for n - and p -doping. In order to explain the principle, midgap surface states are assumed in each case. (a)-(d) Band bending in charge equilibrium between surface states and any space charge region in the semiconductor. (a) the acceptor energy level is below the Fermi level of the n -doped semiconductor and is therefore negatively charged. In charge equilibrium, the upward band bending due to the positive charge of the space charge region compensates for the negatively charged surface states. (d) In the opposite case for donor-like surface states, the states are positively charged in p -doped semiconductors. A downward band bending compensates the positive charge of the surface state with the negatively charged space charge region. For both (b) p -doped semiconductor and acceptor-like surface states and (c) n -doped semiconductor and donor-like surface states, the surface states are uncharged, and flat-band conditions prevail. In these cases, a band bending would provide a charge with the same sign of the surface states, therefore actively preventing a band bending. Adapted from Ref. [82]

2.5 Band structure and surface state position of III-nitride ($10\bar{1}0$) according to DFT calculations

Previous reports based on density functional theory (DFT) calculations revealed the position of surface states on non-polar binary III-nitride semiconductor surfaces and their electronic band structure [33–35, 37, 41, 91]. Figure 2.8 shows the band structure of GaN, InN, and AlN ($10\bar{1}0$) surfaces. The data were taken from Van de Walle and Segev (GaN, InN) [33], and from Miao *et al.* (AlN) [41]. The band structures of GaN and InN were calculated by DFT with the local density approximation (LDA), where the modified pseudopotential approach was used to reproduce the experimental band gaps (cf. Fig. 2.8a and b) [33]. The band structure of AlN was calculated using DFT with the generalized gradient approximation (GGA), augmented wave potentials, and the hybrid functional approach implemented in the Heyd-Scuseria-Ernzerhof (HSE) framework with a mixing parameter of 32% to obtain a band gap of 6.1 eV (cf. Fig. 2.8c) [41].

For m -plane GaN and AlN ($10\bar{1}0$) surfaces, the Ga/Al-derived empty intrinsic surface state lies below the conduction band throughout the first Brillouin zone [33, 41]. The minimum position of the Ga-derived empty dangling bond at the m -plane GaN surface is about 0.7 eV below the conduction band minimum at the $\bar{\Gamma}$ -point of the surface Brillouin zone (cf. Fig. 2.8a) [33, 34]. The maximum of the Ga-derived dangling bond state at the \bar{X} point exhibits nearly the same energy as the conduction band minimum at the $\bar{\Gamma}$ point. Hence, the dispersion of the Ga-derived surface state is roughly 0.7 eV. This empty surface state can be occupied by electrons and thus pins the Fermi level of an n -doped GaN surface ≈ 0.7 eV below the conduction band. The occupied N-derived dangling bond overlaps (i.e., is resonant) with the valence band at the $\bar{\Gamma}$ -point and has no significant DOS within the fundamental band gap. Only the Ga-derived surface state may thus pin the Fermi level at the surface.

Both intrinsic surface states of m -plane AlN surfaces are situated within the fundamental band gap. At the $\bar{\Gamma}$ -point, the minimum of the empty Al-derived dangling

2.5 Band structure and surface state position of III-nitride ($10\bar{1}0$) according to DFT calculations

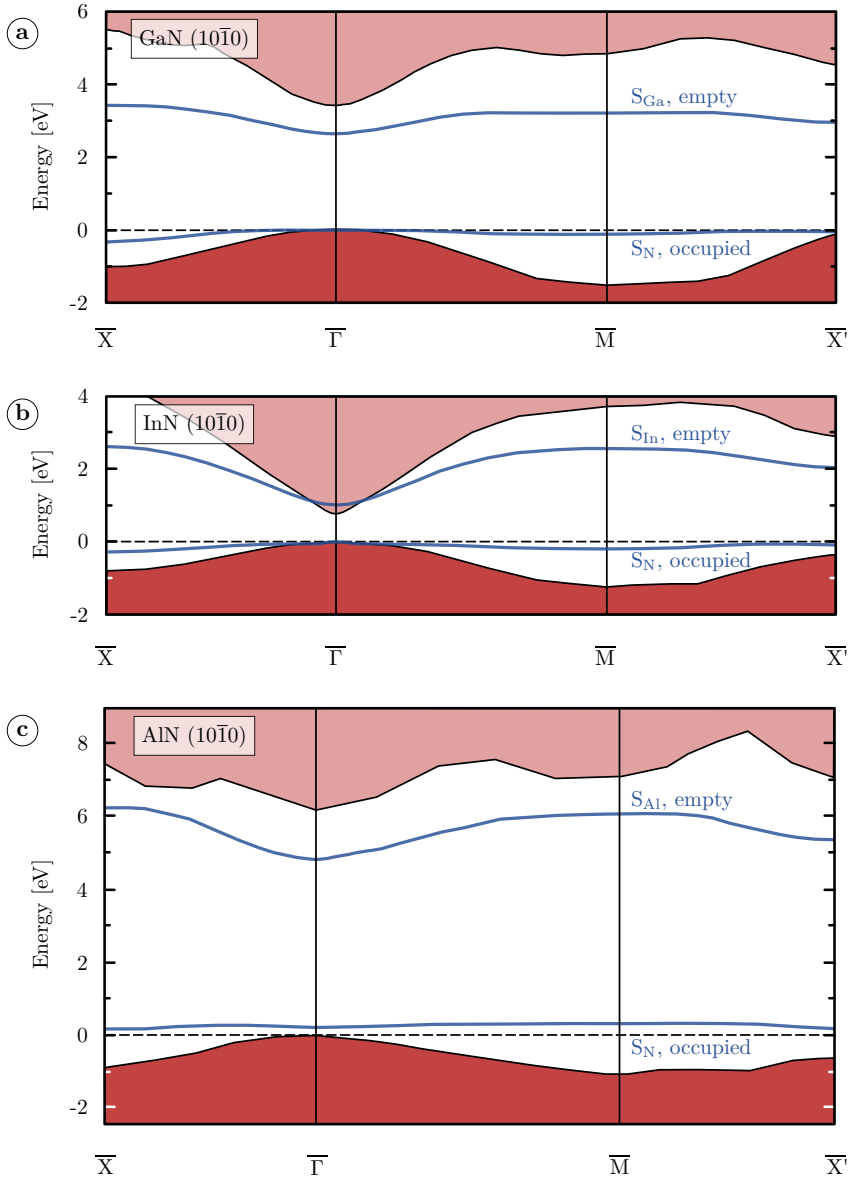


Figure 2.8: Calculated electronic band structure of the non-polar m -plane ($10\bar{1}0$) surfaces of (a) GaN ($10\bar{1}0$) (the data is taken from Ref. [33]), (b) InN (the data is taken from Ref. [33]) and (c) AlN (the data is taken from Ref. [41]).

bond state is about 1.3 eV below the conduction band edge [33], while the maximum at the \bar{X} -point is located at the same energy as the conduction band edge (cf. Fig. 2.8c). The dispersion of the Al-derived dangling bond state is hence about 1.3 eV. The filled N-derived dangling bond state is 0.2 eV above the valence band edge at the $\bar{\Gamma}$ -point. Both dangling bond surface states at AlN (10 $\bar{1}$ 0) surfaces can pin the Fermi level. For *n*-type AlN, only the empty Al-derived dangling bond state can inflict Fermi-level pinning (cf. previous Sec. 2.4.2) and, in principle, for *p*-doped AlN, the filled N-derived dangling bond state.

The maximum of the LDOS of the III-derived surface state is energetically at the edge of the conduction band for both AlN and GaN. However, the lowermost tail of the surface state's DOS, which is located energetically deeper in the fundamental band gap, yields sufficient surface charges for a full Fermi-level pinning.

For the *m*-plane InN (10 $\bar{1}$ 0) surfaces, both the empty In-derived dangling bond state and the filled N-derived dangling bond state overlap with the conduction and valence band (cf. Fig. 2.8b), respectively. Thus, no pinning by intrinsic surface states is expected at the InN(10 $\bar{1}$ 0) surface.

Chapter 3

Experimental setup

In this chapter, the basic preparation steps necessary for STM investigations are explained. In addition, the technical aspects of standard and cross-section STM, as well as their modes of operation, are introduced. The first section illustrates a method for preparing probe tips, which are suitable to obtain atomic resolution depending on the sample material (cf. Sec. 3.1). The sample preparation process is elucidated in Sec. 3.2. Technical aspects and the operation modes of STM are described in Sec. 3.3. In the last section of this chapter, detailed descriptions of the semiconductor samples analyzed in this thesis are given (cf. Sec. 3.4.1 and 3.4.2).

3.1 Tip preparation

The tips used in this work were etched from tungsten wire with a diameter of 0.25 mm using a 10 % sodium hydroxide solution NaOH. The NaOH solution is a thin film suspended within a platinum wire ring. The tungsten wire penetrates a few millimeters through this film (cf. Fig. 3.1). The etching process is started by applying a positive voltage between the tungsten wire (anode) and the platinum ring (cathode). The tungsten wire dissolves to WO_4^{2-} into the solution, while the water is reduced to hydrogen gas H_2 and hydroxide ions OH^- . The chemical equations

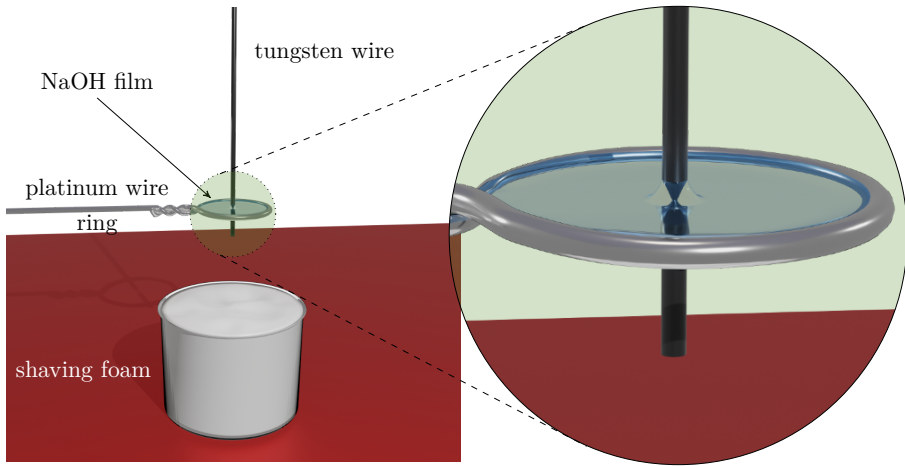
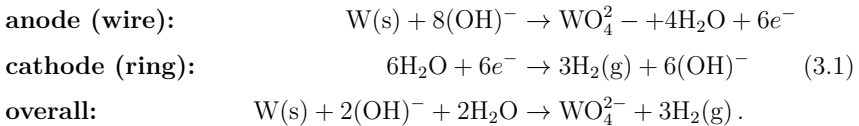


Figure 3.1: Basic structure of the tip preparation system. During the etching process, the anode is the tungsten wire, and the platinum wire ring is the cathode. The meniscus significantly influences the shape of the tip, which can be seen more clearly in the magnification. The shaving foam catches the falling tip.

for the etching process are [92]



The applied voltage is alternated with short pulses of negative polarity. This has the advantage that oxides formed on the tungsten are removed from the tip. The shape of the meniscus (cf. magnified image section in Fig. 3.1) of the NaOH film influences the tip shape during the etching process [92]. When the tapered point of the wire is thin enough that it tears off, the etched tip falls into a glass filled with shaving foam (cf. Fig. 3.1). Each etching process produces two tips, but only the tip that tears off is used. To clean the tip after etching, it is immersed several times in heated distilled water and ethanol. After the tip is checked visually using an optical microscope, it is fixed in the tip holder and ready to be transferred to the load lock of the STM vacuum chamber. This transfer should be done immediately after tip

preparation, such that contamination and oxidation are kept to a minimum.

3.2 Sample preparation

In a conventional STM, the sample surface to be examined is a homogeneous and extended area. However, the samples studied in this work consisted of layered structures grown on a substrate. Conventional in-plane STM can only probe the grown top surface or the substrate, but not the different layers in between (cf. Fig. 3.2a). To obtain images and spectroscopic information of all layers, the samples have to be investigated using a cross-sectional view (cf. Fig. 3.2b). In order to obtain a clean and stoichiometric cross-sectional sample surface, the specimen must be cleaved (cf. Fig. 3.3b). This mode of operation is called cross-sectional STM or short XSTM. It requires precise knowledge about the actual position of the probe tip since the layers are situated close to the edge of the sample surface [24, 93, 94].

Several preparation steps are necessary before a sample can be examined by XSTM: First, the wafer must be cut into smaller pieces with a rectangular shape of 2 mm by 4 mm, using a wire saw. The sample pieces are then thinned to a thickness of 80 to 100 μm , followed by polishing. In the next step, the thinned and polished samples are partly coated using a gold sputtering system. A capacitor is used to obtain disruptive dischargings in the region of the sample's gold layer. This step is required to intermix the gold layer with the underlying material and thus ensure a good ohmic electrical contact. The samples prepared in this way are glued to a

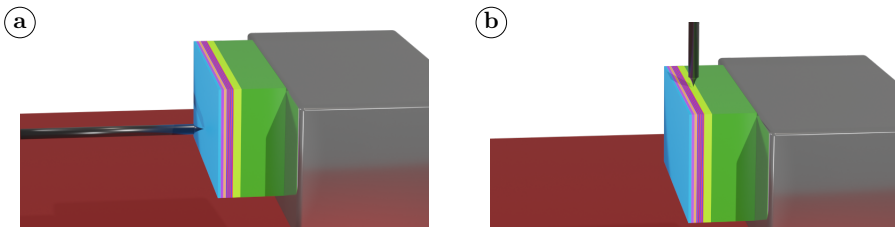


Figure 3.2: (a) Via the conventional STM, a sample surface is directly accessible. (b) In contrast, cross-sectional areas are only accessible with an XSTM arrangement.

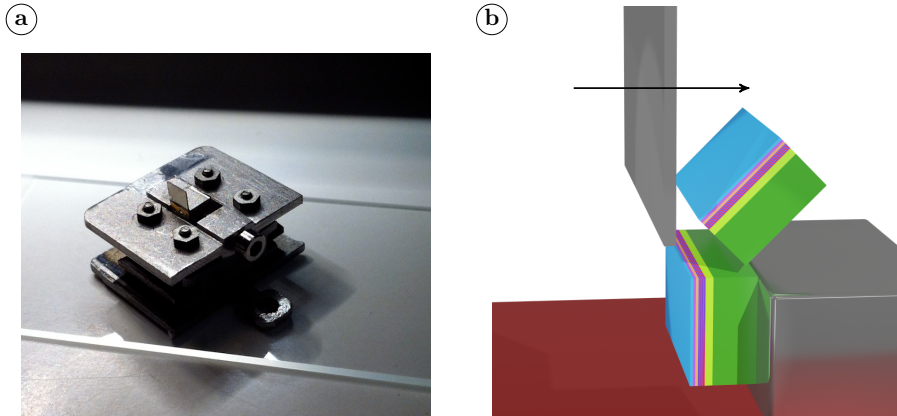


Figure 3.3: (a) Sample holder for the STM [95]. (b) A metal block is moved to the right to cleave the sample.

stainless steel cube with a conductive two-component adhesive. Finally, the samples are then clamped into a sample holder (cf. Fig. 3.3a) and transported into the load lock chamber of the microscope.

The cleavage takes place in the ultra-high vacuum (UHV) of the preparation chamber. Due to the low pressure in the UHV chamber, usually less than $2 \cdot 10^{-10}$ mbar, significant amounts of contamination on the time scales of a few days can be excluded. The high surface sensitivity of the STM implies that even slight contamination can render the measurement unusable.

3.3 Scanning tunneling microscope

In this section, the fundamental technical aspects of the STM will be briefly described. After placing the sample onto the measurement stage of the STM, the tip must first be approached towards the sample up to a distance of less than 1 nm, such that a tunnel current can occur. For this purpose, the STM is equipped with a coarse motor capable of moving the tip in all three spatial directions. This motor is based on shear piezo stacks, which are operated by applying a sawtooth voltage.

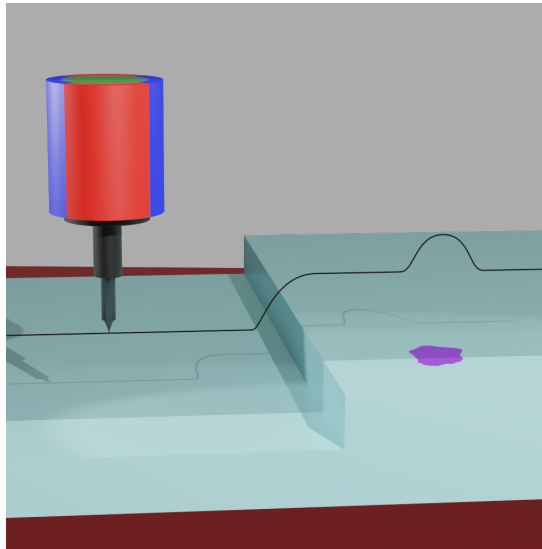


Figure 3.4: Principle of operation of the STM. If the current changes, the tip-sample distance is controlled by a feedback loop. Current changes can occur due to surface irregularities such as steps or electronically different materials.

With the slow-falling voltage flank, the position of the tip is changed, while with the fast-falling voltage flank, the shear piezo stacks slip through. In addition to the coarse motor, a piezo tube is employed to move the probe tip in all three spatial directions with high precision but a smaller range. Approaching the probe tip to a distance of less than one nanometer from the sample surface requires a two-step process: For large distances, the tip is approached manually using an optical microscope and the coarse motor. For smaller distances, an auto approach technique is available. It successively approaches the tip by the coarse motor and probes the existence of a tunnel current by stretching out the piezo tube.

For the acquisition of STM images, a scan range of approximately $16\ \mu\text{m}$ in the x and y direction, i.e., in the sample plane, and $2.4\ \mu\text{m}$ in the z direction is available, mediated by the bending and stretching of the piezo tube.

The STM image is now obtained by scanning the tip line-wise over the sample surface. The movement parallel to the surface is performed by bending the piezo tube in x and y direction (cf. blue and red piezo contacts in Fig. 3.4). In the commonly

used constant current mode, the tip-sample distance is constantly readjusted by a feedback loop such that the measured tunnel current remains constant during the measurement. Technically, this is achieved by a PID controller that uses the tunnel current as input and alters the voltage applied to the piezo tube in the z direction (cf. green contact in Fig. 3.4). This voltage, which is proportional to the z position of the tip, is recorded and eventually yields the STM image. The main contributions to the measured height are, on the one hand, topographic differences (e.g., steps, defects). On the other hand, different electronic contributions like the LDOS (materials with different density of states). For example, heterojunctions typically provide both topographic (through strain) and electronic contributions to the height contrast in STM.

3.4 Samples

3.4.1 Structure of sample A3782/A3787

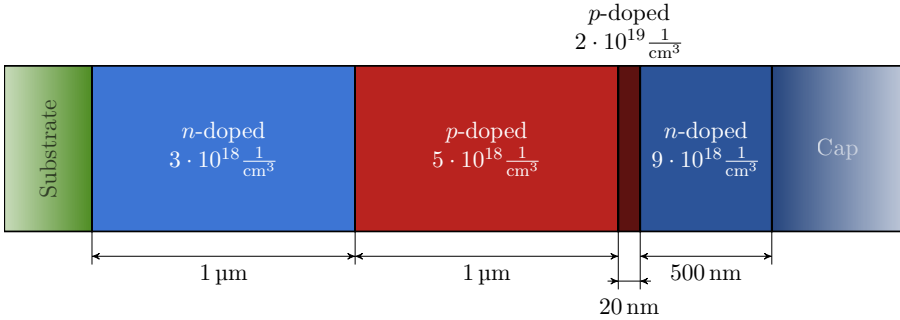


Figure 3.5: Sample structure of the A3782/A3787 sample. On top of a freestanding GaN wafer, a n -doped buffer layer was grown. The n - p - n GaN structure was annealed to activate the p -doped region. Afterward, an n -doped capping layer was grown.

The sample consists of GaN layers with different dopant concentrations and types grown by metal-organic chemical vapor phase epitaxy (MOVPE) on top of a c -plane free-standing hydride vapor phase epitaxy (HVPE)-grown GaN substrate. The consecutive layers form a n - p - n -structure protected by an n -doped capping

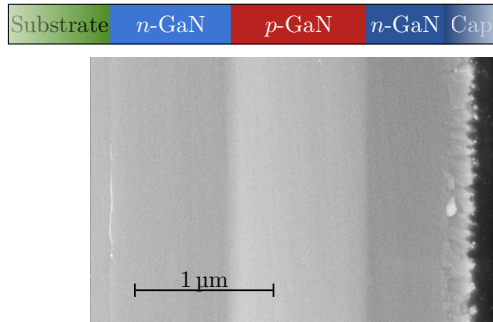


Figure 3.6: SEM image of the sample surface in the secondary electron mode (5 keV). The doping junctions can be discerned well. The substrate sample interface appears as a thin bright line on the left side. The 3D-growth of the capping layer can be seen on the right side of the SEM image.

layer (cf. Fig. 3.5). The doping species of the n - and p -type layers are Si and Mg, respectively. The first $1\ \mu\text{m}$ thick n -doped buffer layer has a nominal doping concentration of $3 \cdot 10^{18}\text{cm}^{-3}$. The $1\ \mu\text{m}$ thick p -doped layer exhibits a nominal doping concentration of around $5 \cdot 10^{18}\text{cm}^{-3}$, followed by a $20\ \text{nm}$ thick p -doped layer with a nominal higher doping concentration of $2 \cdot 10^{19}\text{cm}^{-3}$ capping the p -doped region. The next layer has a thickness of $500\ \text{nm}$ and an n -type doping concentration of $9 \cdot 10^{18}\text{cm}^{-3}$. After this MOVPE run at $960\ ^\circ\text{C}$, the sample was thermally annealed *ex-situ* to activate the Mg dopants at $650\ ^\circ\text{C}$.

In a second run, three highly doped n -type GaN layers with nominal thicknesses of $15\ \text{nm}$, $150\ \text{nm}$, and $5\ \text{nm}$, and Si concentrations of $1 \cdot 10^{20}\text{cm}^{-3}$, $1 \cdot 10^{19}\text{cm}^{-3}$, $1 \cdot 10^{20}\text{cm}^{-3}$, respectively, were grown by MOVPE at a temperature of $715\ ^\circ\text{C}$. However, the two layers with high doping concentration, in the range of $1 \cdot 10^{20}\text{cm}^{-3}$ formed 3D islands. The 3D growth prevents access to these layers through STM. However, by employing scanning electron microscopy (SEM), a polycrystalline region on top of the last layer from the first MOVPE run is unraveled. Within this region, no distinct layers are discernible (cf. Fig. 3.6). Due to the rather low quality, this region is excluded from further analysis in this thesis.

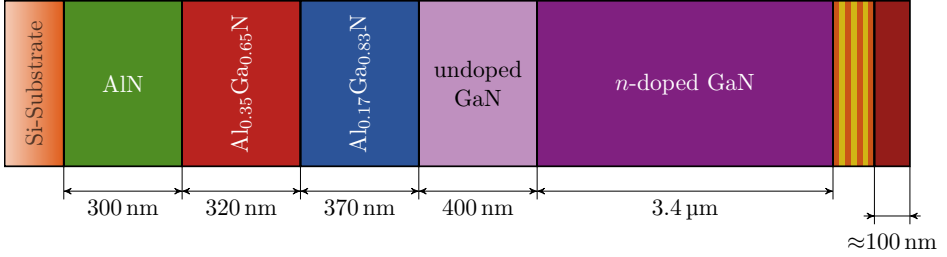


Figure 3.7: Sketch of the LED sample structure. The exact number of quantum wells in the multi-quantum wells is unknown.

3.4.2 Structure of the LED sample

The GaN-based LED-sample structure investigated in this thesis is based on a layered system designed for a nitride multi-quantum well embedded in an n - and p -type GaN layer. In order to reduce production costs, the LED structure was grown on top of a standard Si(111) substrate. However, due to lattice mismatch and strain, as well as back-etching, epitaxial growth of GaN on Si can only be realized by introducing several intermediate layers that can reduce strain.

The very first of the buffer layers on top of the Si substrate is a nominally undoped, 300 nm thick AlN layer [96], which is known to exhibit a smaller lattice mismatch of Si compared to GaN and avoids back-etching. This layer is followed by a 690 nm thick step graded (Al,Ga)N layer with increasing Ga content, representing the transition to GaN. It has been shown that most of the dislocations are relieved in this layer [96]. The AlGa_xN layer can be subdivided into two layers with different Ga content.

The first layer is a 320 nm thick $\text{Al}_{0.35}\text{Ga}_{0.65}\text{N}$ layer [96]. The second one has a thickness of 370 nm and a Ga content of 83 % [96]. The intermediate or buffer layers are completed by an undoped GaN region with a thickness of 400 nm. On top of that, the electrically active layers were grown epitaxially, starting with a 3.4 μm thick Si-doped (n -type) GaN layer, followed by a multi-quantum well structure with an unknown layer sequence. The capping layer consists of several p -doped sub-layers and is approximately 100 nm thick.

This work focuses on the analysis of the buffer layers since strain management and the electrical properties associated with the ternary nitride alloys are nowadays of particular interest. This is the reason why the first four layers are of particular interest to this work.

Chapter 4

Investigation of the influence of various physical parameters on tunnel currents simulated for *n*-type III-nitride ($10\bar{1}0$) semiconductor surfaces

This chapter investigates the influence of various physical parameters on tunnel currents, simulated for *n*-type III-nitride ($10\bar{1}0$) semiconductor surfaces. The physical parameters discussed here are the semiconductors band gap, the electron affinity, the tip radius, the tip work function, the doping concentration, and the energy position of the empty intrinsic group III-derived dangling bond state within the band gap. It turns out that, in particular, the electron affinity and the position of the surface state affect the tunnel currents decisively, while the dopant concentration and the band gap play a minor role on these surfaces. The physical origin of this unexpected behavior of the tunnel current can be found in the electronic properties of the GaN ($10\bar{1}0$) surface. The surface exhibits (a) a filled intrinsic dangling bond state at the valence band edge, which is not influencing the surface Fermi level, and (b) an empty dangling bond state in the fundamental band gap, which induces in STM operation a polarity dependent Fermi-level pinning [38]. This results in a Fermi-level pinning at positive voltages, while at negative voltages no pinning

occurs under tunneling conditions. This constellation is taken as basis for the simulations in this chapter. The findings obtained from the analysis in this chapter are used for the discussion of spectra in Chapter 5 and the fits performed in Chapter 6 for ternary (Al,Ga)N alloys. In addition, they are a guideline for determining sensible fit parameters for future tunnel current simulations.

4.1 Introduction

The tunnel current between a metal probe tip and semiconductor surfaces is usually composed of various components. In the simplest case, i.e., under the assumption of negligible tip-induced band bending as well as the absence of intrinsic surface states in the fundamental band gap, electrons tunnel from filled valence band states (tip states) into empty tip states (conduction band states), if a negative (positive) sample bias of sufficient magnitude is applied [22].

However, the free charge carrier concentration of semiconductors is typically orders of magnitude smaller than that of metals, and thus the electrostatic potential being present in the vacuum region between tip and sample penetrates into the subsurface region of the semiconductor, leading to a tip-induced band bending [22, 76, 97], as discussed previously in Chapter 2. The electrostatic potential difference between tip and sample is the sum of their contact potential (i.e., work function difference) and the applied voltage. The magnitude and extent of the potential that penetrates the semiconductor surface and leads to band bending depend on both the free carrier concentration and the permittivity [76].

For doped semiconductors, tip-induced band bending can create electron or hole accumulation or inversion, which can be the source of other tunnel current components. Such components are known to reduce the voltage range without tunnel current in $I(V)$ spectra (also called the apparent band gap) significantly. In addition, surface states present within the fundamental band gap can alter the band bending and further complicate understanding the measured tunnel currents. Hence, the simulation of tunnel spectra is necessary for achieving both a qualitative and a quantitative understanding of the complex interplay of surface- and tip-related effects at group III nitride semiconductors.

This chapter discusses the variation of the most important semiconductor parameters that influence the tunnel current of non-polar GaN surfaces. [38] Two different software packages for simulation are employed for this purpose: P_SpaceChargeLight developed by Schnedler [79, 98, 99] as well as SEMITIP developed by Feenstra [76, 100, 101]. The results of both packages are quite similar, as discussed in the following section.

4.2 General remarks on the simulation packages used

Both simulation packages utilize finite difference methods (cf. Sec. 2.4.1) to solve the Poisson equation and obtain the three-dimensional electrostatic potential of the tip-vacuum-semiconductor system. Both approaches consider a hyperbolic tip geometry, the interface boundary conditions at the transition from vacuum to the semiconductor, and are capable of treating surface states. It is worth mentioning that surface states are incorporated from the electrostatics point of view. Tunneling between the tip and the surface states is not provided by any of the software packages. However, due to slight differences in, e.g., the image potential, the coordinate systems, and their symmetry, the treatment of non-equilibrium charge carriers, and the derivation of tunnel currents, some deviations may appear in the results, which are physically negligible, at least for GaN.

Regarding technical aspects, SEMITIP returns a tunnel current density in the units of A/nm^2 , while P_SpaceChargeLight returns a tunnel current in A , assuming a fixed tunneling area of 1 nm^2 . However, the major difference between the two is that P_SpaceChargeLight considers the image potential at the surfaces of both the metal probe tip and semiconductor using the approximation described in Ref. [67] divided by two [102] for the calculation. In contrast, the UniInt3 application from the SEMITIP simulation package used in this work does not take into account image potentials. The author of the software rather suggests multiplying the resulting current densities with a constant factor of about 1000 to account for both the tunnel area and the image potentials [76]. This situation is illustrated in Fig. 4.1,

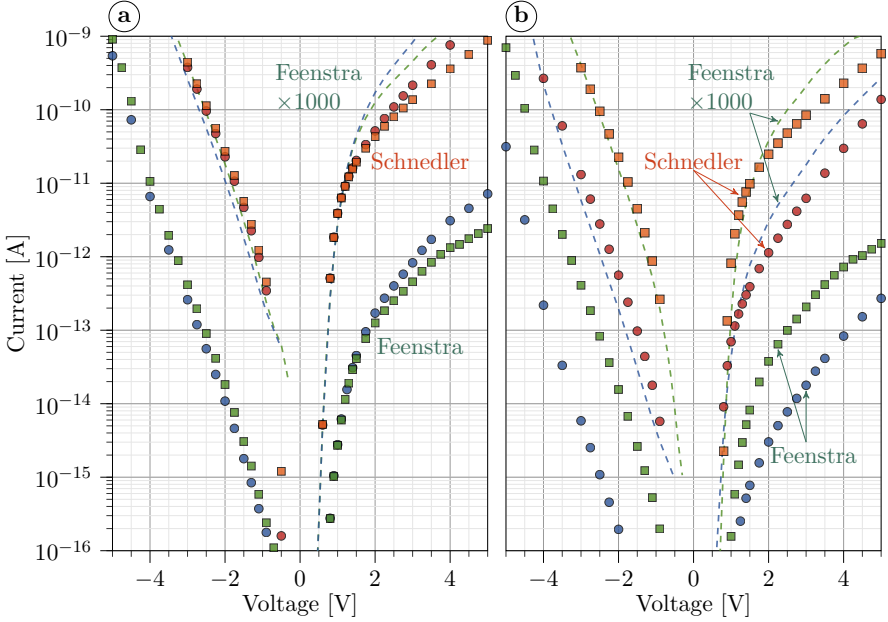


Figure 4.1: Tunnel spectra in logarithmic scale derived by SEMITIP (blue circles, green squares) and P_SpaceChargeLight (red circles, orange squares). The dashed lines are the $I(V)$ curves derived by SEMITIP and multiplied with a constant factor of 1000 in order to match them with the $I(V)$ curves derived by P_SpaceChargeLight. (a) The red and blue circles correspond to a tip radius of 10 nm, while the orange and green colored squares correspond to a tip radius of 50 nm. All the spectra were derived assuming the same tip-sample separation and doping concentration of $d = 10 \text{ \AA}$ and $N_D = 3 \cdot 10^{18} \text{ cm}^{-3}$, respectively. (b) in contrast to (a), all spectra are derived using the same tip radius of 10 nm, but other parameters were changed: For the red and blue symbols, the tip-sample separation is changed to $d = 12 \text{ \AA}$, and the doping concentration is changed to $N_D = 3 \cdot 10^{16} \text{ cm}^{-3}$ for the orange and green spectra.

where tunnel spectra, simulated with P_SpaceChargeLight (red circles and orange squares) and SEMITIP (blue circles and green squares), are shown for comparison. Figure 4.1a shows tunnel spectra simulated for two different tip radii of 10 nm (blue and red circles) and 50 nm (green and orange squares). For both tip radii, the results of UniInt3 need to be multiplied (i.e., offset) by a factor of around 1000 (dashed lines) to match the simulated tunnel spectra of P_SpaceChargeLight close to the current onsets voltages. In analogy to the tip radius, the tip-sample

separation and the doping concentration have been varied from 10 Å to 12 Å and from $3 \cdot 10^{18} \text{ cm}^{-3}$ to $3 \cdot 10^{16} \text{ cm}^{-3}$, respectively. Figure 4.1b shows the corresponding simulated $I(V)$ curves obtained by both software packages. A comparison of the spectra yields again a factor of around 1000 between the $I(V)$ curves of both applications (dashed lines). Hence, it is concluded that the factor is, in first approximation, independent of most of the simulation parameters. Under this assumption, a quantitative comparison of the results of both simulation software packages can be performed.

Nevertheless, at large absolute voltages, small deviations arise, either due to the different tunnel current models employed in the simulation packages or due to numerical errors caused by finite difference algorithms applied to different coordinate systems (hyperbolic vs. Cartesian). Furthermore, the ratio between the tunnel currents derived with and without image potentials (using P_SpaceChargeLight) is voltage-dependent and increases by a factor of ≈ 2 for larger sample voltages.

In the following the simulation program SEMITIP is used, and the resulting spectra are multiplied by a factor of 1000. As shown above, the results are, however, comparable with those of P_SpaceChargeLight.

4.3 Exponential dependence of the tunnel current on the tip-sample separation

First, the dependence of the tunnel spectra on the tip-sample separation is examined in more detail. As mentioned in Sec. 2.1 (cf. Eq. 2.13) at the beginning of Chapter 2, the transmission probability and, thus, the tunnel current depends exponentially on the tip-sample separation in first approximation [60, 66, 67, 70, 103]:

$$I \propto \exp\left(-2 \cdot \kappa \cdot d \left[\text{\AA}\right]\right). \quad (4.1)$$

In Eq. 4.1, the decay constant κ is roughly $\approx 1.09 \text{ \AA}^{-1}$, if a work function of 4.5 eV is assumed [22, 49]. From this relation, it can be concluded that a tip-sample separation change of roughly 1 Å changes the tunnel current by one order

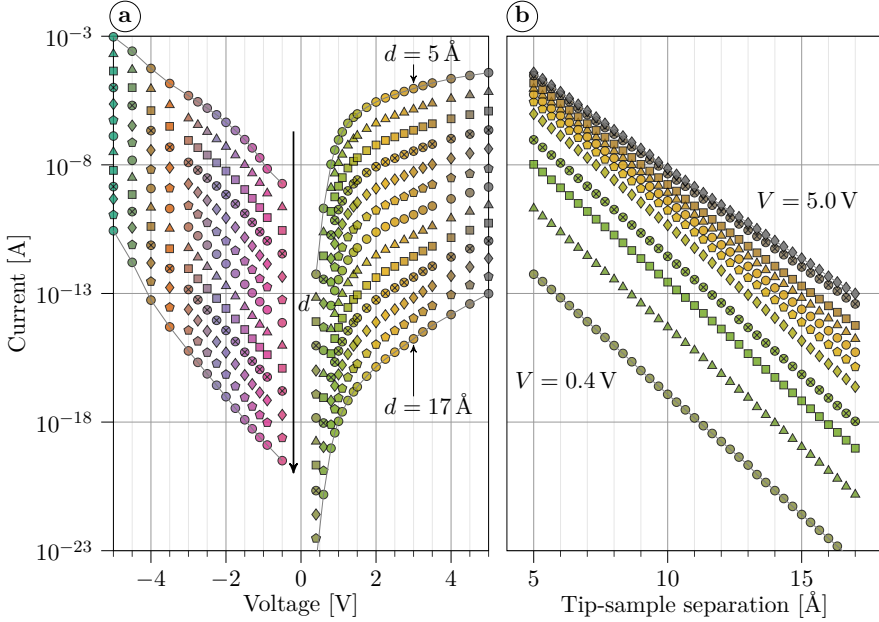


Figure 4.2: (a) Simulated $I(V)$ spectra at various tip-sample separations, ranging from 5 Å (top) to 17 Å (bottom) and with a step width of 1 Å. (b) Tunnel current as a function of tip-sample separation of the positive current branch. The color-coding of the symbols in (b) corresponds to the applied voltage, i.e., the horizontal axis in (a): Each symbol color in (b) is related to a specific voltage point of the positive current branch in (a).

of magnitude. However, these estimations do not consider the effect of the tip-induced band bending, which depends, to a certain degree, also on the tip-sample separation.

Thus, it is worth assessing the relation of the tip-sample separation and the tunnel current in detail. Figure 4.2a shows the simulated $I(V)$ spectra for the non-polar GaN surface at different tip-sample separations. A n -type doping ($3 \cdot 10^{18} \text{ cm}^{-3}$) was used, and in accordance with Refs. [34,38], a polarity-dependent surface Fermi-level pinning was assumed. The corresponding Ga-derived dangling bond surface state was modeled as Gaussian distribution of states with a full width at half maximum (FWHM) of 0.1 eV, centered 0.7 eV below the bulk conduction band edge. The total density of states of the Gaussian distribution was assumed to be $6 \cdot 10^{14} \text{ cm}^{-2}$, which

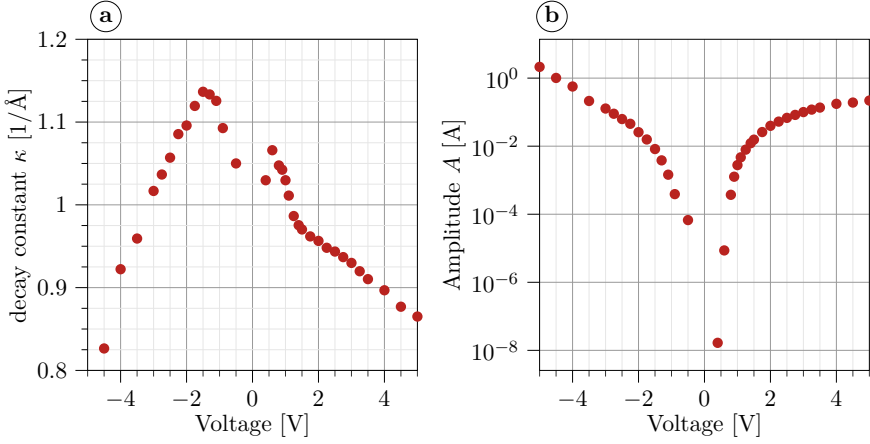


Figure 4.3: The fitted decay constant (a) and amplitude (b) of Eq. 4.1 for every voltage point of the simulated spectra in Fig. 4.2.

corresponds to one state per surface unit cell. The topmost spectrum was derived for the smallest tip-sample separation of 5\AA , while the lowermost spectrum corresponds to the largest tip-sample separation of 17\AA . Figure 4.2b depicts the decay of the tunnel current as a function of the tip-sample separation. The color-coding of the symbols corresponds to the applied voltage and is the same as in Fig. 4.2a. A linear decay in the tunnel current with increasing distance between tip and sample can be seen on a logarithmic scale, i.e., the tunnel current is exponentially decreasing with the tip-sample separation. Figure 4.2b illustrates that the slope of the decay depends on the applied voltage. This is indicative of a voltage dependency of the decay constant κ (cf. Eq. 4.1).

To analyze the voltage dependency of the decay constant κ , Eq. 4.1, is extended by a proportionality constant A and fitted to the $I(z)$ curves presented in Fig. 4.2b. The result of the fits is presented in Fig. 4.3, as a function of voltage in a. First, the decay constant κ is close to the expected literature value of around 1\AA^{-1} [22, 49, 103], and decreases only slightly ($\approx 0.1 \text{\AA}$ to 0.2\AA) for large absolute voltages. Second, two different slopes of the $\kappa(V)$ curve can be discerned for the negative and positive branches. Note that the decay constant κ in Fig. 4.3a is an averaged one, since it is calculated from $I(V)$ curves. However, $I(V)$ curves compromise the density of

states integrated over a certain energy range (from E_F to $E_F + e \cdot V$), with each energy corresponding to a slightly different κ .

Close to the onset voltages, the κ values agree well with the nominal ones of $\approx 1 \text{ \AA}^{-1}$. At larger absolute voltages, a reduced tunneling barrier leads to decreasing average decay constants. It is thus concluded that the exponential decay of the tunnel current due to the increase of the tunnel barrier is the dominant effect for increasing tip-sample separations.

Furthermore, Figure 4.3b shows amplitude A as a function of voltage. The general shape of this function resembles that of the $I(V)$ spectra. The proportionality constant A increases by several orders of magnitudes for large absolute voltages. This is explained by the fact that A contains the integrated density of states, which increases significantly with increasing voltages as well.

4.4 Effects of sample parameters on the tunnel current

The effects of variation of selected sample parameters on computed tunnel currents are discussed below for non-polar GaN surfaces. The results gained in the following section can be transferred and applied to other non-polar ternary III-N compound semiconductor surfaces if their cation-derived dangling bond state has similar characteristics like that for the GaN ($10\bar{1}0$) surface.

4.4.1 Variations in the band gap

In Fig. 4.4 tunnel spectra are shown for band gaps from 3.09 eV to 3.69 eV. The spectra in were derived assuming a polarity-dependent pinning as described above. Note that the calculated currents for the different band gaps coincide in Fig. 4.4. Hence, in both cases, no dependence of the tunnel spectra on the band gap was found.

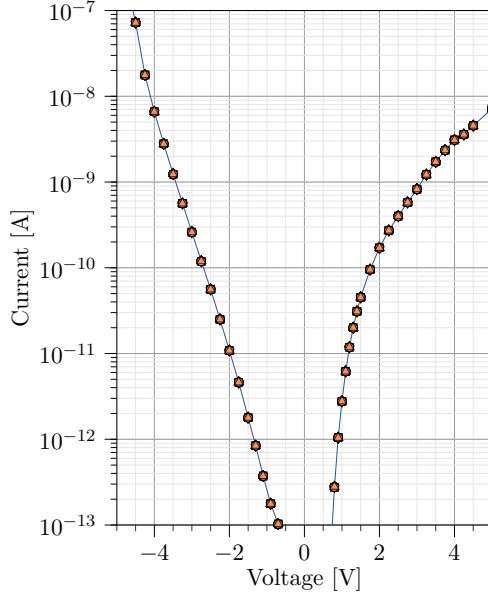


Figure 4.4: $I(V)$ tunnel spectra simulated for different band gaps in a range from 3.09 eV (line) to 3.69 eV, shown as symbols. A polarity-dependent Fermi-level pinning induced by an intrinsic surface state 0.7 eV below the conduction band edge is assumed. Note that tunnel currents at different band gaps coincide for all voltages. No dependence of the tunnel current on the band gap is observed.

For the understanding of the absence of band gap dependence, it is recalled that the empty Ga-derived surface state leads to a polarity-dependent Fermi-level pinning and thus to a shifted onset of the positive voltage branch of the tunnel spectra at the n -doped non-polar GaN (10 $\bar{1}$ 0) surfaces [38]. In contrast, no pinning occurs at negative voltages, and the conduction band is pulled below the Fermi-level, and an accumulation layer can form. Electrons in this layer can tunnel into the tip giving rise to a so-called accumulation current [22, 97, 104–106]. As a result, for both negative and positive voltages, conduction band states are probed. Only at large negative voltages (i.e., $V \ll -3.4$ V), one could probe valence band states in principle. However, due to the larger tunnel barrier related to the valence band states, valence band currents can be neglected in the present case. Without tunnel currents that originate from valence band states, STM becomes insensitive to the

band gap. Therefore, the band gap is not expected to impact the tunnel currents at this surface.

4.4.2 **Effect of the variation in the energy of surface states**

The presence of the Ga-derived dangling bond state in the fundamental band gap of *n*-type non-polar GaN surfaces and its implications on the tunnel current has been discussed in Sec. 4.3 and 4.4.1, already. Here, the focus is on the impact of the variation in surface state energy on the tunnel current. Such a variation influences the onsets voltages and slopes of the tunnel currents, as discussed in the following.

The surface state is again modeled by a Gaussian distribution of states with an FWHM of 0.1 eV and a total (integrated) density of states of $6 \cdot 10^{14} \text{ cm}^{-2}$, which corresponds to one state per surface unit cell. The centroid energies of the Gaussian distribution are varied in steps of 0.1 eV in a range of 0 eV and 1.4 eV below the bulk conduction band edge. The resulting $I(V)$ spectra are shown in Fig. 4.5a.

By shifting the centroid energy of the surface state further towards the mid band gap position, the onset of the tunnel spectra is moved to higher voltages (cf. Fig. 4.5a). The currents are found to converge towards large positive voltages, despite different centroid energies.

This effect is even more evident in Fig. 4.5b, where the tunnel current is shown in logarithmic scale as a function of the surface state's centroid energy: For smaller positive voltages (white in Fig. 4.5), a shift of the centroid energy position changes the tunnel current strongly. In contrast, for larger voltages (green in Fig. 4.5), this influence of a centroid energy shift is much smaller. Hence, all spectra have in common that the influence of surface state induced Fermi-level pinning decreases with increasing positive voltages.

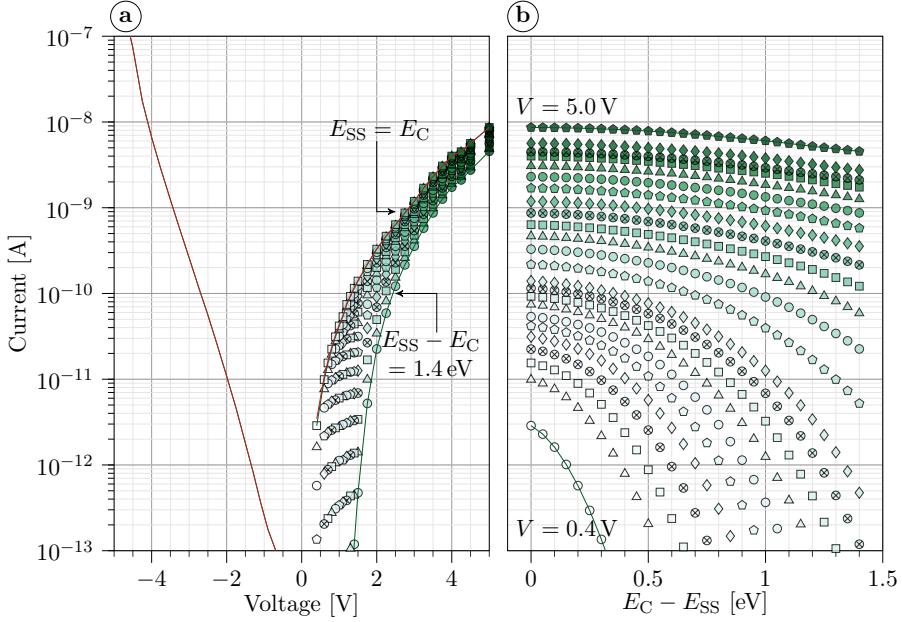


Figure 4.5: (a) Computed $I(V)$ spectra at different centroid energies of the surface state below the conduction band $E_C - E_{SS}$ (ranging from 0 eV to 1.4 eV), with a step width of 0.1 eV. The red line is a tunnel spectrum without any surface state, and the color-coding of the marks in (a) and (b) corresponds to the applied voltage (horizontal axis in (a)). Higher voltages correspond to darker green color. Note, the negative current branch is calculated without pinning by the surface state. (b) Influence of the relative position of the surface state on the measured tunnel current for the simulated voltages.

4.4.3 Effect of the variation in the doping concentration

Next, the influence of the doping concentration on the tunnel current is elucidated. The simulations were carried out assuming both a polarity-dependent pinning as well as an unpinned surface. The doping concentration was varied according to the following sequence: $3 \cdot 10^{14} \text{ cm}^{-3}$, $8 \cdot 10^{14} \text{ cm}^{-3}$, $3 \cdot 10^{15} \text{ cm}^{-3}$, $8 \cdot 10^{15} \text{ cm}^{-3}$, \dots , $3 \cdot 10^{19} \text{ cm}^{-3}$. The donor ionization energy was assumed to be 0.03 eV, which agrees with that of typical dopants, i.e., Si ($0.022 \pm 0.04 \text{ eV}$) and O (0.032 eV to 0.037 eV) [107–109].

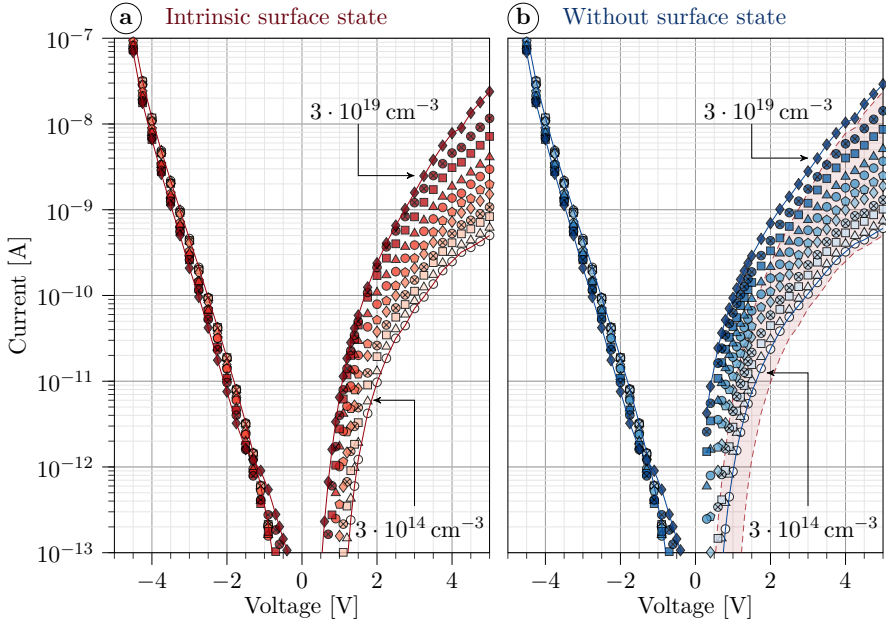


Figure 4.6: Simulated $I(V)$ tunnel spectra for different doping concentrations following the sequence: $3 \cdot 10^{14} \text{ cm}^{-3}$, $8 \cdot 10^{14} \text{ cm}^{-3}$, $3 \cdot 10^{15} \text{ cm}^{-3}$, $8 \cdot 10^{15} \text{ cm}^{-3}$, \dots , $3 \cdot 10^{19} \text{ cm}^{-3}$. Darker colors of the symbols indicate higher doping concentrations. **(a)** Tunnel currents assuming a polarity-dependent Fermi-level pinning, induced by an intrinsic surface state 0.7 eV below the conduction band edge. **(b)** Tunnel spectra for an unpinned surface. For the sake of clarity, the tunnel currents of the pinned surface are also shown in **(b)** as a shaded area.

Figure 4.6a illustrates the corresponding results of the computations that incorporate a polarity-dependent pinning, while Fig. 4.6b depicts the same results for the unpinned surface. Both, Fig. 4.6a and b have in common that the change in doping concentration has only a minor effect on the negative voltage branch of the tunnel spectra. This observation can be understood by recalling that the tunnel current at negative voltages originates from an electron accumulation layer for n -type material. This situation is further elucidated by Fig. 4.7, which illustrates the tunnel current as a function of the doping concentration at **a** negative and **b** positive voltages in case of a surface state 0.7 eV below the conduction band. At negative voltages (cf. Fig. 4.7a), no strong dependence of the tunnel current on

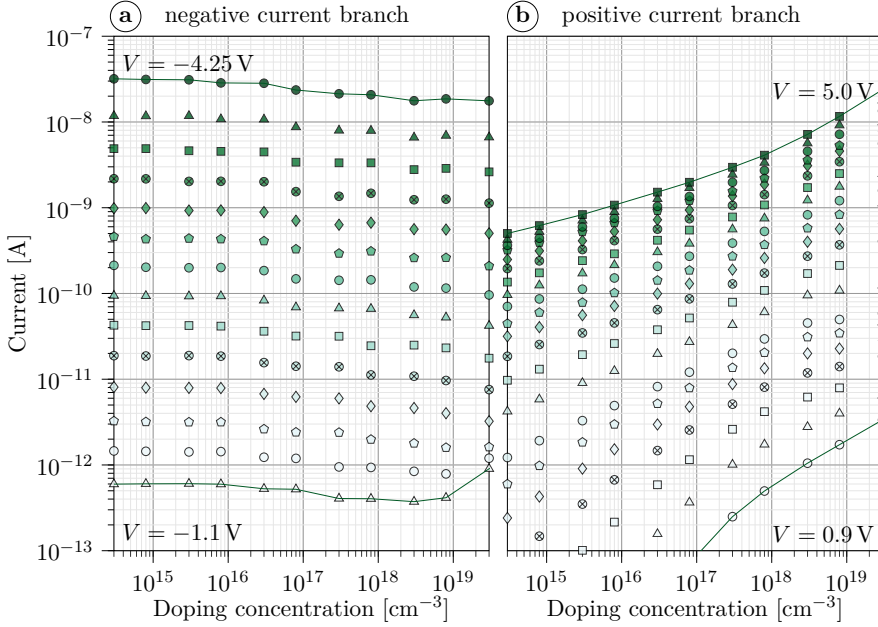


Figure 4.7: Log-log plot of the simulated tunnel currents as a function of the doping concentrations for (a) negative and (b) positive sample voltages (The data is extracted from Fig. 4.6a, i.e., simulated with an intrinsic surface state). Dark green filled symbols correspond to higher absolute voltages than light green symbols. The voltage difference between two adjacent curves is in the range of 0.1 V to 0.25 V.

doping concentration exists for all voltages.

In contrast, for positive voltages, an approximately linear increase of the tunnel current with increasing doping concentrations is visible at all voltages in the log-log plot (cf. Fig. 4.6b). This tendency is independent of the pinning by the surface state, which causes just a shift of the tunnel spectra towards larger positive voltages. The rather strong dependence of the tunnel current on the doping concentration can be understood by considering the screening of electrostatic potentials at the surface and subsurface region of the semiconductor: Both the Ga-derived dangling bond state (dominating at small voltages) and the biased probe tip (dominating at larger voltages) induce a potential at the surface of the GaN sample. This potential penetrates into the semiconductor, where it is successively screened by free carriers.

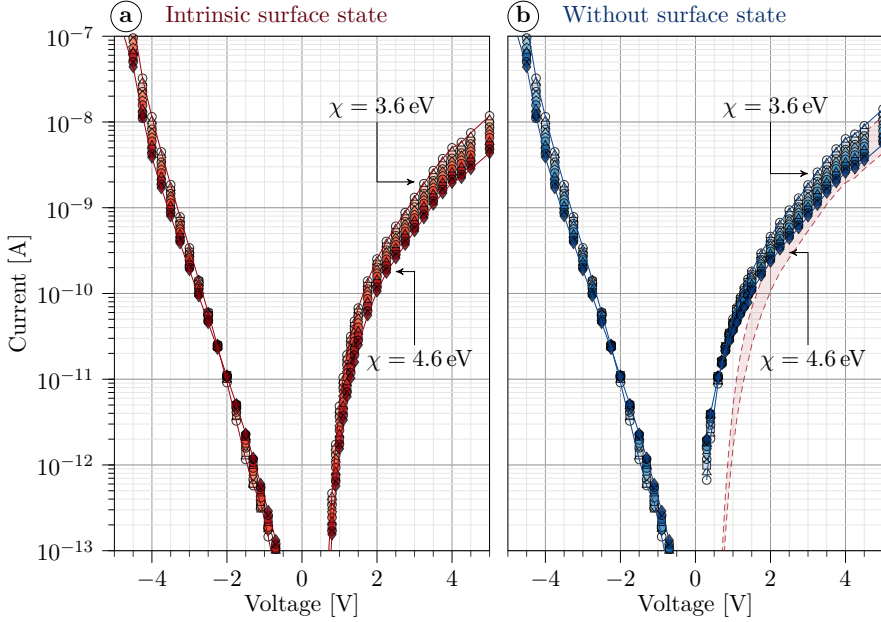


Figure 4.8: Computed $I(V)$ tunnel spectra for electron affinities χ in the range from 3.6 eV (white) to 4.6 eV (darkest color) in steps of 0.1 eV. (a) Simulated with an empty intrinsic surface state 0.7 eV below the conduction band edge. (b) Tunnel spectra for an unpinned surface. For clarity, the tunnel currents of the pinned surface are also shown in (b) as a shaded area.

The screening length and the size of the remaining potential at the surface depend on the free carrier concentration and thus on the dopant concentration.

4.4.4 Electron affinity

Figure 4.8 shows tunnel spectra for different electron affinities χ , between 3.6 eV and 4.6 eV in steps of 0.1 eV. With increasing electron affinity, the onset of the negative current branch is shifted towards smaller absolute voltages. The onset of the positive current branch also shifts to smaller voltages in the unpinned case (cf. Fig. 4.8b), but not in the pinned one (cf. Fig. 4.8a). In addition, the slope of the $I(V)$ curve becomes smaller for both cases with and without a surface state in

the band gap.

For an understanding of these effects, it is recalled that a larger electron affinity leads to a smaller contact potential (cf. Eq. 2.39) and vice versa. The sum of contact potential and applied voltage governs the band bending at the surface of an unpinned semiconductor. If this sum becomes negative, downward band bending is present, and (in the case of n -type material) an electron accumulation zone develops at negative voltages. Thus, a larger electron affinity leads to an earlier onset of the accumulation current. The reduced slope of the $I(V)$ curve is caused by the tunnel barrier, which becomes higher with increasing electron affinities.

For positive voltages, the situation is similar to that at negative voltages: A larger electron affinity decreases the contact potential, which in turn leads to an earlier onset of the positive current branch. In fact, this is only the case for the unpinned surface (cf. Fig. 4.8b). However, experiments unraveled a pinned situation in reality [34,38]: A surface Fermi-level pinning caused by the Ga-derived dangling bond state at the non-polar GaN surface is responsible for an upward band bending of ≈ 0.7 eV at positive voltages. This upward band bending is nearly independent of the contact potential and the applied voltage, provided that it is not too large. Considering that the band bending is not altered by the electron affinity, changes of the tunnel current can only stem from different tunnel barrier heights. This is indeed the case, as demonstrated by the tunnel spectra depicted in Fig. 4.8a: The $I(V)$ curves that correspond to smaller electron affinities and thus smaller tunnel barriers exhibit higher tunnel currents at all positive voltage points. Note again that this is not the case for the tunnel spectra of the unpinned surface (cf. Fig. 4.8b), where the current corresponding to larger electron affinities is higher for small voltages ($V < 0.7$ V), while for larger voltages, the current corresponding to smaller electron affinities dominates.

4.5 Tip specific parameters

Commonly, not much is known about the probe tip's precise geometry and electronic properties in STM/STS experiments. Thus, it is crucial to investigate the influence of varying tip parameters on the tunnel current. This will provide insight into the

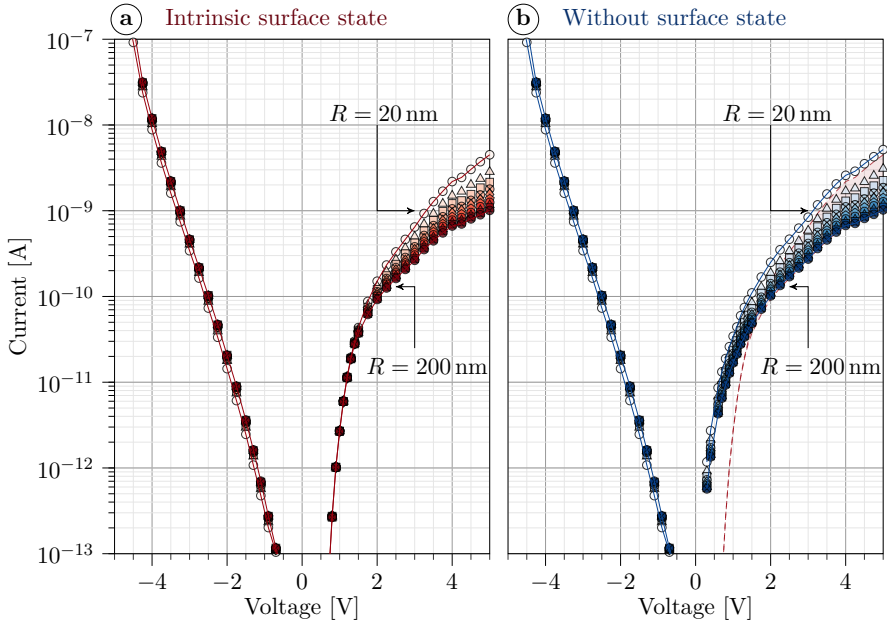


Figure 4.9: $I(V)$ spectra for tip radii between 20 nm (white open symbols) and 200 nm (darkest color, filled symbols) with 20 nm steps. (a) Depicts the simulated tunnel spectra with an empty intrinsic surface state and (b) without. For clarity, the tunnel currents of the pinned (red) surface are also shown in (b) as a shaded area.

reproducibility of STS experiments when different tips are used. Again, the non-polar GaN surface is employed exemplary to model the semiconductor surface.

4.5.1 Tip radius

Figure 4.9 depicts tunnel spectra computed for different tip radii, ranging from 20 nm to 200 nm. At negative voltages, the tunnel currents increase by a factor of less than 2 if the tip radius is enlarged by more than one order of magnitude. This is similar for the cases with and without a surface state.

The small increase of the tunnel current at negative voltages with tip radius is caused by an enlarged tip-induced electron accumulation zone: For larger tip radii,

the downward band bending increases, giving rise to more electrons in the accumulation zone, able to tunnel into the tip.

For the simulation of the positive voltage branch, again, the differences between the unpinned (cf. Fig. 4.9b) case and the case of a surface Fermi-level pinning by the intrinsic Ga-derived dangling bond state (cf. Fig. 4.9a) have been distinguished. The unpinned surface reveals an increase of the tunnel current at all positive voltages with decreasing tip radius. Note that this is the opposite behavior compared to negative voltages and the magnitude increases for large positive voltages. It can be understood considering the tip-induced band bending again: At positive voltages, tunneling from the tip into the conduction band emerges. The smaller the tip-induced upward band bending, the higher the tunnel current because more empty states of the conduction band overlap energetically with the filled states of the tip. Since a smaller tip radius reduces the upward band bending, it thus increases the tunnel current. The impact of the tip radius on the tunnel current becomes stronger for larger positive voltages. At 5 V, the tunnel current changes by one order of magnitude if the tip radius is enlarged by one order of magnitude. The behavior of the tunnel current for the unpinned and the pinned surface differs only for small positive voltages: For the pinned surface (cf. Fig. 4.9a), the tunnel current is independent of the tip radius for small positive voltages < 0.7 V. The reason is similar to that described before in Sec. 4.4.4: At small positive voltages, band bending at the surface of the semiconductor is dominated by pinning and not by the tip's potential. At larger positive voltages, the tip-induced band bending dominates, and thus the currents of the unpinned and pinned surface approach each other.

Note, in the simulation the tunneling area was kept independent of the tip radius for comparability purposes. In addition, a change of the tip-sample separation results in a similar effect as discussed before. In practice, both the tip-sample separation and the tip radius are unknown quantities, and the feedback controller will adjust the absolute tip-sample separation to compensate offsets in the tunnel current caused by different tunnel areas.

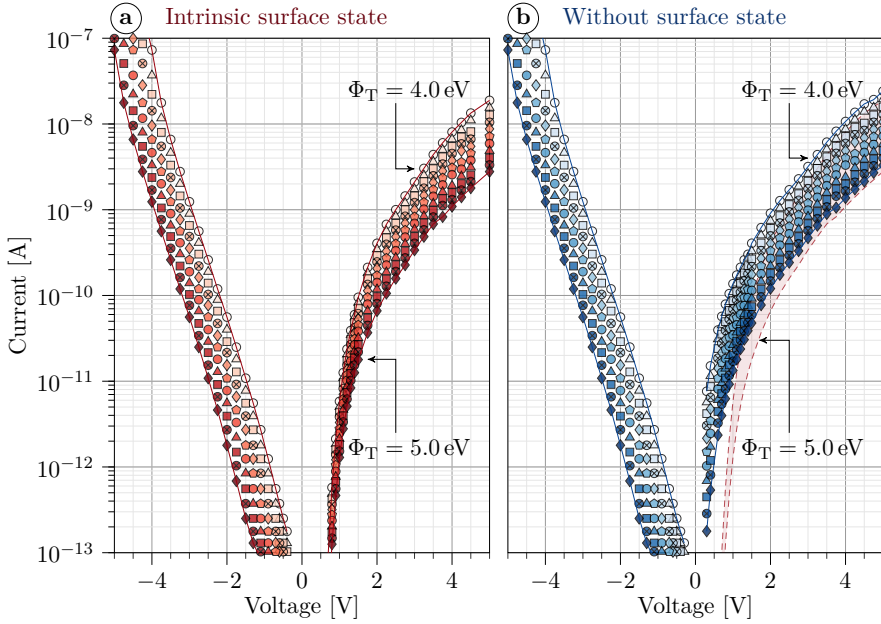


Figure 4.10: Simulated $I(V)$ spectra for tip work functions in a range from 4.0 eV (white) to 5.0 eV (darkest color) and an interval of 0.1 eV. (a) Shows the tunnel spectra for an empty intrinsic surface state 0.7 eV below the conduction band edge. (b) Depicts the unpinned surface. For clarity, the tunnel currents of the pinned (red) surface are also shown in (b) as a shaded area.

4.5.2 Tip work function

Closely intertwined with the electron affinity χ of the semiconductor is the work function of the tunnel tip Φ_T in terms of its influence on the contact potential (cf. Eq. 2.39).

Figure 4.10 shows tunnel spectra computed for tip work functions in the range from 4.0 eV to 5.0 eV. For the unpinned case, the tunnel spectra are shifted rigidly downwards on the current axis for increasing work functions. Two effects are responsible for the observed behavior. First, the tunnel barrier increases with increasing work function. Thus, the probability of electrons tunneling between the tip and the sample reduces. Second, an increased work function and thus a larger contact potential

shifts the conduction band edge upward, i.e., away from the Fermi level. Since the tunnel current arises from electron tunneling out of or into conduction band states for both polarities, the onset voltages of both current branches are shifted to larger absolute values.

In the case of a surface Fermi-level pinning (cf. Fig. 4.10a), the downward shift with work function is also present, but the onset voltage of the positive current branch is less affected by the change in work function (smaller shift range). This is again due to the fact that the band bending at the surface of the semiconductor is not dominated by the tip but by the Ga-derived dangling bond state, at least for small positive voltages. Hence, for these voltages, the current only changes due to the change in the tunnel barrier.

Compensating an electron affinity change with the tip work function

The contact potential depends on the difference between the tip's and the semiconductor's work function. Hence, a change of the sample's electron affinity can be compensated by a simultaneous change of the tip's work function while keeping the contact potential, and thus the tip-induced band bending constant. Only the height of the tunnel barrier is changed. In Fig. 4.11, tunnel spectra are shown for the case of a constant contact potential of 0.4 eV. The electron affinity and tip work function are changed simultaneously in the ranges from 3.6 eV to 4.6 eV and from 4.0 eV to 5.0 eV, respectively, in steps of 0.1 eV. The spectra exhibit a rigid shift for the unpinned case, which is slightly reduced for the pinned case at small positive voltages.

This can be understood as follows: A higher tunnel barrier decreases the probability of electrons tunneling between tip and sample and thus reduces the tunnel current. As a result, the $I(V)$ spectra are shifted on the current axis (cf. Fig. 4.11).

The surface Fermi-level pinning at positive voltages is again responsible for an almost unchanged onset of the current branch in Fig. 4.11a, while the unpinned surface exhibits a more uniform shift of the $I(V)$ curves (cf. Fig. 4.11b).

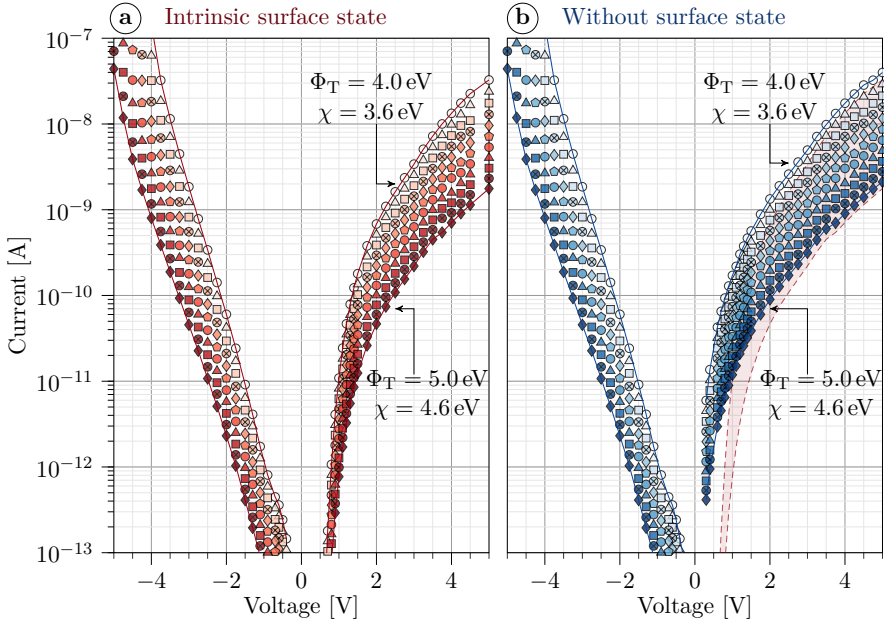


Figure 4.11: $I(V)$ tunnel spectra simulated for a constant contact potential of 0.4 eV. The electron affinity and tip work function are varied in the ranges from 3.6 eV to 4.6 eV and from 4.0 eV to 5.0 eV, respectively, in steps of 0.1 eV. The graphs for $\Phi_T = 4.0$ eV, $\chi = 3.6$ eV and $\Phi_T = 5.0$ eV, $\chi = 4.6$ eV are white and the darkest color, respectively. For clarity, the tunnel currents of the pinned (red) surface are also shown in (b) as a shaded area.

4.6 Conclusion

In this chapter, the influence of the variation of various physical parameters of non-polar GaN sample surfaces and the probe tip on tunnel spectra was investigated using tunnel current simulations. The simulated tunnel spectra obtained by both available simulation packages SEMITIP and P_SpaceChargeLight for the same set of parameters yield almost identical current onsets and slopes close to the onsets if the appropriate image potentials and related tunneling areas are considered.

While the tunnel spectra were found to be independent of a change in band gap, other material parameters and physical quantities have a large impact on the cur-

rent onsets and slopes of the $I(V)$ curves.

Increasing (decreasing) the potential barrier via either the tip work function or the electron affinity of the semiconductor, or both, decreases (increases) the simulated tunnel current.

Accumulation currents are almost independent of many parameters, i.e., doping concentration, electron affinity, tip radius.

Tunnel currents other than accumulation currents are strongly dependent on the band bending (either tip-induced or pinning-induced) at the sample's surface. Thus these currents can be used to gain information about sample parameters, such as the doping concentration and the electron affinity.

These results are used in the following chapters to understand and interpret tunneling spectra quantitatively in conjunction with carefully performed simulations of the tip-vacuum-semiconductor system and hence of the tunnel current.

Chapter 5

Investigation of Fermi-level pinning induced by intrinsic and extrinsic surface states at n - and p -type GaN ($10\bar{1}0$) surfaces

Text and images of this chapter were adapted in parts from the previously published article [P2] (see list of own publications, p. 135) © 2020, Journal of Applied Physics, AIP Publishing.

Fermi-level pinning by extrinsic and intrinsic surface states, as well as their passivation, has been the subject of numerous STM studies at surfaces of n -type GaN [34, 37, 38, 105, 110, 111]. However, similar experiments are still lacking for their p -type counterparts, despite the relevance of such investigations, e.g., understanding the effects of non-polar ($10\bar{1}0$) sidewalls on p - n -junctions in nanowires. In this chapter, non-polar ($10\bar{1}0$) cleavage surfaces of MOVPE grown high quality p - and n -type GaN epitaxial layers are investigated and characterized electrically and structurally by SEM, secondary ion mass spectrometry (SIMS), STM, and STS. Particular emphasis will be put on the changes of UHV cleaved surfaces due to air exposure.

For the clean m -plane GaN ($10\bar{1}0$) surface, it is found that the Ga-derived acceptor-like surface state dominates the Fermi-level pinning for n -type material, while for

p-type GaN the main contribution is attributed to extrinsic Fermi-level pinning caused by cleavage steps. After air exposure, hydroxylation leads to passivation of both extrinsic and intrinsic surface states for *n*- and *p*-type GaN.

5.1 Experimental results

5.1.1 SIMS investigation

The sample A3782/3787 was first investigated by SEM and SIMS to obtain information about the layers' crystal quality, thickness, and doping concentrations. The SIMS measurements were carried out using a TOF.SIMS 5.NCS system from IONTOF GmbH (cf. Figs. 5.1, 5.2, and 5.3). The system is equipped with a reflectron time of flight (TOF) analyzer and two ion guns that are used alternately to ablate material and probe the chemical composition. Depending on the required polarity, either Cs⁺ ions (2 keV, 169 nA, negative polarity) or O₂⁺ ions (1 keV, 310 nA, positive polarity) are employed as primary sputter beam to ablate a 300 × 300 μm² wide square. In the center of this square, a Bi⁺ (30 keV, ≈ 2.5 pA) ion beam is used for composition probing in an area of approximately 60 × 60 μm².

First, a qualitative analysis of the SIMS profiles at negative and positive polarity is provided. The time axis of the SIMS data was calibrated to the penetration depth of the ion beam with the help of the layer thicknesses obtained by SEM (cf. Fig. 5.5a). The SIMS measurement at negative polarity provides information about the Si ion intensity, i.e., the *n*-type dopant species in these samples [112–115]. The results are illustrated in Fig. 5.1. First of all, the SiN⁻ intensity profile (blue line) reproduces the layer structure: The *n*-type layers are discernible by their high SiN⁻ signal (counts > 100). The *p*-type layer can be distinguished by the low SiN⁻ intensity counts (< 10). The peak (counts > 1000) at position 200 nm indicates the beginning of the growth of the capping layer. Another prominent feature of the SiN⁻ intensity profile is the peak between the substrate and the buffer layer at spatial position 2800 nm: Within a narrow region of around 20 nm [P1], the SiN⁻ intensity counts increase by one order of magnitude. Thus this layer is referred to as δ-doped layer.

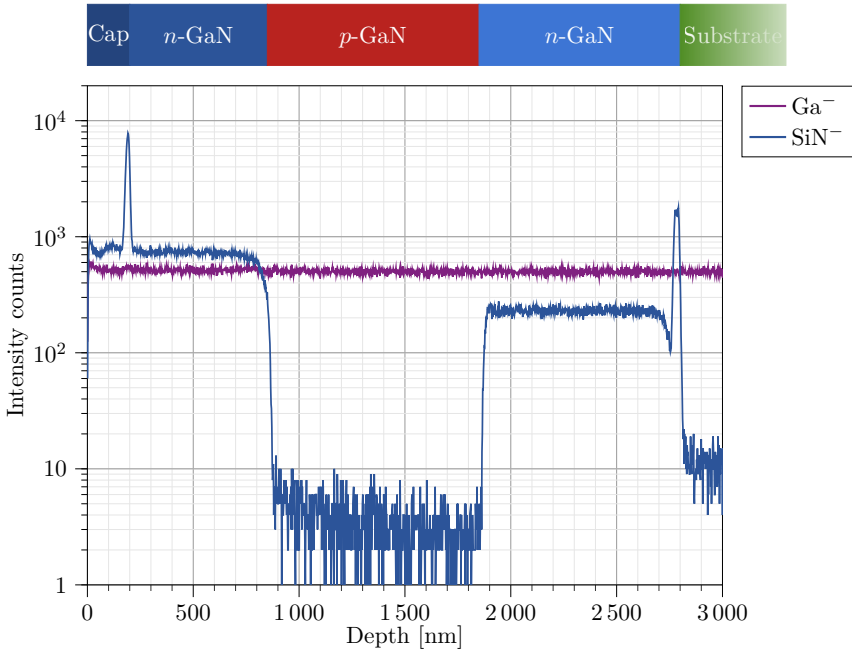


Figure 5.1: SIMS measurement at negative polarity for sample A3782/3787, obtained by sputtering with Cs⁺ ions. At negative polarity, signals of donor atoms have a higher yield rate. In the case of GaN, Si acts as a donor and is the dopant for the two *n*-doped layers.

The SIMS data measured at positive polarity provides access to the *p*-type doping species (here: Mg) with higher secondary ion yield and accuracy [114, 115] as compared to negative polarity [116, 117]. The results are presented in Fig. 5.2. The Mg⁺ intensity profile (orange line) exhibits a peak at the interface between the *p*- and *n*-type GaN layer at spatial position 850 nm. In addition, the Mg⁺ intensity is increasing in growth direction throughout the *p*-doped layer (Note, the growth direction is from right to left in Fig. 5.2). Note, the overall shape of the Si⁺ signal (blue line) in Fig. 5.2 coincides with the one measured at negative polarity (cf. Fig. 5.1). This relation was used for the depth calibration of both graphs relative to each other.

For a quantitative analysis of SIMS signals, a proper calibration of the signals

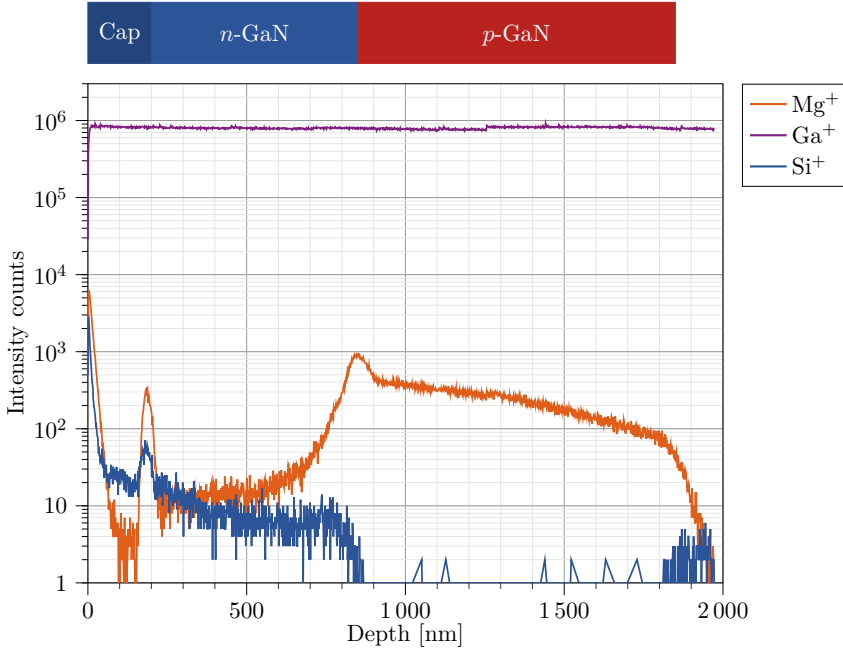


Figure 5.2: SIMS spectra of sample A3782/3787 at positive polarity. The primary sputter ions were O_2^+ . At positive polarity, the signal of acceptor atoms like Mg and, therefore, the p -doped layer is discernible.

is of utmost importance. In this work, an implantation standard sample with a defined concentration of the trace element Mg is used to calibrate the p -type doping concentration. The n -type doping concentration is calibrated by the nominal doping concentration of a GaN buffer layer of $3 \cdot 10^{18} \text{ cm}^{-3}$ from another sample (A3162). Therefore, the n -type doping concentrations can only be compared relative to the known doping concentration of this separate sample.

Next, the Mg^+ and SiN^- ion concentration profiles (cf. Fig. 5.3), which are obtained by calibration of the intensity axis of the SIMS profile (cf. Fig. 5.1 and 5.2), are analyzed quantitatively. The Mg dopant concentration peak at the interface between p - and n - type layer (at spatial position 850 nm) reaches up to $5 \cdot 10^{19} \text{ cm}^{-3}$. The peak concentration is in agreement with the nominal doping concentration of the 20 nm wide highly p -doped layer grown on top of the $1 \mu\text{m}$

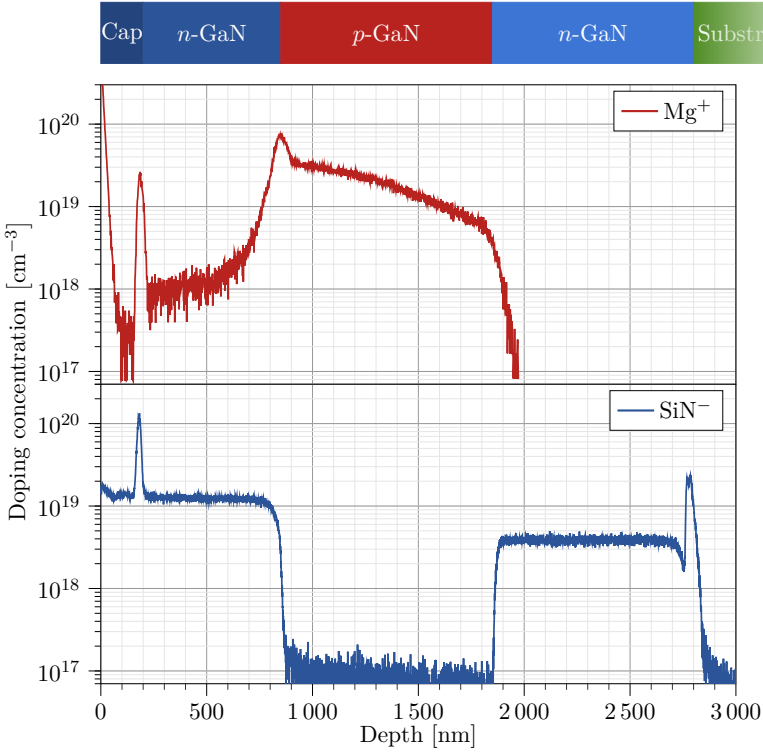


Figure 5.3: Doping concentration was obtained by calibrating the SIMS signal for positive polarity (cf. Fig. 5.2) with an implantation standard and the negative polarity (cf. Fig. 5.1) sample with a known doping concentration of a separate sample.

wide, lower p -doped layer (cf. sample structure in Chapter 3, Fig. 3.5). The lower p -doped layer exhibits an exponential increase (linear on a logarithmic scale) of the Mg concentration from $5 \cdot 10^{18} \text{ cm}^{-3}$ to $3 \cdot 10^{19} \text{ cm}^{-3}$ in growth direction. Hence, on average, the Mg doping concentration in this layer is somewhat higher than the nominal one of $5 \cdot 10^{18} \text{ cm}^{-3}$.

However, it should be noted again that just a small part of the Mg dopants are expected to act electrically as acceptors due to an incomplete activation. The fraction of activated Mg dopants could be decreased even further due to the overgrowth by a n -doped layer before thermal activation. The fraction of activated Mg dopants and thus the actual free carrier concentration in the p -doped layers cannot

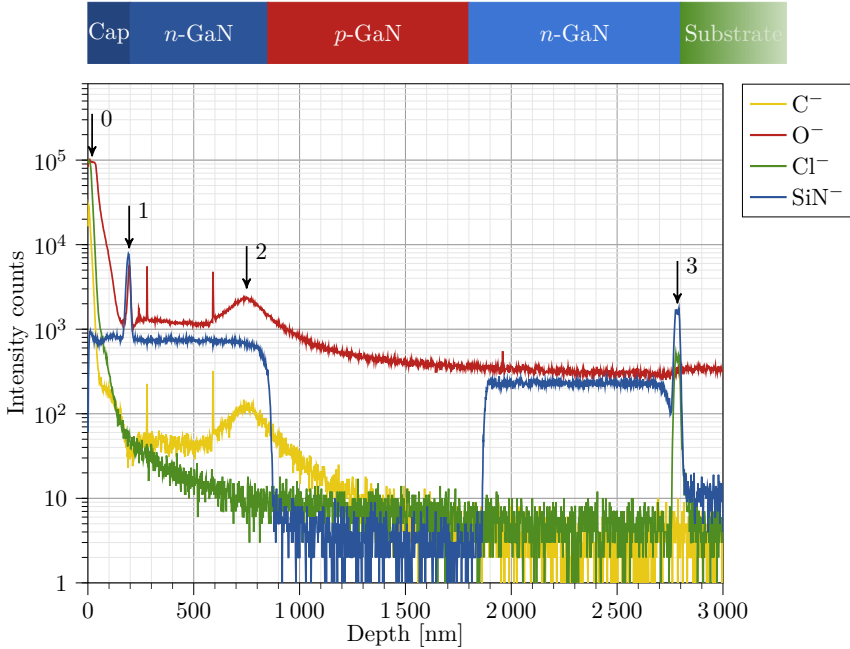


Figure 5.4: SIMS signals for unintentionally incorporated elements O^- , C^- , and Cl^- , probed at negative polarity. The SiN^- signal is shown as a reference to allow comparison with the layer structure.

be determined by SIMS.

The calibrated Si doping concentration of the n -type layers (cf. blue line in Fig.5.3) is close to the intended one: For the capping layer (although polycrystalline), it is above $1 \cdot 10^{20} \text{ cm}^{-3}$ (cf. spatial position 200 nm). The n -type layer next to the cap is about $1 \cdot 10^{19} \text{ cm}^{-3}$, while the buffer layer is at about $3 \cdot 10^{18} \text{ cm}^{-3}$. The δ -doped peak at the substrate buffer interface exhibits a concentration of around $2 \cdot 10^{19} \text{ cm}^{-3}$. Next to this peak in the GaN buffer, the Si concentration is first reduced to $1.5 \cdot 10^{18} \text{ cm}^{-3}$ before $3 \cdot 10^{18} \text{ cm}^{-3}$ is reached (cf. spatial position 2700 nm). The Si concentration of the substrate is below the detection limit. Hence, the n -type conductance of the substrate stems from either oxygen (whose intensity profiles increase slightly in the substrate, cf. Fig. 5.1) or nitrogen vacancies [118–122].

In addition, further ions, i.e., O^- , C^- , and Cl^- , are probed at negative polarity

(cf. Fig. 5.4). Starting at the surface (position 0), the signals of O^- , C^- , and Cl^- show an exponential decay due to entrainment from the surface and enhanced by the 3D growth of the top layer. At position 1, the highly n -doped capping layer (Si doping concentration above $1 \cdot 10^{20} \text{ cm}^{-3}$) was grown after thermal activation of the Mg dopants. The growth after thermal activation could explain the presence of an O peak, and in addition, the Mg peak was detected at positive polarity (cf. Fig. 5.2). At the interface region between the n -doped layer next to the cap and the p -doped layer (at position 2), increased intensity signals for O^- , and C^- can be seen. The presence of O and C indicates contaminations that are incorporated during the growth process or might be caused by a growth interruption. The exponential tail of the O^- and C^- signals could stem from diffusion during post-growth annealing. The layer between substrate and buffer with its δ -like Si doping profile (position 3) also shows an increased content of Cl which usually is introduced by the preparation of the free-standing substrate [123].

5.1.2 Microscopic characterization

Figure 5.5 depicts overview images of the A3782/3787 sample structure (cf. Fig. 3.5) acquired by (a) SEM (cf. Fig. 3.6), (b) current imaging tunneling spectroscopy (CITS), and (c) STM. Each layer of the n - p - n -structure is discernible in all three images (cf. Fig. 5.5a-c). In addition to the n - p - n layers, a bright contrast on the left side of the CITS map and SEM image separates the substrate and the n -type buffer layer. This interface contrast exhibits a spatial width of roughly 20 nm is caused by the aforementioned δ -type Si-doped layer [P1], which was also observed by SIMS with negative polarity (cf. Fig. 5.1, and 5.3). The comparison of all three images reveals that the n - p - n structure has been grown with high epitaxial quality. No growth-related defects are visible (cf. Fig. 5.5a-c). The SEM image reveals that the capping layer exhibits a polycrystalline 3D growth. Possible reasons could be the low growth temperature of 715°C (compared to 960°C for the n - p - n -structure) or high doping concentration. The cleavage surface of a 3D grown crystal bears extreme height changes, which would lead to non-reproducible scan-lines and tip-crashes in the STM. For this reason, the cap layer was not investigated further in the present STM studies.

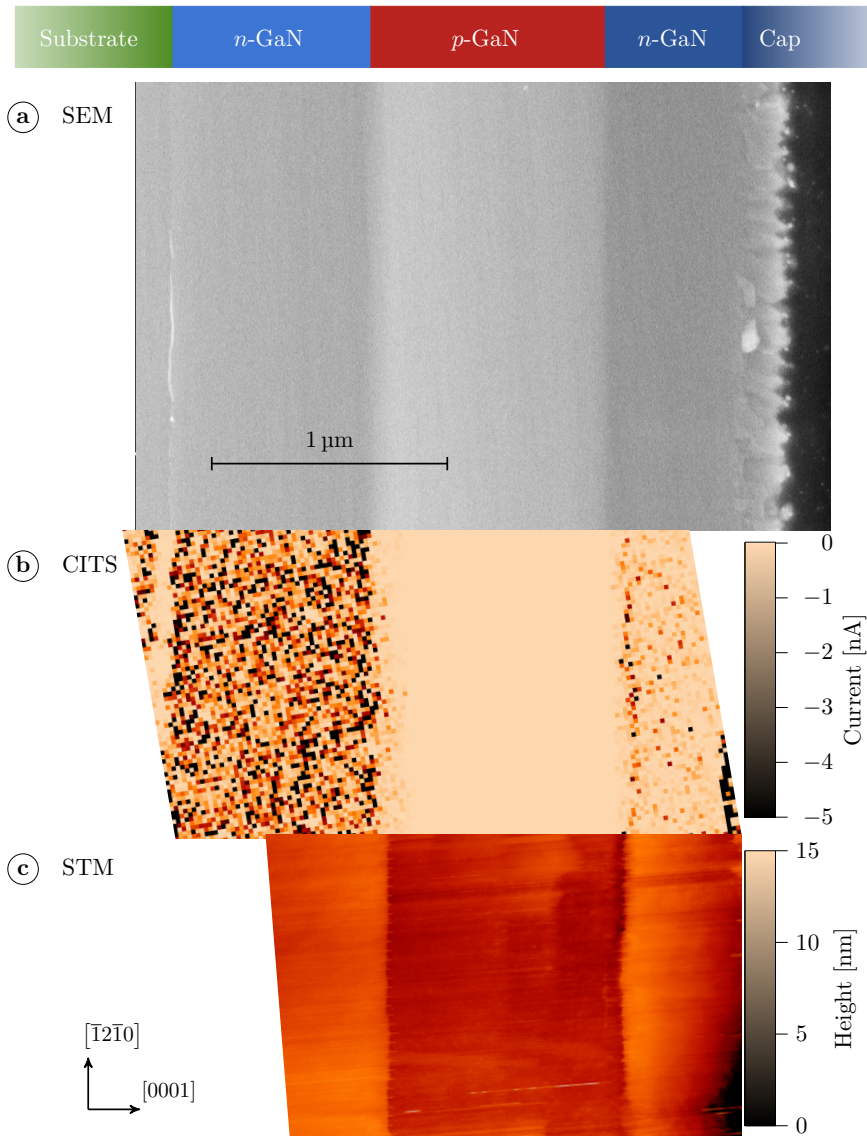


Figure 5.5: Aligned overview images of the n - p - n GaN layer structure. (a) SEM image in the secondary electron mode at 5 keV acceleration voltage. (b) CITS map at -3.2 V (tip-sample distance fixed with setpoint at $+6\text{ V}$ and 80 pA). (c) STM image acquired at a setpoint of -2.5 V and 80 pA . The n - p - n junctions can be recognized well by each of the methods. The CITS map and the STM image were acquired after the SEM analysis and, therefore, after an air exposure of the sample. Reproduced from [P2], with the permission of AIP Publishing.

STM was used to obtain high-resolution images of the surface topography. The STM image in Fig. 5.5b unravels many cleavage steps along the $c[0001]$ direction. In addition to cleavage steps, a rather strong contrast is discernible between the n - p and p - n -junction. This contrast can, however, be an electronic one. If the microscope is operated in the constant-current mode, such an electronic contrast will be translated into a height change in the topographic image.

5.1.3 Tunneling spectroscopy obtained at clean GaN ($10\bar{1}0$) cleavage surfaces in UHV

In order to analyze the electronic properties across the homojunction, STS was measured across the cleavage surface. The corresponding CITS map, evaluated at -3.2 V (cf. Fig. 5.5b), indicates a strong electronic contrast between the n - and p -type region, which in turn can be used to localize the n - p - n homo-structure.

Another representation of the same data set is shown in Fig. 5.6, where the spatial evolution of tunnel spectra (setpoint -4 V and 50 pA) perpendicular to the n - p - n GaN structure is depicted. The image was generated by dividing the rectangular grid that is used to measure tunneling spectra into 23 nm wide subregions (i.e., slices) parallel to the interfaces. The medians of the $I(V)$ spectra in these slices are shown as a function of voltage and spatial position in a logarithmic heat map. Such heat maps will be called tunnel current evolution maps in the following.

The region without measurable tunnel current (i.e., $I < 0.2$ pA) is shown as a yellow and red pixelated area in Fig. 5.6. It is centered around 0 V, with the onset of both negative and positive voltage branches discernible as yellow to green transition (i.e., $I \approx 1$ pA). Higher currents are indicated by blue, magenta, and pink colors. The region without measurable tunnel current will be referred to as the apparent band gap in the following. Comparing Fig. 5.5 with Fig. 5.6 yields a rather large apparent band gap of 3.6 eV in the n -type GaN at spatial positions below 1500 nm. The transition from n -type to p -type doping at 1500 nm is accompanied by a significant decrease of the apparent band gap down to ≈ 1 eV. Towards the right (at the spatial position > 1800 nm), the apparent band gap widens again due to the subsequent n -doped layer on top.

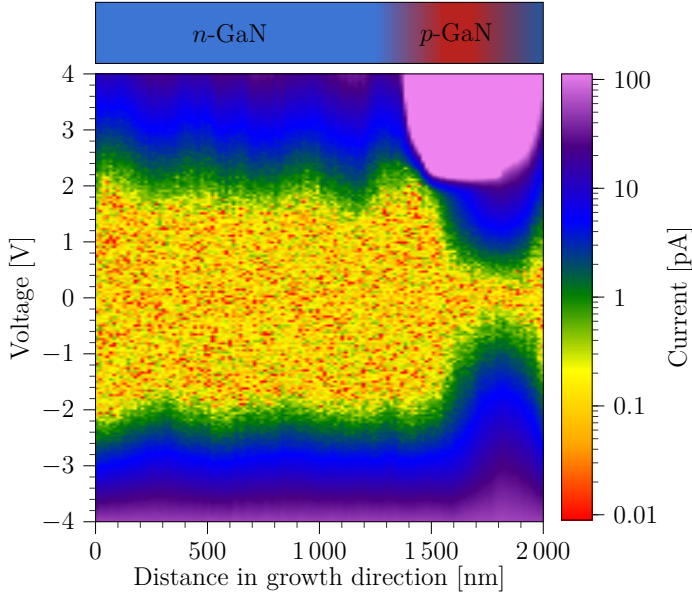


Figure 5.6: Evolution of tunnel spectra (setpoint -4 V and 50 pA) perpendicular to the n - p - n GaN junctions (i.e., in growth direction). The image was generated from a grid of tunnel spectra, measured at the clean UHV-cleaved non-polar GaN ($10\bar{1}0$) surface. Then the grid was divided into 23 nm wide subregions. The median of all spectra of every subregion is shown as a function of voltage and spatial position, using logarithmic color-coding. The onset of the positive and negative tunnel current branches is revealed by the yellow to green transition.

The electronic contrast between the n - and p -doped GaN ($10\bar{1}0$) surfaces can be further assessed by analyzing the spatial evolution of the asymmetry of the tunneling spectra (cf. Fig. 5.7a). The asymmetry of the tunnel spectra is defined here as the mean tunnel current in the voltage range from -2.3 V to 2.3 V . According to this definition, an asymmetry value around 0 is indicative for a tunneling spectrum with similar absolute onset voltages and slopes for the negative and positive current branches. In contrast, values above 0 are characteristic of a smaller onset voltage and an enhanced tunnel current of the positive current branch. Spectra obtained at the surface of the n -doped GaN layer (cf. blue $I(V)$ curves in Fig. 5.7a) are almost symmetrical in terms of current onset voltages and slopes of the negative and positive current branches. Thus, they exhibit asymmetry values close to zero (cf. blue

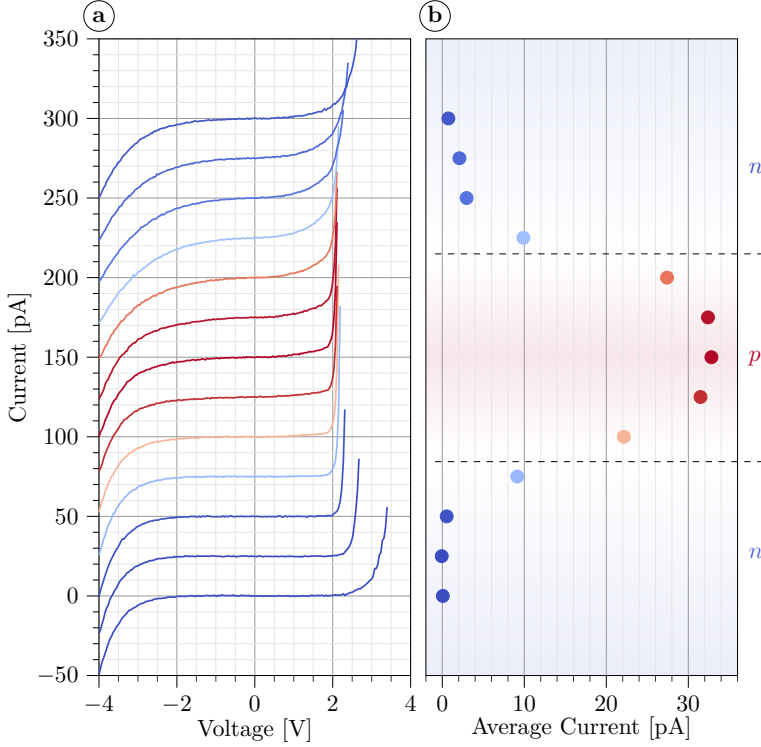


Figure 5.7: (a) Spatial evolution of current-voltage spectra across the n - p - n -layers (set-point -4 V and 50 pA) acquired on freshly cleaved, clean GaN surfaces in UHV. Every spectrum displayed is the median of 490 single tunneling spectra measured in a rectangular spatial area two pixels wide in the c direction (corresponding roughly to 23 nm). The equidistant spatial separation between consecutive rectangular surface areas is approximately 70 nm in the c direction (i.e., the spatial separation between consecutively shown median spectra). For better visibility, consecutive spectra are offset by 25 pA. The current is cut off at approximately 50 pA for display purposes only. (b) Averaged current in the voltage range from -2.3 V to $+2.3$ V for the spectra shown in (a). Blue spectra are rather symmetric within the n -type material. Red spectra show an asymmetric behavior, i.e., the average current is much larger than zero (red circles). This points to p -type material characteristics. Reproduced from [P2], with the permission of AIP Publishing.

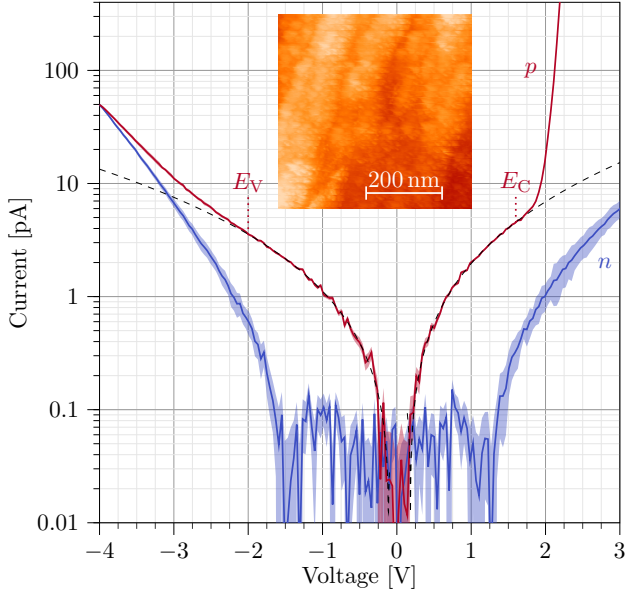


Figure 5.8: Current-voltage ($I(V)$) spectra obtained at the centers of the p - and n -doped layers exposed on freshly cleaved, clean GaN surfaces in UHV. The n - (blue line) and p -type (red line) spectra are the medians of 10230 and 7225 single spectra, respectively. The background shadow indicates the respective error range of one standard deviation. The data is extracted from the same measurement as that in Fig. 5.7. The tip-sample separation was fixed at -4 V and 50 pA. The dashed curve is a fit to the first current onsets of the spectrum measured on the p -doped layer. The constant-current STM image (setpoint $+6$ V and 80 pA) of the p -doped layer in the inset demonstrates the high step density inducing a Fermi-level pinning. Reproduced from [P2], with the permission of AIP Publishing.

circle in Fig. 5.7b). In contrast, the spectra recorded on the p -doped layer show significantly different behavior with higher absolute currents at the positive voltage branch compared to the spectra of n -type GaN. This leads to positive asymmetry values in the range of 20 to 30 pA (cf. red circle in Fig. 5.7b). The asymmetry of the tunneling spectra is used in the following, in addition, to identify the p - and n -doped layers at the GaN ($10\bar{1}0$) cleavage surface.

Next, an in-depth analysis of the tunnel spectra recorded on the differently doped GaN layers is provided. Figure. 5.8 illustrates the median of the tunnel spectra

obtained at both n - and p -doped GaN layers in a logarithmic scale. The blue line comprises spectra acquired in the center of the first n -doped layer. Its shape is quite similar to previously measured n -type spectra on clean *in-situ* cleaved m -plane GaN [34, 38]. The key features of these spectra are first, an apparent band gap smaller than the fundamental band gap, and second, an upward shift of the conduction band current onset to about +1 V, i.e., much higher as compared to that expected for unpinned n -type semiconductors (≈ 0 V) [P2]. The shift of the current onset has been attributed to the presence of the empty Ga-derived dangling bond surface state below the conduction band minimum (i.e., within the fundamental band gap), which leads to a surface Fermi-level pinning [33, 34, 36–38]. At negative voltages, however, no surface Fermi-level pinning and thus no upward band bending was observed. In contrast, at small negative voltages, the recorded current originates from electrons tunneling from a tip-induced electron accumulation zone into empty tip states (i.e., the conduction band minimum is dragged below the Fermi level locally). Only at larger negative voltages, the tunneling out of filled valence band states into empty tip states occurs in addition to the tunneling out from the accumulation zone. The convolution of both tunnel current contributions is measured by STS. Thus, for the specific case of nitride semiconductors, the measurement of the size of the fundamental band gap by STS is complicated by i) the convolution of different tunnel current components at negative voltages and ii) the presence of a surface Fermi-level pinning at positive voltages only [106].

The $I(V)$ spectra measured at the center of the p -type GaN layer do exhibit fundamentally different characteristics. First, the apparent band gap is much smaller than on n -type material. Second, at positive voltages, a second current onset is observed at about +1.6 V. For the negative branch, a similar but weaker secondary onset occurs at voltages of about -2 V. The secondary onsets can be identified by a reversal of curvature. The presence of two current contributions in each current branch can be further revealed by fitting the tunnel current close to the first current onsets. In first approximation, a simple exponential dependence of the tunnel current on the voltage is used to fit the $I(V)$ characteristic close to the onset (cf. Eq. 5.1). This dependency is based on Eq. 24 in Ref. [67], which takes into account the exponential transmission coefficient. In addition, this equation was extended by the shift induced by the current onset voltage, which leads to the

equation:

$$I \propto \exp(\alpha \cdot |V - V_{\text{onset}}|^{0.5}). \quad (5.1)$$

In Eq. 5.1 α is a constant, and V_{onset} is the shift of the surface band edges relative to the Fermi level E_F [22, 67]. As it turned out, an exponent of about 0.25 instead of 0.5 yields the best fits. The fitted currents are depicted in Fig. 5.8 as gray dashed lines. Subtracting the fitted tunnel currents from the measured $I(V)$ profile yields an estimation of the second current onsets, which are assigned to the bulk valence (E_V) and conduction band edge (E_C) in Fig. 5.8.

The very small apparent band gap of the spectra on the p -type layer suggests the presence of surface states pinning the Fermi energy near the mid-gap position. This and the symmetric shape of the spectra close to 0 V indicates that electrons can tunnel into and out of these surface states, pointing to half-filled surface states. The steeper slope of the current at the second current onset is higher than the current out of the first onset, suggests a significantly smaller DOS of the midgap states as compared to the DOS present at the second current onset at higher voltages. The smaller DOS can be attributed to the defect states at the surface, while the second onsets, which are indicative of a higher DOS, arise from electrons tunneling into or out of the bulk conduction and valence bands states, respectively. Indeed, the separation of second onset voltages of 3.6 V fits well to the fundamental band gap of GaN at room temperature of approximately 3.4 eV. Hence the defects pin the p -type GaN surface 1.6 eV below the conduction band edge.

5.1.4 Discussion of the origin of Fermi-level pinning

Next, the physical origin of the surface states and thus of the surface Fermi-level pinning will be elucidated. The intrinsic surface states of the GaN (10 $\bar{1}$ 0) surfaces comprise empty Ga-derived or the filled N-derived dangling bond states. While the filled states turned out to be resonant with the bulk valence band or close to the valence band [33–37, 110], a significant DOS arising from the empty Ga dangling bonds was found within the fundamental band gap of GaN, reaching up to 0.7 eV below the conduction band edge [33–39]. For p -type GaN, the bulk Fermi level

close to the valence band edge is too low to achieve an occupation of this empty acceptor-like surface state. Thus, it becomes electrically inactive and cannot be responsible for the observed midgap pinning.

Similarly, the filled N-derived dangling bond surface states cannot induce a midgap pinning either, since they are close to the valence band edge and thus lack a DOS within the fundamental band gap [34, 124–127]. In addition, the concentration of activated Mg dopants in *p*-type GaN is always rather small, typically giving rise to a Fermi level located relatively far above the valence band edge. Thus, the fully occupied N-derived intrinsic surface state cannot give rise to a surface Fermi-level pinning. Finally, intrinsic surface states have a DOS of states comparable to the bulk bands and thus much larger than that of extrinsic surface states such as defect states. Therefore, the current induced by intrinsic surface states is larger than that of extrinsic surface states. On *p*-type GaN (10 $\bar{1}$ 0) surfaces, the current due to surface states is significantly smaller than that of the bulk states, suggesting extrinsic defect states as the origin.

At this stage, the origin of the extrinsic surface state is further addressed. The surface morphology revealed by STM and SEM exhibits a high density of cleavage steps. The 3D-growth structure of the capping layer might be at the origin of the large step density since the cleavage may start simultaneously at multiple positions in the 3D-grown cap. As a result, steps and step kinks are present at the cleavage surface. They exhibit localized states, which are typically half-filled and in midgap position [39, 40, 128–132]. Therefore, the surface pinning is anticipated to be caused by these defect states.

In contrast, the situation is different for *n*-type GaN (10 $\bar{1}$ 0) surfaces. With the Fermi level located close to the conduction band edge, the intrinsic Ga-derived dangling bond surface state is partially occupied. Since the LDOS of the dangling bond states is much higher than the LDOS of the defect state, the surface Fermi level will be pinned by this intrinsic surface state.

Finally, the fictive case of an unpinned *p*-type GaN (10 $\bar{1}$ 0) surface is addressed. Even in this configuration, the spectra would also be fundamentally different from those measured on *n*-doped GaN (10 $\bar{1}$ 0) surfaces [P2]: "No electrons would be in the conduction band under (non-equilibrium) tunneling conditions, even if the

conduction band edge is dragged below the Fermi energy by the tip's electric field [for unpinned p -type GaN (10 $\bar{1}$ 0) surfaces]. Hence, no tunneling current of electrons from the conduction band into the tip can occur at negative voltages [133]. Thus, on p -type surfaces, no electron accumulation current occurs at negative voltages. The analogous hole accumulation current of electrons tunneling from the tip into the hole accumulation zone in the valence band at positive voltages can be neglected: the barrier for tunneling directly into the conduction band is much smaller (due to the large band gap) and hence the normal conduction band current dominates. Hence, even for unpinned p -type material, the fundamental band gap is detectable in contrast to n -type material [106]" [P2].

5.1.5 Tunneling spectroscopy on surfaces after exposure to ambient conditions

After the STM measurements were performed on the freshly cleaved sample surface, the sample was transferred through the air for further analysis by SEM (cf. Fig. 5.5). After SEM imaging, the sample was reinserted into the vacuum chamber of the STM. For this purpose, the sample was first placed in the load lock chamber, and heated for 4 days at 110 °C.

After air exposure and subsequent restoration of UHV conditions, both the tunnel spectra (cf. Figs. 5.9, 5.10) and CITS maps (cf. Fig. 5.5) still exhibit characteristics that enable a distinction between the different layers of the n - p - n GaN structure: In the evolution of the tunnel spectra in growth direction, as shown in Fig. 5.9, all three layers are clearly distinguishable, with the p -type layer in the center of Fig. 5.9 being most prominent due to its smaller apparent band gap and its higher current of the positive voltage branch, compared to the n -type GaN layers on the left and right. This leads in turn to an increased asymmetry of the tunnel spectra in the p -type region, as depicted in Fig. 5.10. To illustrate this asymmetric behavior, the tunnel current of the spectra was again averaged in the range from -2.1 V to +2.1 V. The asymmetry of the tunnel spectra is found to be slightly negative (i.e., higher currents at the negative branch) for n -type GaN and pronounced positive (i.e., higher currents at the positive branch) for the p -type layer. The reversal of the

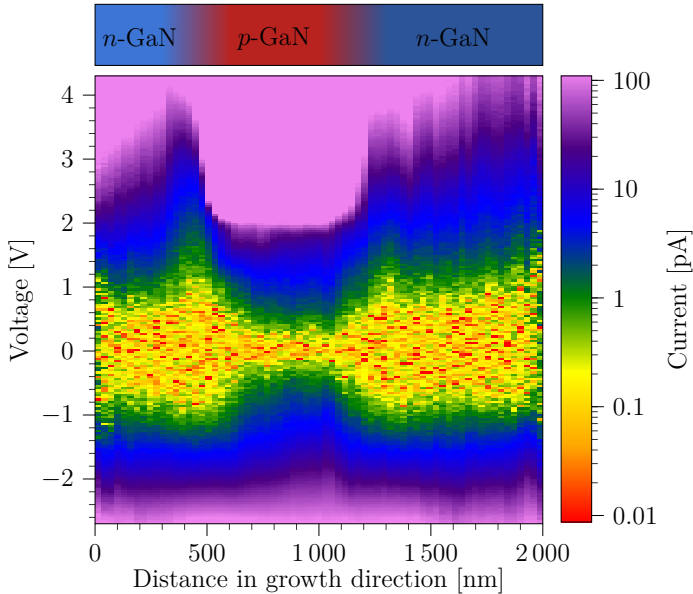


Figure 5.9: Evolution of tunnel spectra in growth direction after air exposure acquired at a negative setpoint of -2.5 V and 80 pA. The current onset is discernible again at the yellow to green transition as in Fig. 5.6. The n -doped GaN regions are on the left and right, as indicated by the colored bar on top. The p -doped region becomes visible in the center (starting at a spatial position of 500 nm to 1100 nm) and is characterized by a very small apparent band gap.

asymmetry between n - and p -doped areas is in agreement with tunneling spectra obtained on GaAs(110) n - and p -junctions [93, 133, 134].

The tunnel spectra evolution across the n - p - n junction changes significantly when reversing the polarity of the set voltage. Figure 5.11 depicts the tunnel current evolution across the n - p - n junction, similar to the one shown in Fig. 5.9, but this time recorded using a positive setpoint of $+6$ V and 80 pA. The tunnel spectra measured at the p -doped layer exhibit a much larger apparent band gap than those obtained on the n -doped layers. This at first glance counterintuitive result can be explained by the rather high positive set voltage used for the acquisition: The spectra measured at the p -type layer exhibit at positive voltages, independent of the air exposure, a second current onset at $+2$ V, and a strong current increase at higher

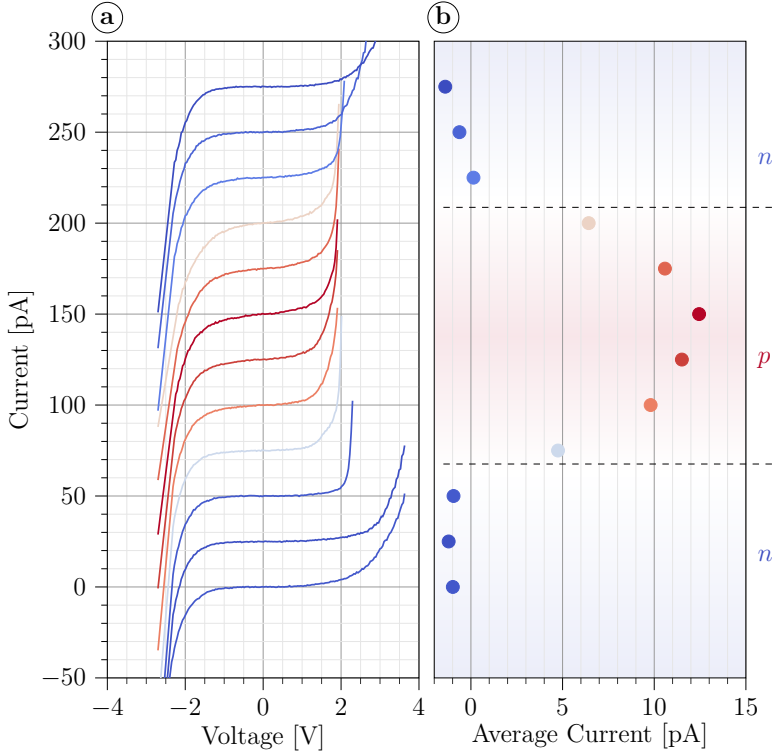


Figure 5.10: a) Spatial evolution of tunneling spectra (setpoint -2.5 V and 80 pA) across the n - p - n -layers after air-exposure, evaluated in analogy to Fig. 5.7. Each spectrum is the median of at least 460 single spectra. The spatial distance between two consecutive spectra is roughly 90 nm. b) Averaged current (from -2.1 V to $+2.1$ V) of the spectra shown in a). Spectra (red) at the p -doped layer show a positive asymmetric behavior, whereas spectra (blue) at the n -doped layer have a small negative asymmetry. Reproduced from [P2], with the permission of AIP Publishing.

voltages (cf. Figs. 5.8, 5.12 and 5.13). Thus, for a set voltage of $+6$ V, the tip-sample separation will be increased substantially (as compared to negative set voltages) by the feedback electronics in order to counteract the strong current increase on p -type GaN and keep the set current at 80 pA. However, this increase of the tip-sample separation is accompanied by a reduced tunnel current at the negative current branch too. As a result, the negative current branch of the spectrum is below the detection limit in a rather wide voltage range. In contrast, for n -type

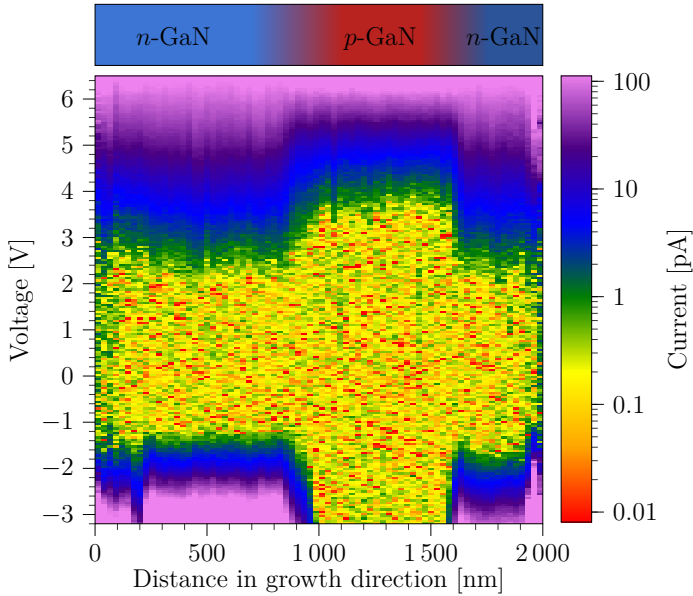


Figure 5.11: Tunnel spectra evolution across the n - p - n junction after air exposure. The spectra were measured using a positive setpoint of +6 V and 80 pA. The p -doped region becomes visible in the center (starting at a spatial position of 900 nm to 1600 nm) and is characterized by a very large apparent band gap. The n -doped GaN region is on the left and right. The changes in apparent band gap are due to substantially different tip-sample separations between n - and p -type GaN. A proper comparison is not possible at positive set voltages.

GaN, the spectra do not exhibit a large current at large positive voltages as on p -type material. Hence, on n -type GaN, the tip-sample separation is not increased at positive set voltages. Hence, the tip-sample separation is at positive set voltages strongly differing between n - and p -type GaN, and thus the spectra cannot be compared. A comparison is only possible at negative set voltages in the range below -2 V, where the tip-sample separation on p and n -type GaN is almost identical, as done in the following.

Let us now return to the detailed analysis of the spectra measured at the center of both the p -doped (cf. Fig. 5.12) and n -doped (cf. Fig. 5.13) layer, with negative set voltage. At first glance, the spectra after air exposure and subsequent reintroduction into UHV with long-term annealing are quite similar to the spectra recorded

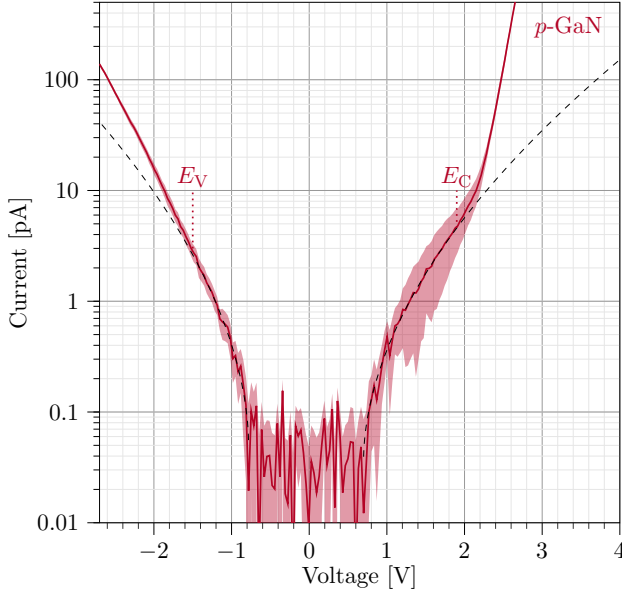


Figure 5.12: Characteristic $I(V)$ spectra obtained at the p -doped layer after air exposure. The setpoint is at -2.5 V and 80 pA. The dashed curves are fits to the first current onsets of the spectrum. The background shadow indicates the error margin. Reproduced from [P2], with the permission of AIP Publishing.

on the freshly cleaved clean sample: At the p -doped layer, two onsets are clearly distinguishable, one at $+0.8$ V, the second one around $+2$ V (cf. Fig. 5.12). Of the onsets at negative voltages (-0.8 V and -1.5 V), the second one is less pronounced than in the spectrum on the clean sample (cf. Fig. 5.8) but clearly present. The first onsets of the p -type spectra after air exposure were again fitted using the same method as mentioned before in Sec. 5.1.3 (cf. Eq. 5.1). The best fits were achieved for an exponent of about 0.5 and are shown as dashed lines in Fig. 5.12. The voltage difference of the second onsets at negative and positive voltages is about 3.5 V and thus close to the fundamental band gap of 3.4 eV.

Despite many similarities of the spectra on p -type material before and after air exposure, some key differences occur: The apparent band gap is slightly larger after air exposure, and the pinning position is shifted a few tenths of eV towards the valence band edge compared to the spectra on the freshly cleaved clean surface.

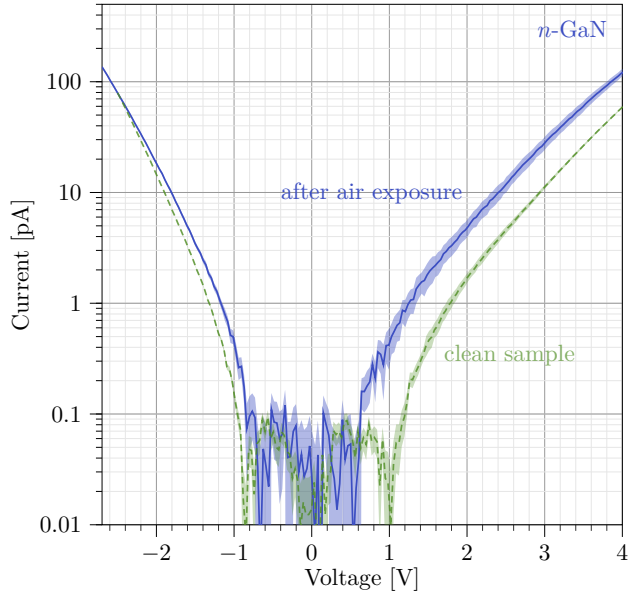


Figure 5.13: Characteristic $I(V)$ spectra obtained at the n -doped layer after air exposure. The setpoint is at -2.5 V and 80 pA. For comparison, a spectrum at the same setpoint from the n -type substrate of the clean sample is also displayed. The background shadows indicate the error margin. Reproduced from [P2], with the permission of AIP Publishing.

The spectra recorded on n -type material after air exposure are quite similar too to the spectra measured with the same setpoint on the freshly cleaved clean n -type GaN surface (cf. Fig. 5.13). The only difference is a downward shift of the onset voltage of the positive current branch to 0.5 V (i.e., onset shifted towards 0).

5.2 Discussion of the effect of air exposure

In this section, the origin of the electronic changes due to air exposure is elucidated. First, the experimental observations described above on p -type material air exposure leads to an increase of the apparent band gap attributable to a decrease of the defect currents. This suggests a reduced pinning DOS which is also accompanied by a slight shift of the pinning level.

On *n*-type material, the pinning level shifts toward the conduction band upon air exposure. This suggests again a reduced pinning DOS.

Both of these effects are anticipated to be caused by air exposure. The most likely adsorbed air components on the non-polar GaN surface are either oxygen or water molecules since other gases, such as nitrogen, are non-reactive or have a negligible concentration. Typically, oxidation is the dominating effect at many unprotected semiconductors surfaces subjected to ambient air at room temperature, such as GaAs and Si. The resulting oxide can penetrate deep into the bulk material. However, it is known that GaN exhibits different behavior in which no oxidation is detected below 700 °C [135, 136]. Furthermore, the sticking coefficient of oxygen on GaN (10 $\bar{1}0$) surfaces is significantly lower than that of water [88]. Recent publications suggest that adsorption and subsequent dissociation of water molecules is the preferred reaction process on polar GaN surfaces [89, 90].

This adsorption and dissociation process also occurs on the non-polar GaN (10 $\bar{1}0$) surface: Theoretical calculations and experiments found a small dissociation barrier for H₂O in the low meV range [137–139]. Such a low dissociation barrier implies a fast, almost instant coverage of the surface by dissociated water, much faster than oxidation can take place. At the hydroxylated surface, the OH⁻ group is bound to the Ga surface atom, while the H⁺ is associated with the N [90, 137, 138, 140]. Of the various possible hydroxylation configurations, this one has the highest dissociation energy of 1.44 eV and is [90, 137, 138, 140], therefore, the most stable one. The Ga-OH bond can only be broken above 200 °C [88, 139]. Therefore, the annealing of the here investigated air-exposed samples during baking in the load-lock chamber at 110 °C was not sufficient to remove the dissociated water molecules.

The hydroxylated surface has a large impact on the electronic properties since both the N- and Ga-derived dangling bond surface states are shifted to the valence band edge emptying the fundamental band gap of intrinsic surface states [138, 141]. The shift of the intrinsic surface states relative to the band edges is illustrated in Fig. 5.14 for the clean (left) and hydroxylated (right) surface: after air exposure, the N-H bond surface state is energetically positioned below the valence band edge [141]. The Ga-OH bond surface state is found close to the valence band edge [138, 140].

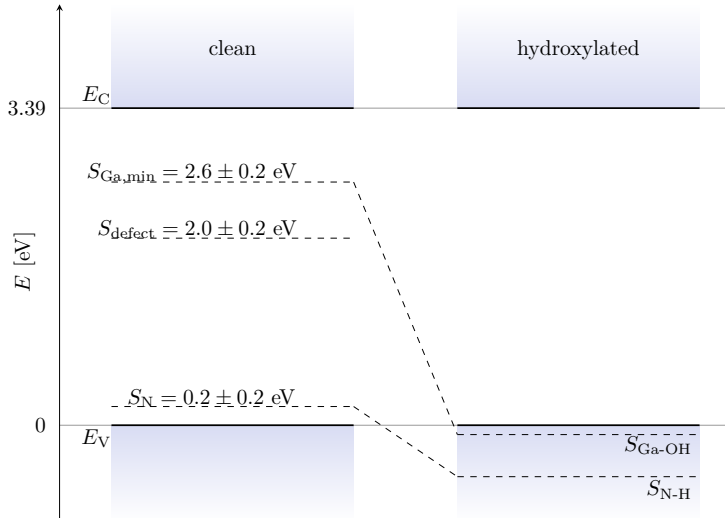


Figure 5.14: Schematic diagram showing the energy levels of the different states (intrinsic surface states, defect states and hydroxylated intrinsic surface states) for the clean and hydroxylated m -plane GaN surface. The energy levels were extracted from our measurements (S_{defect} and S_{Ga}) and Refs. [138, 141]. Reproduced from [P2], with the permission of AIP Publishing.

A H_2O -driven passivation of the non-polar GaN surface is in good agreement with the STS measurements in this thesis, as discussed in detail below.

p -type GaN

As mentioned above, a high density of steps is present at the cleaved m -plane surface. The resulting step edges and kinks correspond to either a - or c -plane facets, with the latter appearing more frequently in the sample studied. The defect states arising from these step edges and kinks give rise to Fermi-level pinning on the freshly cleaved clean p -type GaN ($10\bar{1}0$) surface as measured by STS (see, e.g., Fig. 5.8).

Hydroxylation is also expected to affect step edges and kinks. The a -plane facets at the step edges can be anticipated to behave as m -plane surfaces. Thus, hydroxylation or hydrogen absorption at these edges shifts the intrinsic surface state into the

valence band. Indeed, similar behavior has already been observed for the intrinsic surface states of GaN c -plane surfaces, caused either by hydroxylation [89,142,143] or hydrogen absorption [144]. Therefore, one can expect that step edges can be passivated by hydroxylation. This is in line with the experimental observations on p -type GaN ($10\bar{1}0$) surfaces, which imply a smaller density of defect states and a shift of the pinning levels. The fact that the pinning level was only shifted but was not completely removed from the fundamental band gap indicates that the step edges are only partially hydrated, in agreement with the above expectation [P2]. Exposing the non-polar p -type GaN surface to water instead of air could ultimately lead to a full passivation.

n -type GaN

As discussed in Sec. 5.1.5, the minimum of the Ga-derived empty dangling bond leads to Fermi-level pinning of n -type GaN ($10\bar{1}0$) surfaces. On clean samples, this surface Fermi-level pinning induces an upward band bending of about 1 eV. After air exposure of the surface, the upward band bending is reduced to about 0.5 eV. This reduction is in agreement with electroreflectance measurements. These showed a Fermi-level pinning 0.42 ± 0.05 eV below the conduction band [145].

The explanation for the reduced band bending is the passivation of the Ga-derived empty dangling bond by hydroxide groups. The resulting filled Ga-OH state is shifted towards the valence band edge [138, 140]. Provided that hydroxylation passivates most, but not all Ga dangling bonds, a reduced density of pinning states will be present after air exposure, which in turn would lower the band bending towards flat band conditions. This is consistent with the reduced band bending observed by the measurements.

Note that with this type of analysis, no differences of OH⁻ bond to the Ga surface atoms can be identified for the n - or p -doped surface. Therefore, there is no evidence for a Fermi-level dependent behavior of the surface reaction.

Finally, the hydroxylation and adsorption on GaN surfaces other than the ($10\bar{1}0$) surface and the adsorption of other molecules on the m -plane surface are discussed. On the one hand, hydroxylation has been investigated on c -plane GaN surfaces,

too: On the c -plane surface, the adsorption of hydroxyl groups is preferred near the H3 site but not at the Ga location (T4 site) [146]. Hence the binding structure is not comparable with that on the m -plane surface. Interestingly, at high hydroxyl concentrations, the pinning of the Ga surface state at the c -plane surface is lifted [147]. This tendency agrees with that observed here on the m -plane GaN surface.

On the other hand, the binding of other types of molecules was investigated on m -plane GaN surfaces. It is found that the sulfur atom of thiol groups is bound to the Ga dangling bond [148], in analogy to the adsorption of the OH^- group. This suggests that the complex negatively charged molecule groups generally bind to the empty Ga dangling bond. This site is likely preferred due to the cation character of Ga in GaN.

For the sake of completeness, the conclusions drawn and the methodology used should be examined critically at this point. Besides the interpretation shown here, other effects can also lead to similar tunnel spectra, such as pure hydrogen passivation or oxygen coverage [36, 141]. However, considering the literature results regarding adsorption for different molecules on GaN surfaces [141], the most plausible interpretation is the one outlined above. In addition, the energy levels of the surface states expected from literature for the presented interpretation regarding hydroxylation are consistent with the observed pinning and density changes [36, 140]. Finally, it should be mentioned that the determination of the defect pinning level is blurred due to the thermal broadening and the measurement noise. Nevertheless, the defect pinning level is still well below the minimum of the Ga-derived dangling bond state and can therefore be well separated.

5.3 Conclusion

In this chapter, a cross-sectional scanning tunneling microscopy and spectroscopy investigation of GaN n - p - n -junctions is presented. The focus is on the comparison of freshly cleaved clean cross-section surfaces in UHV with surfaces after exposure to air [P2]. For the freshly cleaved clean n -type GaN ($10\bar{1}0$) surface, the Fermi level is found to be intrinsically pinned by the empty Ga-derived dangling bond surface state. In contrast, on the p -type GaN ($10\bar{1}0$) surfaces, pinning by extrinsic defect

states dominates. After exposure to ambient air and reintroduction and heating in UHV, the pinning shifts towards the band edges combined with a reduced density of the pinning states. These effects are discussed in the framework of adsorption and dissociation of water molecules. The hydroxylation results in a passivation of both intrinsic and extrinsic surface states by shifting the surface state into the valence band. These results reveal an interesting interplay between intrinsic and extrinsic surface states present at the m -plane surface of GaN [P2]. The results illustrate how critical the dopant-dependent Fermi-level pinning is for the interpretation of tunnel spectra in doping structures in group III-nitrides.

Furthermore, the study suggests a pathway towards creating passivated GaN surfaces with flat band conditions. Such passivated nitride surfaces are useful for the production of improved nanowire-based optoelectronic devices, solar cells, hydrogen splitting cells, or bio-electric devices, as well as laser facets [P2].

Chapter 6

Intrinsic surface states of ternary (Al,Ga)N ($10\bar{1}0$) surfaces

6.1 Experiment

For the XSTM investigations, small rectangular samples were cut from the as-grown wafer, thinned, and electrically contacted [96]. For further details on the sample structure and preparation, the reader is referred to Sec. 3.4.2. After transfer into the ultra-high vacuum chamber ($p < 2 \cdot 10^{-8}$ Pa) of the STM, the samples were cleaved to obtain contamination-free cross-sectional ($10\bar{1}0$) surfaces. The measurements were performed without interruption of the vacuum. Compositions and layer thicknesses were studied by energy dispersive x-ray (EDX) spectroscopy in a FEI Titan G2 80-200 CREWLEY scanning transmission electron microscope (STEM) [96, 149].

6.2 Experimental results

Figure 6.1 provides a chemical, microscopic, and electronic overview of the cross-sectional $\text{Al}_{0.17}\text{Ga}_{0.83}\text{N}/\text{Al}_{0.35}\text{Ga}_{0.65}\text{N}/\text{AlN}/\text{Si}$ hetero sample structure. The constant-current XSTM image in Fig. 6.1b acquired at -2.5 V primarily reveals the topography of the non-polar ($10\bar{1}0$) cleavage surface. It consists of large atomically flat

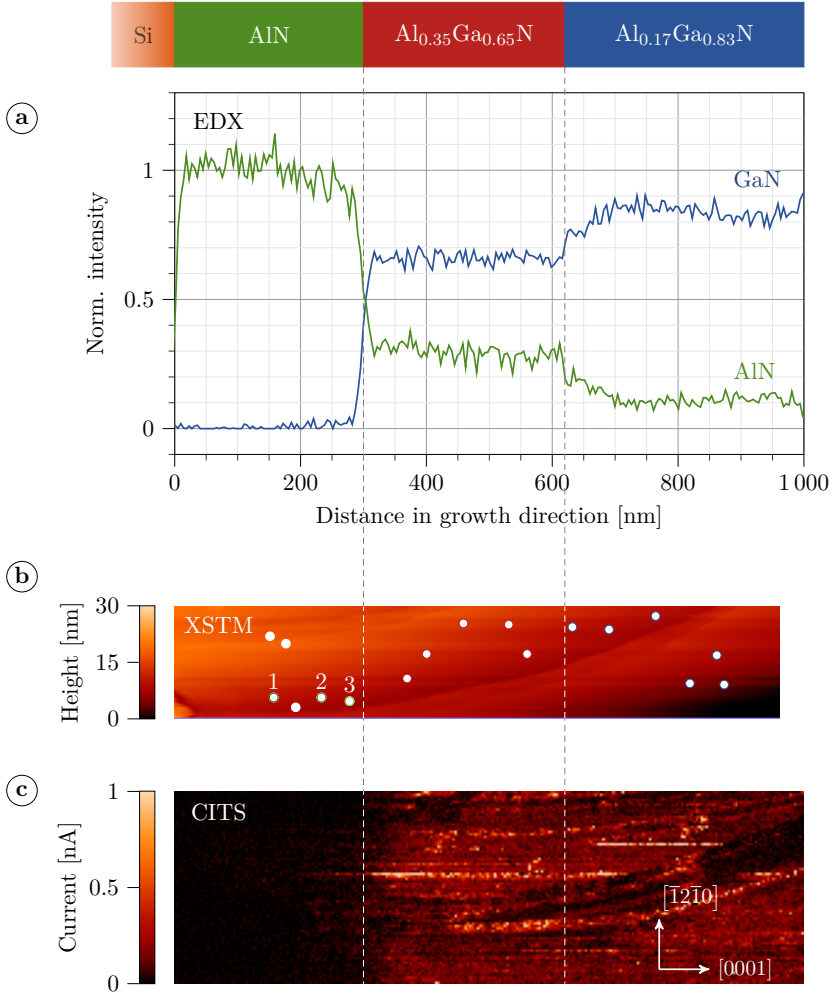


Figure 6.1: (a) EDX measurement of the Al and Ga compositions for the three different layers. (b) XSTM image, measured at a setpoint of -2.5 V, 80 pA. (c) CITS image of the same area, measured at a setpoint of -4.5 V, 80 pA. The CITS map depicts the measured current at a selected voltage of $+4.8$ V. While the XSTM image in (b) does not reveal topographic changes at the layers' interfaces, the CITS image in (c) exhibits a pronounced change of contrast and thus of the electronic properties at the Al_{0.35}Ga_{0.65}N/AlN interface. In addition to the CITS maps, single-point spectroscopy has been performed at spatial positions that are indicated by filled circles in the XSTM image.

terraces separated by cleavage steps of various heights. Despite the rather large compositional differences at the heterointerfaces, as revealed by the EDX line profile in Fig. 6.1a, no surface topography changes can be discerned. In particular, the cleavage steps cross the interfaces unaffected and without any directional change. At negative set voltages, there is also no detectable electronic contrast change at the two heterointerfaces covered by the overview images (cf. Chapter 4; the accumulation current is nearly independent of most semiconductor parameters). Only in the far left bottom corner of the constant-current STM image the outermost edge of the Si substrate, which is not of interest here, induces a cleavage orientation and a large height change.

In contrast to the XSTM image at a negative voltage, the CITS map evaluated at positive sample voltages (cf. Fig. 6.1c) reveals a notable change of contrast (i.e., current) at the $\text{Al}_{0.35}\text{Ga}_{0.65}\text{N}/\text{AlN}$ interface (cf. left dashed white line). However, the $\text{Al}_{0.17}\text{Ga}_{0.83}\text{N}/\text{Al}_{0.35}\text{Ga}_{0.65}\text{N}$ interface with smaller composition change exhibits no pronounced contrast either. Therefore, the position of the latter interface in both the XSTM image and the CITS map is determined using the $\text{Al}_{0.35}\text{Ga}_{0.65}\text{N}$ layer thickness as obtained by EDX (cf. right dashed lines). Note, the curved stripe contrast within the (Al,Ga)N layers, in Fig. 6.1c are step-related features, whereas the horizontal single pixel wide lines arise from tip-instabilities.

At this stage, the current-voltage spectra acquired at different spatial positions on the cross-sectional cleavage surface are addressed. At each position, marked by filled circles in Fig. 6.1b, a set of 25 tunnel spectra was measured. All tunnel spectra acquired at spatial positions within the $\text{Al}_{0.17}\text{Ga}_{0.83}\text{N}$ and $\text{Al}_{0.35}\text{Ga}_{0.65}\text{N}$ layers far enough from the interfaces are averaged and shown in Fig. 6.2a and b, as blue and red symbols, respectively. Throughout the AlN layer, a rather large systematic change of the spectra occurs, and thus three spectra acquired with increasing distances to the $\text{Al}_{0.35}\text{Ga}_{0.65}\text{N}/\text{AlN}$ interface are shown in Fig. 6.2c. Their spatial positions are numbered correspondingly in Fig. 6.1b.

The negative current branches of all spectra exhibit identical onset voltages and slopes. In contrast, the onsets and slopes of the positive current branch change with Al content. In particular, the onset voltages increase with the Al concentration. Note, for pure AlN, the positive current branch of the spectra, in addition, exhibits

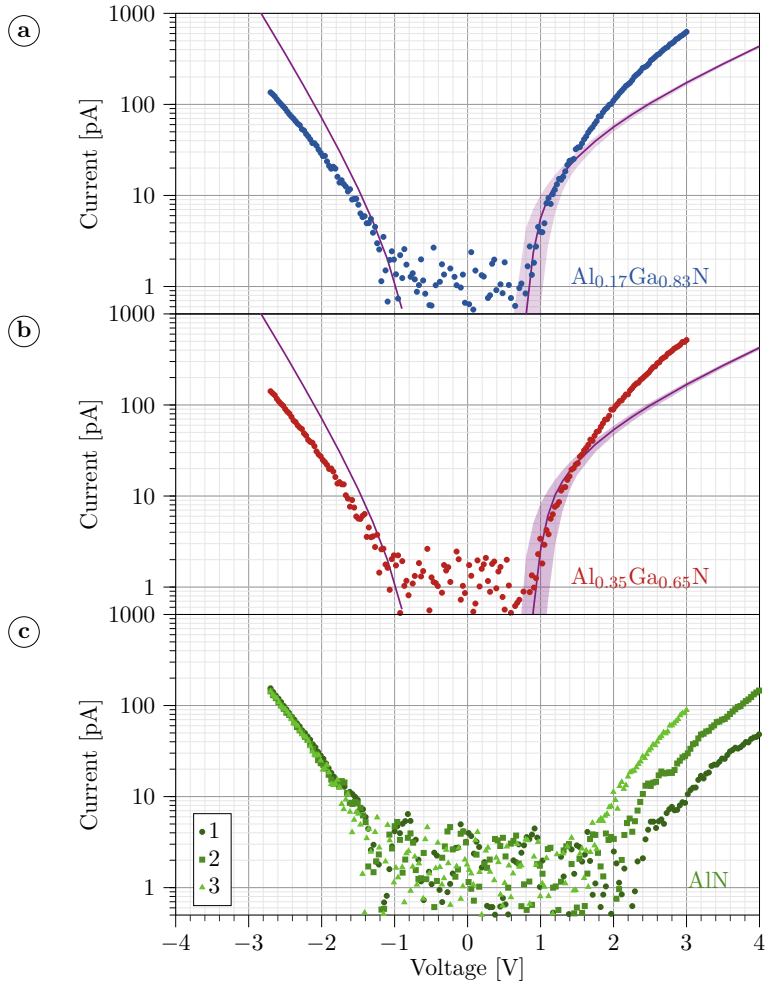


Figure 6.2: $I(V)$ tunnel spectra measured on (a) the $\text{Al}_{0.17}\text{Ga}_{0.83}\text{N}$ -layer (blue symbols), (b) the $\text{Al}_{0.35}\text{Ga}_{0.65}\text{N}$ -layer (red symbols), and (c) the AlN-layer (green symbols). All spectra were obtained using the same setpoint (-2.5 V and 80 pA). The onset of the spectra were fitted by adjusting the surface state energy level in the simulation described in Ref. [79,98,99] (violet lines).

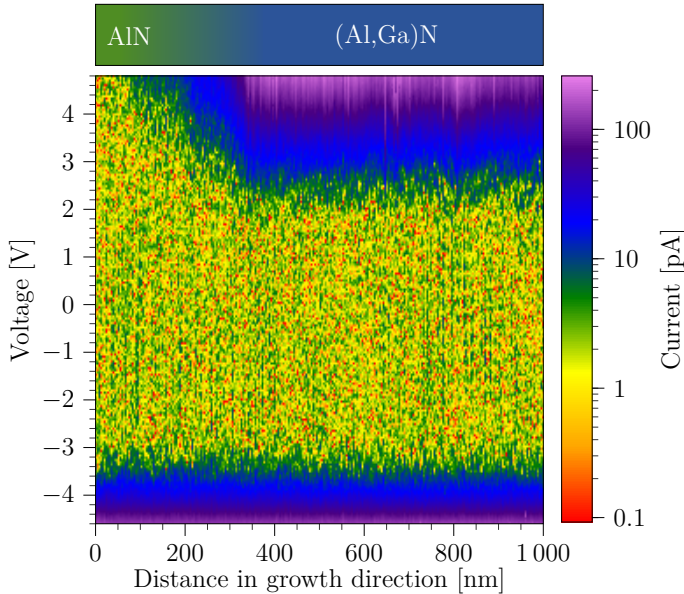


Figure 6.3: Evolution of tunnel spectra in growth direction across the $\text{Al}_x\text{Ga}_{1-x}\text{N}$ -layers. The spectra were measured using a negative setpoint of -4.5 V and 80 pA . A wide transition region between AlN and (Al,Ga)N is visible. In this spectroscopy taken at large tip-sample separation, the two (Al,Ga)N layers with different compositions cannot be distinguished easily.

a shift to larger onset voltages with increasing distance to the $\text{Al}_{0.35}\text{Ga}_{0.65}\text{N}/\text{AlN}$ interface (cf. Fig. 6.2c).

The continuous change of tunnel spectra's positive current branch onset within the AlN-layer can also be recognized in the tunnel current evolution across the interfaces shown in Fig. 6.3 (setpoint -4.5 V and 80 pA). The logarithmic scale of the color scheme used enables a rough assignment of the colors to different characteristics of the tunnel spectra: The voltage range that is primarily colored yellow and red is attributed to the apparent band gap, while the transition from yellow to green gives a rough estimation of the spatial evolution of the current onsets across the interfaces. Blue and purple areas represent higher tunnel currents. For AlN (region from 0 nm to 300 nm), the apparent band gap is larger than that of the $\text{Al}_x\text{Ga}_{1-x}\text{N}$ -layers (region from 300 nm to 1000 nm). In the tunnel current evolution image,

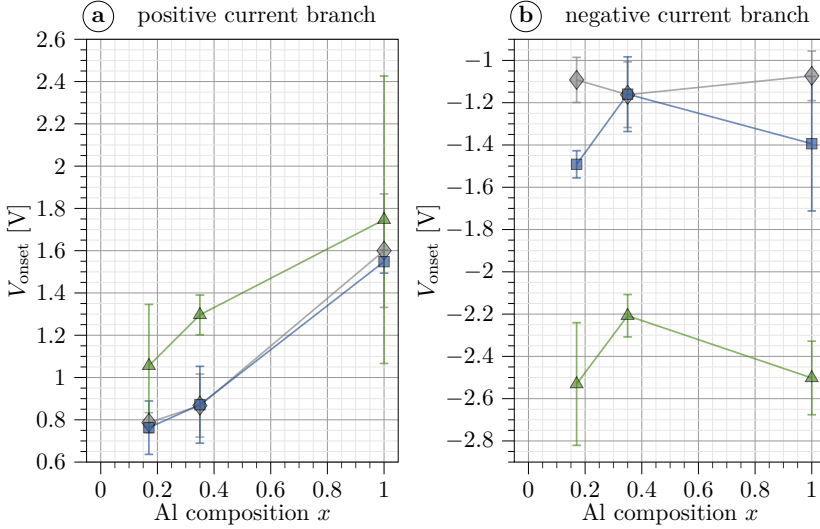


Figure 6.4: Onset voltages of the (a) positive and (b) negative current branches determined from tunnel spectra acquired at different tip-sample separations fixed by different setpoints -80 pA and set voltages of -2.5 V (gray diamonds), -3.5 V (blue rectangles), and -4.5 V (green triangles). The intercept of the noise level with an exponential fit of the positive current branch close to the onset was used to determine the onset voltages.

the AlN tunnel spectra exhibit a continuous change of the onset of the positive current branch away from the AlGaN/AlN interface. At larger distances to this interface (i.e., on the left edge of Fig. 6.3), no current could be measured for positive voltages up to 4.8 V. Therefore, we first consider only spectra measured in the center of the AlN layer, i.e., far away from the AlN/Al_{0.35}Ga_{0.65}N interface (dark green symbols in Fig. 6.2c), whereas for the two other layers, no such spatial dependence is observed.

Figure 6.4 shows the onset voltages V_{onset} of both current branches of the tunnel spectra as a function of the Al content. The tunnel spectra were acquired at three different setpoints with the set current fixed at -80 pA and the voltage set to: -2.5 V (gray diamonds, cf. Fig. 6.2), -3.5 V (blue rectangles), and -4.5 V (green triangles). To determine the voltage onset, the current branch of the $I(V)$ curves were fitted with an exponential function and the intercept with the noise level

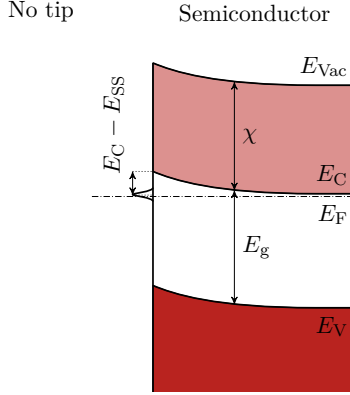


Figure 6.5: Surface state induced band bending without any tip. The cation-derived surface state is partially occupied, pinning the Fermi energy at the surface.

was calculated. The onset voltages of the positive current branch V_{onset} increase with the Al concentration (cf. Fig. 6.4a). The onset voltages V_{onset} of the negative voltage branch seem to be in the same range for all Al concentration and at the same setpoint. (cf. Fig. 6.4b).

6.3 Discussion

In order to understand the Al composition-dependent shift of the current onset at positive voltages (and the lack of Al concentration dependence at negative voltages), we recall that the freshly cleaved (10 $\bar{1}$ 0) surfaces exhibit a filled N-derived dangling bond at or near the valence band edge and empty Ga/Al-derived dangling bonds in the upper part of the fundamental band gap (cf. Fig. 2.8) [33,34,41]. On *n*-type surfaces, a partial occupation of the latter cation-derived empty dangling bond state induces an upward band bending and Fermi-level pinning (cf. Fig. 6.5). The magnitude of the upward band bending depends on the energy difference between the lowermost tail (i.e., the minimum) of the LDOS of the cation-derived surface state and the Fermi level near the conduction band minimum.

During STM measurements, the additional presence of a biased probe tip modifies

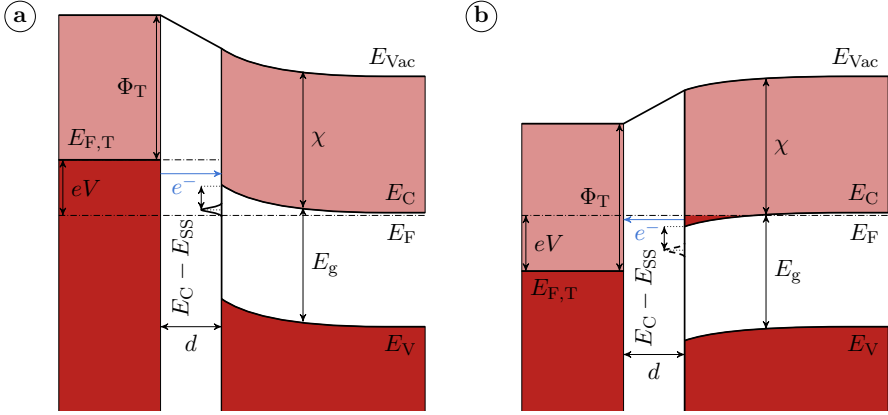


Figure 6.6: (a) Band bending at positive voltages applied between tip and sample. Due to the additional band bending induced by the cation-derived surface state, the applied voltage has to be higher for electrons to tunnel from filled tip states into empty conduction band states. (b) Band bending at negative voltages. The upward band bending of the cation-derived surface state is removed due to the electrons tunneling out of the surface state into the tip.

this intrinsic band bending (cf. Fig. 6.6):

At negative voltages applied to the sample, the tip induces a downward band bending, and the partial occupation of the empty surface state is removed (by tunneling from the surface state into the tip). Thereby the conduction band edge is dragged below the Fermi energy, creating an electron accumulation zone in the conduction band (cf. Fig. 6.6b). Note that the empty surface state cannot be filled despite being below the Fermi level E_F since the transition probability between the conduction band minimum and the surface state is smaller than between the surface state and the tip [38]. Hence, at negative voltages smaller than the band gap, the tunnel current is dominated by electron tunneling out of this accumulation zone in the conduction band into the tip [38]. The resulting current is essentially independent of band alignment, doping level, Al composition, etc., and thus the contrast is dominated by topographic features only. This explains the lack of contrast at the heterointerfaces in the XSTM images acquired at negative voltages and the absence of Al composition dependence of the onset voltage at negative voltages (cf. Fig. 6.4b).

At positive voltages, the additional electric field due to the presence of the tip modifies the intrinsic band bending primarily at large voltages only, where the tip-induced band bending dominates. At small positive voltages, the tip-induced band bending is negligible, and therefore only the intrinsic band bending (cf. Fig. 6.6a) due to the empty surface state in the band gap governs the tunnel current onset (as also described in Chapter 4) [38]. This corresponds to a polarity-dependent Fermi-level pinning for the n -doped m -plane GaN surface, where the onset of the positive voltage branch of the $I(V)$ curves is indicative of the position of the intrinsic surface state in the band gap [38].

6.3.1 Empty surface state of (Al,Ga)N

For the two (Al,Ga)N layers (17% and 35% Al content), the situation should be relatively similar (discussed later in this section in detail) to those of GaN. Therefore, the partially filled surface state will govern the upward band bending in the case of no applied voltage. The voltage required to allow electrons tunneling from filled tip states into empty conduction band states thus depends largely on the energy position of the intrinsic surface state (cf. Fig. 6.6a). Hence, the previously determined onset voltages (cf. Fig. 6.4) indicate in first approximation the position of the surface state below the conduction band edge.

The approximation above assumes that the band bending at the n -type $\text{Al}_x\text{Ga}_{1-x}\text{N}$ ($10\bar{1}0$) surface is independent of the tip, i.e., no tip-induced band bending occurs, and the band bending is determined by the intrinsic Fermi-level pinning only. However, the band bending induced by the tip cannot be neglected entirely as it adds a small additional upward shift of the band edges at positive voltages. In order to decouple these two contributions (i.e., surface state energy and tip-induced band bending) and to eventually obtain a surface Fermi-level pinning energy free of tip-induced effects, we turn to the simulation of the tunnel spectra [76, 79, 98, 100].

We used Vegard's law and literature values for all sample properties. For the effective masses of holes and electrons, the literature values for GaN were used since the Al concentration is relatively small, and the effect even at larger voltages should be negligible. The empty cation-derived surface state was modeled as Gaussian

distribution with a full width at half maximum of 0.1 eV and a total surface charge density of $6 \cdot 10^{14} \text{ cm}^{-2}$, corresponding to one state per surface unit cell. The centroid energy of the Gaussian distribution, relative to the conduction band minimum $E_C - E_{SS}$, was used as a fit parameter. A standard probe tip with a 60 nm radius, an apex opening angle of 45° , and a work function of 4.0 eV was used in all simulations. The work function of the tip (here W) can vary in a wide range due to the tip's surface roughness and orientation [150–153].

According to the SIMS measurement, the (Al,Ga)N layers contained a Si doping concentration of $N_D = 1.6 \cdot 10^{18} \text{ cm}^{-3}$. This Si doping concentration was used for both ternary nitride layers and the assumption of no doping compensation [154–156]. In addition, the activation energy of the dopants was assumed to be identical to that in pure GaN [107–109, 154, 155].

The electron affinities used in the simulation are determined using literature values of the binary compounds GaN and AlN and Vegard's law: For polar GaN surfaces, a wide range of electron affinities from 2.1 eV to 4.1 eV is found in literature [157–162]. Also, for polar AlN surfaces, a similarly wide range of electron affinity values from 0.6 eV to 2.0 eV are reported [159–165]. The electron affinity appears to decrease almost linear with increasing Al content supporting the use of Vegard's law for ternary compounds [159, 160, 166].

For non-polar GaN ($10\bar{1}0$) surfaces an electron affinity of about $\chi = 4.1 \text{ eV}$ is found experimentally [39]. Unfortunately, no experimental values were found in literature for the non-polar surfaces of AlN. In a theoretical calculation of Lymperakis, electron affinities of 3.5 eV and 1.2 eV were found for GaN and AlN ($10\bar{1}0$) surface, respectively [167]. These values appear to be roughly 0.6 eV lower than the experimental one, and it can be anticipated that the electron affinity of non-polar surfaces is at the uppermost end of the range obtained for polar surfaces. Therefore, the electron affinity of the ternary nitride layers is approximated using the upper values of the polar AlN surface (2 eV) and the one of the non-polar GaN surface (4.1 eV). Note that the large uncertainty of the literature values prohibits a clear distinction between the electron affinities of (Al,Ga)N with 17% and 35% Al content. Therefore, an electron affinity of $\chi = 3.5 \text{ eV}$ was assumed, as first approximation, for both ternary nitride layers.

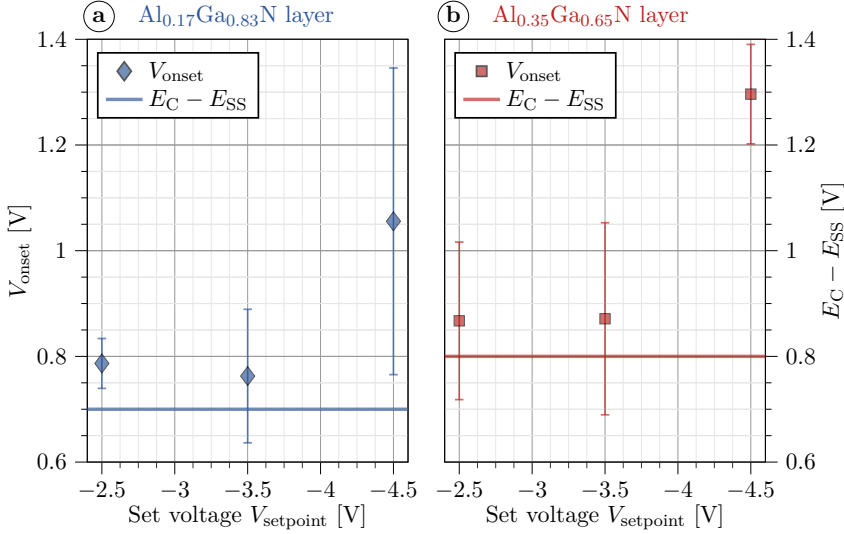


Figure 6.7: Onset voltages ($\cdot e$) for the ternary (Al,Ga)N-layer (cf. Fig. 6.4) with different Al compositions as a function of the tip-sample separation adjusted by the set voltage V_{setpoint} of the setpoint. (a) Voltage onsets obtained on the Al_{0.17}Ga_{0.83}N layer, and (b) on the Al_{0.35}Ga_{0.65}N layer. The set current of the setpoint was 80 pA. The solid lines correspond to the surface state position below the conduction band obtained by tunnel spectra simulation.

The solid violet lines in Fig. 6.2 show the best fits of the simulated tunnel spectra to the measured $I(V)$ curves. In case of the ternary nitride layers, a good agreement could be achieved between the simulation and measured tunnel spectra. The best fits were obtained for surface state energies (below E_C) of (0.7 ± 0.2) eV and (0.8 ± 0.2) eV for Al contents of 17%, and 35%, respectively. The violet shaded areas in Fig. 6.2 indicate changes of the simulated $I(V)$ curves that correspond to the respective uncertainty values.

The centroid energies of the surface state determined in this way can be compared with the previously determined voltage onsets (cf. Fig. 6.4). Since as mentioned above, these values indicate the approximate surface state position below the conduction band. For this purpose, the dependence of the determined onset voltages ($\cdot e$) on the set voltage is shown in Fig. 6.7. Note that a higher set voltage also corresponds to a larger tip-sample separation. With a smaller tip-sample separa-

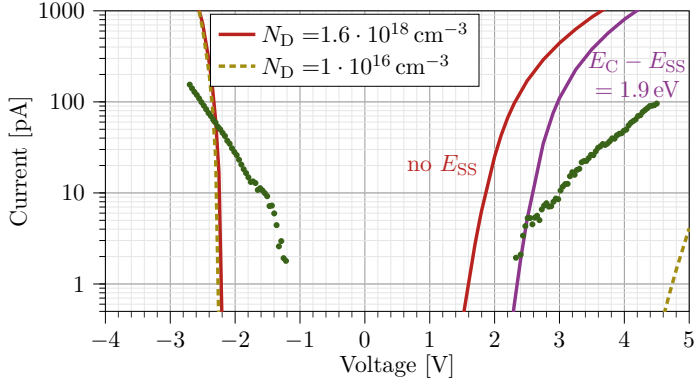


Figure 6.8: $I(V)$ tunnel spectra measured on AlN (cf. spectrum number 1 in Fig.6.2c), using the setpoint -2.5 V and 80 pA. The solid lines represent simulated tunnel spectra for a doping concentration of $N_D = 1.6 \cdot 10^{18} \text{ cm}^{-3}$ and an electron affinity of $\chi = 2.0$ eV. The red line represents a simulated tunnel spectrum without surface state, while the tunnel spectrum with a surface state 1.9 eV below the conduction band (violet line) matches the onset of the measured spectrum. Using a doping concentration of $N_D = 1 \cdot 10^{16} \text{ cm}^{-3}$ and otherwise the same parameters, one obtains the dashed tunnel spectrum.

tion (set voltage -2.5 V and -3.5 V), the voltage onsets are reasonably close to the surface state positions determined from the tunnel current simulation for both ternary (Al,Ga)N layers (cf. Fig. 6.7a,b). However, especially at higher tip-sample separations (set voltage -4.5 V), there are notable deviations. A larger part of the tunnel spectra obtained with a higher tip-sample separation is shifted below the current noise level, and therefore the measured positive current branch onset voltages are apparently shifted to higher values.

6.3.2 Empty surface state of AlN

First, assuming that AlN behaves similarly to GaN, the standard model used above for GaN and (Al,Ga)N is applied to AlN. DFT calculations predict the energy position of the cation-derived dangling bond state of the AlN ($10\bar{1}0$) surface to be (partially) located within the fundamental band gap (cf. Fig. 2.8). Hence, the positive current branch should be offset again by the pinning effect of the surface state. The SIMS data reveal a Si doping concentration ($N_D = 1.6 \cdot 10^{18} \text{ cm}^{-3}$) almost

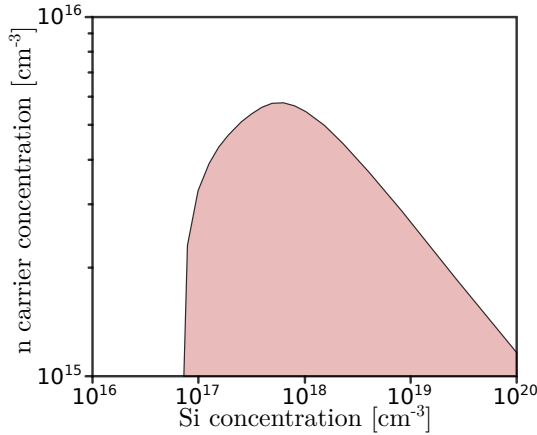


Figure 6.9: Calculated charge carrier concentration as a function of doping concentration. Data is taken from Ref. [168].

identical to that of the ternary nitride layers. Again no compensation is assumed, and the Si donor activation energy is taken as equal to that of GaN and (Al,Ga)N. The electron affinity of AlN is assumed to be $\chi = 2.0$ eV, the upper end of the literature values for polar AlN as mentioned above.

The resulting simulated spectra are shown in Fig. 6.8. The onset of the positive current branch can be fitted by the surface state position (cf. 1.9 eV in Fig. 6.8). However, the slope of the positive current branch is too steep. At the negative current branch, neither the onset nor the slope are in agreement with the measured spectra. Even by changing the tip-sample separation, it is not possible to get a good match between the simulated and measured spectra, since shifting the positive (negative) branch of the simulated closer to the measured spectra will shift away the negative (positive) branch.

Hence, the above-stated assumptions can not be entirely fulfilled. The situation seems to be more complex at the AlN-layer [120, 169, 170]. Indeed, recent literature suggests that higher Si doping concentrations in AlN actually lead to lower charge carrier concentrations [154–156, 168, 171–173]. The lower charge carrier concentration is originating from a doping compensation. In addition, the activation energy is sharply increasing for higher Al concentrations up to 250 meV for pure

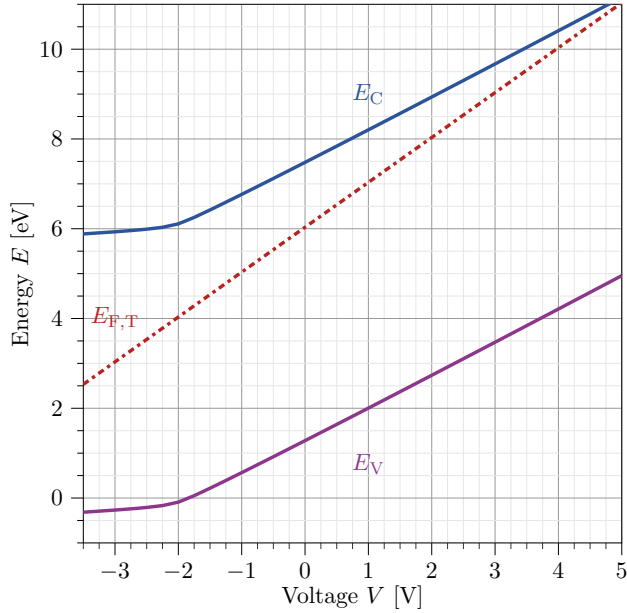


Figure 6.10: Simulated positions of the conduction (blue) and valence (violet) band at the surface as a function of applied voltage at the AlN surface with a doping concentration of $1 \cdot 10^{16} \text{ cm}^{-3}$ (cf. Fig. 6.8). The Fermi level of the tip (red dashed line) is inside the fundamental band gap for the whole simulated voltage range.

AlN [154,155]. Thus, the actual charge carrier concentration is significantly smaller than the Si doping concentration. To take this effect into account, a doping concentration as low as $1 \cdot 10^{16} \text{ cm}^{-3}$ was assumed for a new simulation of the tunnel spectra of AlN.

The simulated AlN tunnel spectrum for a doping concentration of $1 \cdot 10^{16} \text{ cm}^{-3}$ is shown as a yellow dashed line in Fig. 6.8. The onset of the simulated positive current branch is significantly above 4 V, i.e., far above the measured one. Similarly, the simulated negative branch caused by the tip-induced electron accumulation zone does not fit to the measured $I(V)$ spectra: neither the onset nor the slope matches.

The discrepancy of the onset voltages is due to a large contact potential induced by the rather large difference between the AlN electron affinity and the tip's work func-

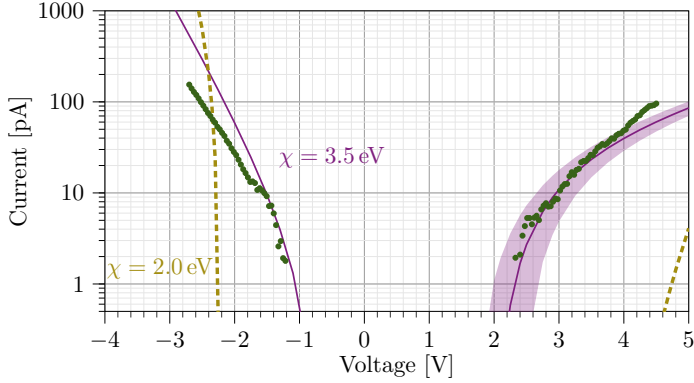


Figure 6.11: $I(V)$ tunnel spectra measured on AlN (cf. spectra number 1 in Fig.6.2c), using the setpoint -2.5 V and 80 pA. The solid lines represent simulated tunnel spectra for a doping concentration of $N_D = 1 \cdot 10^{16} \text{ cm}^{-3}$, an electron affinity of $\chi = 3.5$ eV and a surface state 1.4 eV below the conduction band. The violet shaded area corresponds to a surface state position from 1.0 eV to 1.8 eV below the conduction band. The yellow dashed line represents a simulated tunnel spectra without surface state and a doping concentration of $N_D = 1 \cdot 10^{16} \text{ cm}^{-3}$.

tion. This induces a tip-induced band bending, which keeps the tip's Fermi energy facing the fundamental band gap of AlN for a wide voltage range (cf. Fig. 6.10). As a result tunneling is only possible at voltages larger than $+4.6$ V or smaller than -2.4 V, which is in conflict with the measured onset voltages. In summary, using only literature values for the sample's electrical parameters and assuming only tunneling into or out of bulk states, the measured $I(V)$ spectra of AlN cannot be reproduced by the simulation.

One possibility to resolve the above-described discrepancy between the measured and simulated tunnel spectra of AlN is to use an electron affinity of $\chi = 3.5$ eV instead of 2.0 eV (cf. violet line in Fig. 6.11) in the simulations. However, this value is far away of all the reported literature values for AlN, where an electron affinity of $\chi = 2.0$ eV already represents the upper limit. Even under the assumption of a similar offset between non-polar and polar AlN like for GaN of 0.6 eV, an electron affinity of 3.5 eV is likely too large.

Therefore, the only conflict-free resolution of the discrepancy above-mentioned is incorporating tunneling into and out of AlN's surface states. Indeed both intrinsic

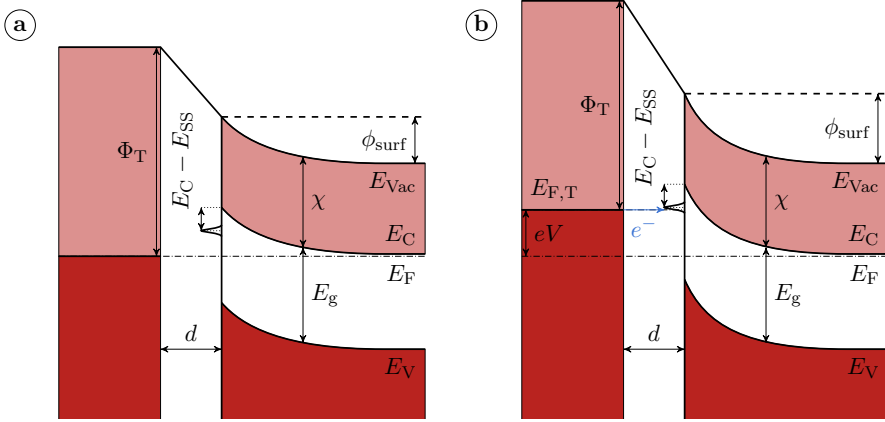


Figure 6.12: (a) Band bending without applied voltage and an empty surface state below the conduction band. Due to the band bending arising from the contact potential, the surface state is far away from the Fermi level and completely empty. (b) By applying a voltage eV the band bending will be increased, but the Fermi level of the tip will also be shifted closer to the surface state. At the onset voltage, the electrons can tunnel from the tip into the surface state.

and extrinsic (i.e., defect-related) surface states can be the origin of tunnel currents. The investigated AlN ($10\bar{1}0$) surface exhibits a rather low defect density since it consists of large atomically flat terraces, separated by steps (cf. Fig. 6.1b). It is thus anticipated that only the intrinsic surface states (i.e., the cation- and anion-derived dangling bond states) contribute to the tunnel current, and no defect-state related current arises.

The presence of surface state-related tunneling necessitates a different approach to determining the energy position of the empty cation-derived surface state. This approach is elucidated in the following. Due to the rather small electron affinity, a contact potential (cf. Sec. 2.4.1) of around $+2.0\text{ V}$ is present between the tip and the AlN surface, which induces a strong upward band bending, as illustrated in Fig. 6.12a. The band bending shifts the cation-derived dangling bond state of the AlN ($10\bar{1}0$) surface upward and thus away from the Fermi level. As a result, the state is completely empty and has no significant influence on the band bending. By applying and increasing a positive voltage, the Fermi level of the tip increases relative to the Fermi level of the sample (cf. Fig. 6.12b). Simultaneously the upward

band bending increases. When the tip's Fermi level exceeds the lowermost end of the Al-derived surface state, tunneling of electrons between the tip and the surface state becomes possible at much smaller voltages than tunneling into bulk states.

Using this model, the energy position of the Al-derived surface state minimum can be deduced from the current onset of the experimental $I(V)$ spectra, provided that the surface potential (i.e., band bending at the surface) at $V = V_{\text{onset}}$ is known. the position of the surface state below the conduction band $E_C - E_{\text{SS}}$ is then given by

$$E_C - E_{\text{SS}} = e(\phi_{\text{surf}} - V_{\text{onset}}) . \quad (6.1)$$

First, the onset voltage of the positive current branch V_{onset} needs to be determined from the measured $I(V)$ curves. Exponential function fitting (cf. Eq. 5.1 in Sec. 5.1.3) yields +1.77 V, while the intersection of the positive voltage branch with the noise level yields +2.2 V. The latter is helpful in the evaluation of the accuracy.

Next, the surface potential $\phi_{\text{surf}}(V, r, E_C - E_{\text{SS}})$ has to be determined at the onset voltage ($V = V_{\text{onset}}$). However, ϕ_{surf} is not directly accessible in STS experiments. In first approximation, it can be calculated theoretically by solving the electrostatic tip-vacuum-semiconductor problem. Using the finite-difference Poisson-solver of P_SpaceChargeLight [79,98,99], the surface potential $\phi_{\text{surf}}(V = V_{\text{onset}}, r, E_C - E_{\text{SS}})$ was derived as a function of $E_C - E_{\text{SS}}$ and tip radii (30, 60, and 120 nm).

Finally, with a known onset voltage V_{onset} and surface potential $\phi_{\text{surf}}(V = V_{\text{onset}}, r, E_C - E_{\text{SS}})$, the surface state energy can be calculated according to Eq. 6.1. Due to the dependence of ϕ_{surf} on both the tip radius and the surface state energy $E_C - E_{\text{SS}}$ a graphical solution is depicted in Fig. 6.13a. In this figure, the difference between the surface potential and the onset voltage (i.e., right-hand side of Eq. 6.1) is shown as a function of the surface state energy $E_C - E_{\text{SS}}$ (i.e., left-hand side of Eq. 6.1) for $V_{\text{onset}} = +1.8$ V and for different tip radii of 30 nm (red line), 60 nm (orange line) as well as 120 nm (blue line). The solution of Eq. 6.1 is then given by the intersection of the function for 60 nm radius (found as best value for (Al,Ga)N)

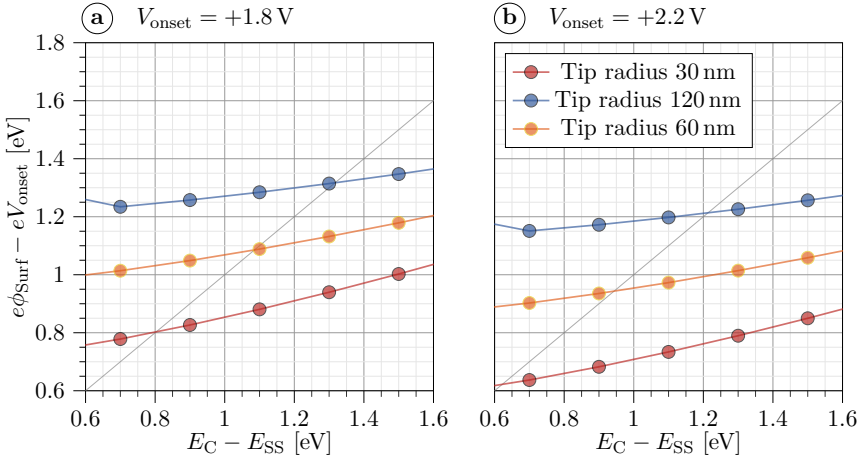


Figure 6.13: (a) Surface state minimum energy in terms of the difference of the onset voltage and the surface potential as a function of surface state position below the conduction band edge for the onset voltage of +1.8 V. (b) Shows the same for an onset voltage at the upper limit of +2.2 V. Both figures show data for different tip radii.

with the bisector (gray line). The other tip radii can be used to estimate the error bar.

For an onset voltage of +1.8 V the surface state energy is found to be at around +1.1 eV. A deviating tip radius in the range of 30 nm and 120 nm leads to a deviation of the surface state position between 0.8 eV and 1.3 eV (cf. Fig. 6.13a). An additional variation of the onset voltage will lead to further errors estimated here using an onset voltage of 2.2 V. This yields a surface state position range between 0.6 eV and 1.2 eV (cf. Fig. 6.13b). Therefore, an error range of $\pm 0.5 \text{ eV}$ should be considered. Combining these values yields a position of the surface state below the conduction band edge of $E_C - E_{\text{SS}} = (1.1 \pm 0.5) \text{ eV}$ for AlN (10 $\bar{1}$ 0).

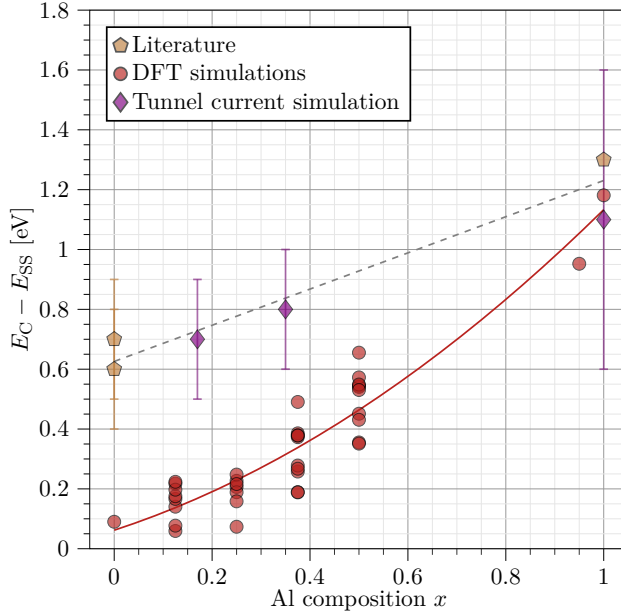


Figure 6.14: Surface state position relative to the conduction band minimum for different Al compositions. The red circles represent DFT calculations [167]. The violet marks correspond to the surface state positions obtained by tunnel current simulation in Fig. 6.2 and Sec. 6.3.2. Literature values for GaN were obtained from Ref. [33, 34, 38], and for AlN from Ref. [41].

6.3.3 Position of the empty surface state in DFT calculations

Next, the experimentally obtained surface state positions derived by tunnel spectra simulation are compared to those obtained by first-principles calculations within DFT and values found in literature.

Figure 6.14 depicts the minimum of the cation-derived surface state relative to the bulk conduction band obtained by several methods. The surface state position obtained by DFT calculations is indicated by red circles [167]. For pure GaN the minimum of the LDOS of the surface state is calculated to be 0.1 eV below the conduction band. For higher Al contents the difference between conduction band edge

and minimum of the surface state increases until it reaches ≈ 1.2 eV for pure AlN. The experimentally obtained values (from the above-described method of simulating tunnel spectra) are depicted as violet diamond symbols for the corresponding Al composition (cf. Fig. 6.14). The values found in literature for pure GaN [33, 34, 38] and AlN [41] are shown as brown pentagons in Fig. 6.14.

Note that the *ab-initio* DFT calculations performed for and presented in this thesis appear to underestimate the energy difference between the empty dangling bond state and the bulk conduction band minimum. For pure GaN the energy difference is calculated here to be 0.1 eV, while previous reports found values around 0.7 eV [33, 34, 38]. The origin of this discrepancy is presumably due to issues with the alignment of the band gap/conduction band between the alloys and AlN, anticipated to be most relevant for moderate Al concentrations. For high Al concentration this problem may not exist. This is corroborated by the fact that for pure GaN the experimental surface state position from literature fits well with the DFT results presented in earlier reports (i.e., 0.7 eV) [33, 34, 38]. The literature value for pure AlN and the present DFT calculation are in good agreement, and fit well with the surface state position determined experimentally here.

Therefore, both the surface state position resulting from measurement and the one resulting from DFT calculation are in good agreement and reveal a weak shift of the surface state toward midgap with increasing Al concentration of roughly $5 \cdot 10^{-3}$ eV/%. This trend is indicated by the gray dashed line in Fig. 6.14.

6.4 Conclusion

In conclusion, tunnel spectra measured by STM were analyzed to unravel the energy position of the group III-derived empty surface state at non-polar m -plane $\text{Al}_x\text{Ga}_{1-x}\text{N}$ surfaces. The presented DFT calculations indicate the same trend as the experimental values for the empty cation-derived dangling bond state on (Al,Ga)N (10 $\bar{1}$ 0) surfaces. With increasing Al concentration, the minimum in energy of the empty dangling bond state shifts toward midgap. The shift is in first approximation linear with a slope of $\approx 5 \cdot 10^{-3}$ eV/%. This is in good agreement

with new DFT calculations presented here and from literature revealing the same trend.

Chapter 7

Summary

The electronic properties of (10 $\bar{1}$ 0) surfaces of ternary solid solution (Al,Ga)N semiconductors with compositions ranging from pure GaN to AlN (i.e., the binary end points) as well as *n*- and *p*-type doping were investigated using cross-sectional scanning tunneling microscopy (XSTM) and spectroscopy (XSTS). The aim of the thesis was to identify the different intrinsic and extrinsic surface states present, their energy position within the fundamental band gap, and their physical origin in order to understand the electronic properties of non-polar (Al,Ga)N (10 $\bar{1}$ 0) surfaces subjected to different surface treatment conditions, i.e., atomically clean and hydroxylated. Particular emphasis has been put on the Fermi-level pinning as a central parameter defining the surfaces' electronic properties and passivation.

The position of surface states within the fundamental band gap can be unraveled quantitatively by STS in conjunction with tunnel current simulations. However, this approach requires detailed knowledge about the physical effects that contribute to the surface band bending during the experimental measurement. Therefore, a systematic preliminary investigation of the influence of different physical parameters on the tunnel current was performed, using a simulation of the tunnel current. For the *n*-doped non-polar III-nitride surfaces, it is found that the tunnel spectra are independent of the size of the fundamental band gap, since for both, negative and positive sample voltages, the measured current originates from tunneling into or out of conduction band states. Other semiconductor parameters, like the electron affinity or the doping concentration, affect the onsets and slopes of the $I(V)$ spectra to different degrees. The tunnel current also depends on the work function of the

probe tip, while its radius has minor influence. The assessment of the simulation provides a detailed understanding of the surface and tip properties derivable from STS data and yields a basis for a proper interpretation of tunneling spectra of ternary (Al,Ga)N (10 $\bar{1}0$) surfaces.

With the help of the findings, the extrinsic and intrinsic surface states present on freshly cleaved and air-exposed non-polar (10 $\bar{1}0$) cross-sectional surfaces of GaN *n-p-n* junctions were investigated quantitatively by STS [P2].

For clean freshly cleaved GaN the *n*-type surface is intrinsically pinned by the empty Ga-derived dangling bond surface state, which is in agreement with earlier reports. In contrast, the Fermi level on *p*-type surface is found to be extrinsically pinned. This pinning is attributed to defect states at the edges of cleavage-induced steps.

After air exposure and subsequent heating in UHV, the pinning level of both *n*- and *p*-doped regions shifted towards the band edge, accompanied by a reduced density of pinning states, and for *p*-doped GaN, a larger apparent band gap was probed by STS. These findings are attributed to the adsorption and dissociation of water molecules during air exposure. The hydroxylation results in a passivation of the Ga dangling bonds by binding with OH- groups and in a passivation of the N dangling bonds by binding with H+. This passivation removes the surface states from the fundamental band gap, by shifting the energy position of the intrinsic (and likely also extrinsic) surface states into the valence band. For a full passivation, no pinning would be expected anymore, and tunneling spectra would be only governed by the tip-induced band bending. However, the surfaces exhibit a reduced band bending on the *n*-type GaN (10 $\bar{1}0$) surface after air exposure and a reduced pinning DOS on *p*-doped GaN surfaces, which points to a partial passivation.

These results reveal an interesting interplay between intrinsic and extrinsic surface states present at the *m*-plane surface of GaN [P2], illustrating the importance of dopant-dependent Fermi-level pinning for the interpretation of tunnel spectra in group III nitride doping structures.

Furthermore, the intrinsic surface states were investigated as a function of the Al concentration in ternary solid solution (Al,Ga)N (10 $\bar{1}0$) surfaces. The energy posi-

tion of the empty cation-derived dangling bond state was extracted from tunneling spectra measured on a set of non-polar m -plane $\text{Al}_x\text{Ga}_{1-x}\text{N}$ ($10\bar{1}0$) surfaces with different compositions. With increasing Al concentration, the minimum of the empty dangling bond state shifts towards midgap. The shift is in first approximation linear with a slope of $\approx 5 \cdot 10^{-3} \text{ eV}/\%$. Complimentary DFT calculations reveal an analogous trend. In addition, a fundamentally different tunneling behavior is found for pure AlN as compared to Ga containing (Al,Ga)N semiconductors. For pure AlN, tunneling into the conduction band is not possible due to the large band gap, the low free carrier concentration, and large tip-induced band bending. Instead, the tunneling spectra are compatible only with tunneling into the intrinsic surface states. This is in contrast with Ga containing (Al,Ga)N ($10\bar{1}0$) surfaces, where tunneling into the bulk states dominates and the surface states show up primarily in the Fermi-level pinning.

The trends and physical effects observed for surface states on non-polar ternary (Al,Ga)N m -plane surfaces can be anticipated to be not limited to this particular alloy, but rather provide a general behavior for intrinsic and extrinsic surface states of most binary and ternary non-polar III-nitride compound semiconductor surfaces. Especially the passivation by hydroxylation offers the prospect to control Fermi-level pinning at sidewall facets of ternary group III nitride nanowires and related nanostructures for both n and p doping, despite clean surfaces exhibit different physical origins of the Fermi level pinning.

Bibliography

- [1] J. W. Harrison and J. R. Hauser, *Theoretical calculations of electron mobility in ternary III-V compounds*, J. Appl. Phys. **47**, 292 (1976).
- [2] S. Adachi, *GaAs, AlAs, and Al_xGa_{1-x}As: Material parameters for use in research and device applications*, J. Appl. Phys. **58**, R1 (1985).
- [3] S. Tiwari and D. J. Frank, *Empirical fit to band discontinuities and barrier heights in III-V alloy systems*, Appl. Phys. Lett. **60**, 630 (1992).
- [4] M. Shur, *GaN based transistors for high power applications*, Solid-State Electron. **42**, 2131 (1998).
- [5] I. Vurgaftman, J. R. Meyer, and L. R. Ram-Mohan, *Band parameters for III-V compound semiconductors and their alloys*, J. Appl. Phys. **89**, 5815 (2001).
- [6] I. Vurgaftman and J. R. Meyer, *Band parameters for nitrogen-containing semiconductors*, J. Appl. Phys. **94**, 3675 (2003).
- [7] K. Takahashi, A. Yoshikawa, and A. Sandhu, editors, *Wide Bandgap Semiconductors*, Springer-Verlag Berlin Heidelberg, 2007.
- [8] D. Zhu, D. J. Wallis, and C. J. Humphreys, *Prospects of III-nitride optoelectronics grown on Si*, Rep. Prog. Phys. **76**, 106501 (2013).
- [9] M. Kneissl, T.-Y. Seong, J. Han, and H. Amano, *The emergence and prospects of deep-ultraviolet light-emitting diode technologies*, Nat. Photonics **13**, 1749 (2019).
- [10] S. Mokkalapati and C. Jagadish, *III-V compound SC for optoelectronic devices*, Mater. Today **12**, 22 (2009).

- [11] G. H. Olsen, C. J. Nuese, and R. T. Smith, *The effect of elastic strain on energy band gap and lattice parameter in III-V compounds*, J. Appl. Phys. **49**, 5523 (1978).
- [12] C. P. Kuo, S. K. Vong, R. M. Cohen, and G. B. Stringfellow, *Effect of mismatch strain on band gap in III-V semiconductors*, J. Appl. Phys. **57**, 5428 (1985).
- [13] J. Zou, D. J. H. Cockayne, and B. F. Usher, *Misfit dislocations and critical thickness in InGaAs/GaAs heterostructure systems*, J. Appl. Phys. **73**, 619 (1993).
- [14] S. C. Jain, M. Willander, and H. Maes, *Stresses and strains in epilayers, stripes and quantum structures of III - V compound semiconductors*, Semicond Sci. Technol. **11**, 641 (1996).
- [15] J. Bartolomé, M. Hanke, D. van Treeck, and A. Trampert, *Strain Driven Shape Evolution of Stacked (In,Ga)N Quantum Disks Embedded in GaN Nanowires*, Nano Lett. **17**, 4654 (2017).
- [16] T. Kehagias, G. P. Dimitrakopoulos, P. Becker, J. Kioseoglou, F. Furtmayr, T. Koukoulou, I. Häusler, A. Chernikov, S. Chatterjee, T. Karakostas, H.-M. Solowan, U. T. Schwarz, M. Eickhoff, and P. Komninou, *Nanostructure and strain in InGaN/GaN superlattices grown in GaN nanowires*, Nanotechnology **24**, 435702 (2013).
- [17] W. Guo, M. Zhang, A. Banerjee, and P. Bhattacharya, *Catalyst-Free In-GaN/GaN Nanowire Light Emitting Diodes Grown on (001) Silicon by Molecular Beam Epitaxy*, Nano Lett. **10**, 3355 (2010).
- [18] Y.-J. Lu, C.-Y. Wang, J. Kim, H.-Y. Chen, M.-Y. Lu, Y.-C. Chen, W.-H. Chang, L.-J. Chen, M. I. Stockman, C.-K. Shih, and S. Gwo, *All-Color Plasmonic Nanolasers with Ultralow Thresholds: Autotuning Mechanism for Single-Mode Lasing*, Nano Lett. **14**, 4381 (2014).
- [19] S. Albert, A. Bengoechea-Encabo, X. Kong, M. A. Sanchez-Garcia, E. Calleja, and A. Trampert, *Monolithic integration of InGaN segments emitting in the*

- blue, green, and red spectral range in single ordered nanocolumns*, Appl. Phys. Lett. **102**, 181103 (2013).
- [20] T. Xu, K. A. Dick, S. Plissard, T. H. Nguyen, Y. Makoudi, M. Berthe, J.-P. Nys., X. Wallart, B. Grandidier, and P. Caroff, *Faceting, composition and crystal phase evolution in III-V antimonide nanowire heterostructures revealed by combining microscopy techniques*, Nanotechnology **23**, 095702 (2012).
- [21] M. Schnedler, I. Lefebvre, T. Xu, V. Portz, G. Patriarche, J.-P. Nys, S. R. Plissard, P. Caroff, M. Berthe, H. Eisele, R. E. Dunin-Borkowski, P. Ebert, and B. Grandidier, *Lazarevicite-type short-range ordering in ternary III-V nanowires*, Phys. Rev. B **94**, 195306 (2016).
- [22] R. M. Feenstra and J. A. Stroscio, *Tunneling spectroscopy of the GaAs(110) surface*, J. Vac. Sci. Technol. B **5**, 923 (1987).
- [23] R. M. Feenstra, *Tunneling spectroscopy of the (110) surface of direct-gap III-V semiconductors*, Phys. Rev. B **50**, 4561 (1994).
- [24] R. M. Feenstra, *Cross-sectional scanning tunnelling microscopy of III-V semiconductor structures*, Semicond. Sci. Technol. **9**, 2157 (1994).
- [25] Ph. Ebert, G. Cox, U. Poppe, and K. Urban, *A STM study of the InP (110) surface*, Ultramicroscopy **42-44**, 871 (1992).
- [26] Ph. Ebert, K. Urban, and M. G. Lagally, *Charge state dependent structural relaxation around anion vacancies on InP(110) and GaP(110) surfaces*, Phys. Rev. Lett. **72**, 840 (1994).
- [27] Ph. Ebert, X. Chen, M. Heinrich, M. Simon, K. Urban, and M. Lagally, *Direct Determination of the Interaction between Vacancies on InP(110) Surfaces*, Phys. Rev. Lett. **76**, 2089 (1996).
- [28] H. Morkoç, S. Strite, G. B. Gao, M. E. Lin, B. Sverdlov, and M. Burns, *Large-band-gap SiC, III-V nitride, and II-VI ZnSe-based semiconductor device technologies*, J. Appl. Phys. **76**, 1363 (1994).

- [29] S. Nakamura, T. Mukai, and M. Senoh, *Candela-class high-brightness In-GaN/AlGaIn double-heterostructure blue-light-emitting diodes*, Appl. Phys. Lett. **64**, 1687 (1994).
- [30] S. Nakamura, M. Senoh, S. Nagahama, N. Iwasa, T. Yamada, T. Matsushita, H. Kiyoku, and Y. Sugimoto, *InGaIn-Based Multi-Quantum-Well-Structure Laser Diodes*, Jpn. J. Appl. Phys. **35**, L74 (1996).
- [31] F. A. Ponce and D. P. Bour, *Nitride-based semiconductors for blue and green light-emitting devices*, Nature **386**, 351 (1997).
- [32] L. Largeau, D. L. Dheeraj, M. Tchernycheva, G. E. Cirlin, and J. C. Harmand, *Facet and in-plane crystallographic orientations of GaN nanowires grown on Si(111)*, Nanotechnology **19**, 155704 (2008).
- [33] C. G. Van de Walle and D. Segev, *Microscopic origins of surface states on nitride surfaces*, J. Appl. Phys. **101**, 081704 (2007).
- [34] L. Lymperakis, P. H. Weidlich, H. Eisele, M. Schnedler, J.-P. Nys, B. Grandidier, D. Stievenard, R. E. Dunin-Borkowski, J. Neugebauer, and Ph. Ebert, *Hidden surface states at non-polar GaN (10 $\bar{1}$ 0) facets: Intrinsic pinning of nanowires*, Appl. Phys. Lett. **103**, 152101 (2013).
- [35] R. González-Hernández, A. González-García, D. Barragán-Yani, and W. López-Pérez, *A comparative DFT study of the structural and electronic properties of nonpolar GaN surfaces*, Appl. Surf. Sci. **314**, 794 (2014).
- [36] M. Himmerlich, A. Eisenhardt, S. Shokhovets, S. Krischok, J. Räthel, E. Speiser, M. D. Neumann, A. Navarro-Quezada, and N. Esser, *Confirmation of intrinsic electron gap states at nonpolar GaN(1 $\bar{1}$ 00) surfaces combining photoelectron and surface optical spectroscopy*, Appl. Phys. Lett. **104**, 171602 (2014).
- [37] M. Landmann, E. Rauls, W. G. Schmidt, M. D. Neumann, E. Speiser, and N. Esser, *GaN m-plane: Atomic structure, surface bands, and optical response*, Phys. Rev. B **91**, 035302 (2015).
- [38] M. Schnedler, V. Portz, H. Eisele, R. E. Dunin-Borkowski, and Ph. Ebert, *Polarity-dependent pinning of a surface state*, Phys. Rev. B **91**, 205309 (2015).

-
- [39] V. Portz, M. Schnedler, H. Eisele, R. E. Dunin-Borkowski, and Ph. Ebert, *Electron affinity and surface states of GaN m -plane facets: Implication for electronic self-passivation*, Phys. Rev. B **97**, 115433 (2018).
- [40] H. Eisele, J. Schuppang, M. Schnedler, M. Duchamp, C. Nenstiel, V. Portz, T. Kure, M. Bügler, A. Lenz, M. Dähne, A. Hoffmann, S. Gwo, S. Choi, J. S. Speck, R. E. Dunin-Borkowski, and Ph. Ebert, *Intrinsic electronic properties of high-quality wurtzite InN*, Phys. Rev. B **94**, 245201 (2016).
- [41] M. S. Miao, A. Janotti, and C. G. Van de Walle, *Reconstructions and origin of surface states on AlN polar and nonpolar surfaces*, Phys. Rev. B **80**, 155319 (2009).
- [42] V. Portz, M. Schnedler, L. Lymperakis, J. Neugebauer, H. Eisele, J.-F. Carlin, R. Butté, N. Grandjean, R. E. Dunin-Borkowski, and P. Ebert, *Fermi-level pinning and intrinsic surface states of $Al_{1-x}In_xN(10\bar{1}0)$ surfaces*, Appl. Phys. Lett. **110**, 022104 (2017).
- [43] E. T. Yu, X. Z. Dang, P. M. Asbeck, S. S. Lau, and G. J. Sullivan, *Spontaneous and piezoelectric polarization effects in III-V nitride heterostructures*, J. Vac. Sci. Technol. B **17**, 1742 (1999).
- [44] B. S. Eller, J. Yang, and R. J. Nemanich, *Polarization Effects of GaN and AlGaN: Polarization Bound Charge, Band Bending, and Electronic Surface States*, J. Electron. Mater. **43**, 4560 (2014).
- [45] J. Bai, L. Jiu, N. Poyiatzis, P. Fletcher, Y. Gong, and T. Wang, *Optical and polarization properties of nonpolar InGaN-based light-emitting diodes grown on micro-rod templates*, Sci. Rep. **9**, 9770 (2019).
- [46] B. A. Haskell, S. Nakamura, S. P. DenBaars, and J. S. Speck, *Progress in the growth of nonpolar gallium nitride*, Phys. Status Solidi B **244**, 2847 (2007).
- [47] G. Binnig, H. Rohrer, C. Gerber, and E. Weibel, *Surface Studies by Scanning Tunneling Microscopy*, Phys. Rev. Lett. **49**, 57 (1982).
- [48] G. Binnig, H. Rohrer, C. Gerber, and E. Weibel, *Tunneling through a controllable vacuum gap*, Appl. Phys. Lett. **40**, 178 (1982).

- [49] G. Binnig and H. Rohrer, *Scanning tunneling microscopy*, Helv. Phys. Acta **55**, 726 (1982).
- [50] G. Binnig, H. Rohrer, C. Gerber, and E. Weibel, *(111) facets as the origin of reconstructed Au(110) surfaces*, Surf. Sci. Lett. **131**, L379 (1983).
- [51] G. Binnig and H. Rohrer, *Scanning tunneling microscopy*, Surf. Sci. **126**, 236 (1983).
- [52] F. Hund, *Zur Deutung der Molekelspektren. I*, Z. Phys. **40**, 742 (1927).
- [53] F. Hund, *Zur Deutung der Molekelspektren. II*, Z. Phys. **42**, 93 (1927).
- [54] F. Hund, *Zur Deutung der Molekelspektren. III.*, Z. Phys. **43**, 805 (1927).
- [55] G. Gamow, *Zur Quantentheorie des Atomkernes*, Z. Phys. **51**, 204 (1928).
- [56] G. Wentzel, *Eine Verallgemeinerung der Quantenbedingungen für die Zwecke der Wellenmechanik*, Z. Phys. **38**, 518 (1926).
- [57] H. A. Kramers, *Wellenmechanik und halbzahlige Quantisierung*, Z. Phys. **39**, 828 (1926).
- [58] L. Brillouin, *La mécanique ondulatoire de Schrödinger; une méthode générale de résolution par approximations successives*, Compt. Rend. Hebd. Seances Acad. Sci. **183**, 24 (1926).
- [59] M. Schnedler, *Quantitative scanning tunneling spectroscopy of non-polar compound semiconductor surfaces*, Dissertation, RWTH Aachen University, 2015.
- [60] J. Frenkel, *Einführung in die Wellenmechanik*, Springer-Verlag Berlin Heidelberg, 1929.
- [61] F. Schwabl, *Quantenmechanik - Eine Einführung*, Springer-Verlag Berlin Heidelberg, 2007.
- [62] W. Nolting, *Grundkurs Theoretische Physik 5/1*, Springer-Verlag Berlin Heidelberg, 7. edition, 2009.
- [63] B. Voigtländer, *Scanning Probe Microscopy: Atomic Force Microscopy and Scanning Tunneling Microscopy*, Nanoscience and Technology, Springer-Verlag Berlin Heidelberg, 2015.

-
- [64] W. Demtröder, *Experimentalphysik 3*, Springer-Verlag Berlin Heidelberg, 4. edition, 2010.
- [65] C. Kittel, *Einführung in die Festkörperphysik*, Oldenbourg Wissenschaftsverlag, 2013.
- [66] J. Bardeen, *Tunnelling from a many-particle point of view*, Phys. Rev. Lett. **6**, 57 (1961).
- [67] J. G. Simmons, *Generalized Formula for the Electric Tunnel Effect between Similar Electrodes Separated by a Thin Insulating Film*, J. Appl. Phys. **34**, 1793 (1963).
- [68] C. J. Chen, *Introduction to Scanning Tunneling Microscopy*, Oxford University Press, Oxford, 1993.
- [69] W. A. Harrison, *Tunneling from an Independent-Particle Point of View*, Phys. Rev. **123**, 85 (1961).
- [70] J. Tersoff and D. R. Hamann, *Theory and Application for the Scanning Tunneling Microscope*, Phys. Rev. Lett. **50**, 1998 (1983).
- [71] J. Tersoff and D. R. Hamann, *Theory of the scanning tunneling microscope*, Phys. Rev. B **31**, 805 (1985).
- [72] C. J. Chen, *Tunneling matrix elements in three-dimensional space: The derivative rule and the sum rule*, Phys. Rev. B **42**, 8841 (1990).
- [73] N. F. Mott, *Note on the contact between a metal and an insulator or semiconductor*, Math. Proc. Cambridge Philos. Soc. **34**, 568–572 (1938).
- [74] W. Schottky, *Abweichungen vom Ohmschen Gesetz in Halbleitern*, Phys. Z. **41**, 570 (1940).
- [75] J. Bardeen, *Surface States and Rectification at a Metal Semi-Conductor Contact*, Phys. Rev. **71**, 717 (1947).
- [76] R. M. Feenstra, Y. Dong, M. P. Semtsiv, and W. T. Masselink, *Influence of Tip-induced Band Bending on Tunneling Spectra of Semiconductor Surfaces*, Nanotechnology **18**, 044015 (2006).

- [77] R. Seiwatz and M. Green, *Space Charge Calculations for Semiconductors*, J. Appl. Phys. **29**, 1034 (1958).
- [78] S. M. Sze and K. K. Ng, *Physics of Semiconductor Devices*, Wiley-Interscience, New York, 3. edition, 2007.
- [79] M. Schnedler, V. Portz, P. H. Weidlich, R. E. Dunin-Borkowski, and Ph. Ebert, *Quantitative description of photoexcited scanning tunneling spectroscopy and its application to the GaAs(110) surface*, Phys. Rev. B **91**, 235305 (2015).
- [80] I. E. Tamm, *Über eine mögliche Art der Elektronenbindung an Kristalloberflächen*, Z. Phys. Sowjetunion **1**, 733 (1932).
- [81] W. Shockley, *On the Surface States Associated with a Periodic Potential*, Phys. Rev. **56**, 317 (1939).
- [82] W. Mönch, *Surface States*, Springer-Verlag Berlin Heidelberg, 1995.
- [83] V. Heine, *Theory of Surface States*, Phys. Rev. **138**, A1689 (1965).
- [84] F. Yndurain, *Density of states and barrier height of metal-Si contacts*, J. Phys. C: Solid State Phys. **4**, 2849 (1971).
- [85] C. Tejedor, F. Flores, and E. Louis, *The metal-semiconductor interface: Si (111) and zinblende (110) junctions*, J. Phys. C: Solid State Phys. **10**, 2163 (1977).
- [86] F. Flores, A. Muñoz, and J. Durán, *Semiconductor interface formation: The role of the induced density of interface states*, Appl. Surf. Sci. **41-42**, 144 (1990).
- [87] W. Mönch, *Empirical tight-binding calculation of the branch-point energy of the continuum of interface-induced gap states*, J. Appl. Phys. **80**, 5076 (1996).
- [88] V. M. Bermudez and J. P. Long, *Chemisorption of H₂O on GaN(0001)*, Surf. Sci. **450**, 98 (2000).
- [89] P. Lorenz, *Oberflächen- und Grenzflächeneigenschaften von polaren Galliumnitrid-Schichten*, Dissertation, Technische Universität Ilmenau, Fakultät für Mathematik und Naturwissenschaften, 2011.

-
- [90] N. Kharche, M. S. Hybertsen, and J. T. Muckerman, *Computational investigation of structural and electronic properties of aqueous interfaces of GaN, ZnO, and a GaN/ZnO alloy*, Phys. Chem. Chem. Phys. **16**, 12057 (2014).
- [91] D. Segev and C. G. Van de Walle, *Origins of Fermi-level pinning on GaN and InN polar and nonpolar surfaces*, Europhys. Lett. **76**, 305 (2006).
- [92] J. P. Ibe, P. P. Bey, S. L. Brandow, R. A. Brizzolara, N. A. Burnham, D. P. DiLella, K. P. Lee, C. R. K. Marrian, and R. J. Colton, *On the electrochemical etching of tips for scanning tunneling microscopy*, J. Vac. Sci. Technol. A **8**, 3570 (1990).
- [93] A. R. Smith, S. Gwo, K. Sadra, Y. C. Shih, B. G. Streetman, and C. K. Shih, *Comparative study of cross-sectional scanning tunneling microscopy/spectroscopy on III-V hetero- and homostructures: Ultrahigh vacuum-cleaved versus sulfide passivated*, J. Vac. Sci. Technol. B **12**, 2610 (1994).
- [94] O. Flebbe, H. Eisele, T. Kalka, F. Heinrichsdorff, A. Krost, D. Bimberg, and M. Dähne-Prietsch, *Atomic structure of stacked InAs quantum dots grown by metal-organic chemical vapor deposition*, J. Vac. Sci. Technol. B **17**, 1639 (1999).
- [95] V. Portz, *Investigation of ternary nitride semiconductor alloys by scanning tunneling microscopy*, Dissertation, RWTH Aachen University, 2017.
- [96] L. Zhang, V. Portz, M. Schnedler, L. Jin, Y. Wang, X. Hao, H. Eisele, R. E. Dunin-Borkowski, and Philipp Ebert, *Dislocation bending in GaN/step-graded (Al,Ga)N/AlN buffer layers on Si(111) investigated by STM and STEM*, Philos. Mag. **98**, 3072 (2018).
- [97] N. D. Jäger, E. R. Weber, K. Urban, and Ph. Ebert, *Importance of carrier dynamics and conservation of momentum in atom-selective STM imaging and band gap determination of GaAs(110)*, Phys. Rev. B **67**, 165327 (2003).
- [98] M. Schnedler, R. E. Dunin-Borkowski, and Ph. Ebert, *Importance of quantum correction for the quantitative simulation of photoexcited scanning tunneling spectra of semiconductor surfaces*, Phys. Rev. B **93**, 195444 (2016).

- [99] M. Schnedler, *P_SpaceChargeLight (April 2021)*, https://github.com/mschnedler/P_SpaceChargeLight, retrieved, June 2021.
- [100] R. M. Feenstra, *Electrostatic Potential for a Hyperbolic Probe Tip near a Semiconductor*, J. Vac. Sci. Technol. B **21**, 2080 (2003).
- [101] R. M. Feenstra, *SEMITIP version 6 (May 2011)*, http://www.andrew.cmu.edu/user/feenstra/semitip_v6, retrieved, June 2021.
- [102] J. G. Simmons, *Potential Barriers and Emission-Limited Current Flow Between Closely Spaced Parallel Metal Electrodes*, J. Appl. Phys. **35**, 2472 (1964).
- [103] J. Frenkel, *On the Electrical Resistance of Contacts between Solid Conductors*, Phys. Rev. **36**, 1604 (1930).
- [104] N. Ishida, K. Sueoka, and R. M. Feenstra, *Influence of surface states on tunneling spectra of n-type GaAs(110) surfaces*, Phys. Rev. B **80**, 075320 (2009).
- [105] L. Ivanova, S. Borisova, H. Eisele, M. Dähne, A. Laubsch, and Ph. Ebert, *Surface states and origin of the Fermi level pinning on nonpolar GaN(100) surfaces*, Appl. Phys. Lett. **93**, 192110 (2008).
- [106] Ph. Ebert, L. Ivanova, and H. Eisele, *Scanning tunneling microscopy on unpinned GaN(1 $\bar{1}$ 00) surfaces: Invisibility of valence-band states*, Phys. Rev. B **80**, 085316 (2009).
- [107] W. Götz, N. M. Johnson, C. Chen, H. Liu, C. Kuo, and W. Imler, *Activation energies of Si donors in GaN*, Appl. Phys. Lett. **68**, 3144 (1996).
- [108] C. G. Van de Walle, C. Stampfl, and J. Neugebauer, *Theory of doping and defects in III-V nitrides*, J. Cryst. Growth **189-190**, 505 (1998).
- [109] H. Wang and A.-B. Chen, *Calculation of shallow donor levels in GaN*, J. Appl. Phys. **87**, 7859 (2000).
- [110] M. Bertelli, P. Löptien, M. Wenderoth, A. Rizzi, R. G. Ulbrich, M. C. Righi, A. Ferretti, L. Martin-Samos, C. M. Bertoni, and A. Catellani, *Atomic and*

-
- electronic structure of the nonpolar GaN(1 $\bar{1}$ 00) surface*, Phys. Rev. B **80**, 115324 (2009).
- [111] H. Eisele and Ph. Ebert, *Non-polar group-III nitride semiconductor surfaces*, Phys. Stat. Sol. RRL **6**, 359 (2012).
- [112] H. A. Storms, K. F. Brown, and J. D. Stein, *Evaluation of a cesium positive ion source for secondary ion mass spectrometry*, Anal. Chem. **49**, 2023 (1977).
- [113] C. W. Magee, *Depth Profiling of n-Type Dopants in Si and GaAs Using Cs⁺ Bombardment Negative Secondary Ion Mass Spectrometry in Ultrahigh Vacuum*, J. Electrochem. Soc. **126**, 660 (1979).
- [114] J. Maul and K. Wittmaack, *Secondary ion emission from silicon and silicon oxide*, Surf. Sci. **47**, 358 (1975), Proceedings of the Third Symposium on Surface Physics University of Utrecht, The Netherlands 26-28 June 1974.
- [115] R. J. MacDonald and B. V. King, *SIMS - Secondary Ion Mass Spectrometry*, pages 117–147, Springer Berlin Heidelberg, Berlin, Heidelberg, 1992.
- [116] C. Andersen, *Analytic methods for the ion microprobe mass analyzer. Part II.*, Int. J. Mass Spectrom. Ion Phys. **3**, 413 (1970).
- [117] J. Morabito and J. Tsai, *In-depth profiles of phosphorus ion-implanted silicon by Auger spectroscopy and secondary ion emission*, Surf. Sci. **33**, 422 (1972).
- [118] D. Elwell and M. M. Elwell, *Crystal growth of gallium nitride*, Prog. Cryst. Growth Charact. **17**, 53 (1988).
- [119] S. Strite and H. Morkoç, *GaN, AlN, and InN: A review*, J. Vac. Sci. Technol. B **10**, 1237 (1992).
- [120] C. G. Van de Walle and J. Neugebauer, *First-principles calculations for defects and impurities: Applications to III-nitrides*, J. Appl. Phys. **95**, 3851 (2004).
- [121] M. G. Ganchenkova and R. M. Nieminen, *Nitrogen Vacancies as Major Point Defects in Gallium Nitride*, Phys. Rev. Lett. **96**, 196402 (2006).

- [122] J. Buckeridge, C. R. A. Catlow, D. O. Scanlon, T. W. Keal, P. Sherwood, M. Miskufova, A. Walsh, S. M. Woodley, and A. A. Sokol, *Determination of the Nitrogen Vacancy as a Shallow Compensating Center in GaN Doped with Divalent Metals*, Phys. Rev. Lett. **114**, 016405 (2015).
- [123] Y. Fujii, R. Micheletto, and G. Alfieri, *The Electronic Properties of Chlorine in GaN: An Ab Initio Study*, Phys. Status Solidi B **258**, 2000303 (2021).
- [124] Q. Yan, A. Janotti, M. Scheffler, and C. G. Van de Walle, *Role of nitrogen vacancies in the luminescence of Mg-doped GaN*, Appl. Phys. Lett. **100**, 142110 (2012).
- [125] S. Limpijumnong and C. G. Van de Walle, *Diffusivity of native defects in GaN*, Phys. Rev. B **69**, 035207 (2004).
- [126] A. Kyrtsov, M. Matsubara, and E. Bellotti, *Migration mechanisms and diffusion barriers of carbon and native point defects in GaN*, Phys. Rev. B **93**, 245201 (2016).
- [127] J. L. Lyons and C. G. Van de Walle, *Computationally predicted energies and properties of defects in GaN*, npj Comput. Mater. **3**, 12 (2017).
- [128] M. Heinrich, C. Domke, Ph. Ebert, and K. Urban, *Charged steps on III-V compound semiconductor surfaces*, Phys. Rev. B **53**, 10894 (1996).
- [129] S. Gaan, G. He, R. M. Feenstra, J. Walker, and E. Towe, *Size, shape, composition, and electronic properties of InAs/GaAs quantum dots by scanning tunneling microscopy and spectroscopy*, J. Appl. Phys. **108**, 114315 (2010).
- [130] S. Gaan, R. Feenstra, Ph. Ebert, R. Dunin-Borkowski, J. Walker, and E. Towe, *Structure and electronic spectroscopy of steps on GaAs(110) surfaces*, Surf. Sci. **606**, 28 (2012).
- [131] A. Sabitova, Ph. Ebert, A. Lenz, S. Schaafhausen, L. Ivanova, M. Dähne, A. Hoffmann, R. E. Dunin-Borkowski, A. Förster, B. Grandidier, and H. Eisele, *Intrinsic bandgap of cleaved ZnO(11 $\bar{2}$ 0) surfaces*, Appl. Phys. Lett. **102**, 021608 (2013).

-
- [132] P. Capiod, T. Xu, J. P. Nys, M. Berthe, G. Patriarche, L. Lymperakis, J. Neugebauer, P. Caroff, R. E. Dunin-Borkowski, Ph. Ebert, and B. Grandidier, *Band offsets at zincblende-wurtzite GaAs nanowire sidewall surfaces*, Appl. Phys. Lett. **103**, 122104 (2013).
- [133] N. Jäger, M. Marso, M. Salmeron, E. R. Weber, K. Urban, and Ph. Ebert, *Physics of imaging $p - n$ junctions by scanning tunneling microscopy and spectroscopy*, Phys. Rev. B **67**, 165307 (2003).
- [134] R. M. Feenstra, A. Vaterlaus, E. T. Yu, P. D. Kirchner, C. L. Lin, J. M. Woodall, and G. D. Pettit, *Semiconductor Interfaces at the Sub-Nanometer Scale*, chapter Atomic Scale Analysis of Semiconductor Interfaces, pages 127–137, Springer, Dordrecht, 1993.
- [135] S. D. Wolter, *Kinetic Study of the Oxidation of Gallium Nitride in Dry Air*, J. Electrochem. Soc. **145**, 629 (1998).
- [136] I. Rousseau, G. Callsen, G. Jacopin, J.-F. Carlin, R. Butté, and N. Grandjean, *Optical absorption and oxygen passivation of surface states in III-nitride photonic devices*, J. Appl. Phys. **123**, 113103 (2018).
- [137] X. Shen, P. B. Allen, M. S. Hybertsen, and J. T. Muckerman, *Water Adsorption on the GaN (10 $\bar{1}$ 0) Nonpolar Surface*, J. Phys. Chem. C **113**, 3365 (2009).
- [138] J. Wang, L. S. Pedroza, A. Poissier, and M. V. Fernández-Serra, *Water Dissociation at the GaN(10 $\bar{1}$ 0) Surface: Structure, Dynamics and Surface Acidity*, J. Phys. Chem. C **116**, 14382 (2012).
- [139] S.-Y. Wu, L.-W. Lang, P.-Y. Cai, Y.-W. Chen, Y.-L. Lai, M.-W. Lin, Y.-J. Hsu, W.-I. Lee, J.-L. Kuo, M.-F. Luo, and C.-C. Kuo, *Microscopic evidence for the dissociation of water molecules on cleaved GaN(1 $\bar{1}$ 00)*, Phys. Chem. Chem. Phys. **20**, 1261 (2018).
- [140] A. C. Meng, J. Cheng, and M. Sprik, *Density Functional Theory Calculation of the Band Alignment of (10 $\bar{1}$ 0) $In_xGa_{1-x}N$ /Water Interfaces*, J. Phys. Chem. B **120**, 1928 (2016).

- [141] L. Lymparakis, J. Neugebauer, M. Himmerlich, S. Krischok, M. Rink, J. Kröger, and V. M. Polyakov, *Adsorption and desorption of hydrogen at nonpolar GaN(1 $\bar{1}$ 00) surfaces: Kinetics and impact on surface vibrational and electronic properties*, Phys. Rev. B **95**, 195314 (2017).
- [142] P. Lorenz, R. Gutt, T. Haensel, M. Himmerlich, J. A. Schaefer, and S. Krischok, *Interaction of GaN(0001)-2 \times 2 surfaces with H₂O*, phys. stat. sol. c **7**, 169 (2010).
- [143] X. Zhang and S. Ptasinska, *Electronic and chemical structure of the H₂O/GaN(0001) interface under ambient conditions*, Sci. Rep. **6**, 24848 (2016).
- [144] M. Ptasinska, J. Piechota, and S. Krukowski, *Adsorption of Hydrogen at the GaN(000 $\bar{1}$) Surface: An Ab Initio Study*, J. Phys. Chem. C **119**, 11563 (2015).
- [145] L. Janicki, J. Misiewicz, G. Cywiński, M. Sawicka, C. Skierbiszewski, and R. Kudrawiec, *Surface potential barrier in m-plane GaN studied by contactless electroreflectance*, Appl. Phys. Express **9**, 021002 (2016).
- [146] H. Wang, H. Zhang, J. Liu, D. Xue, H. Liang, and X. Xia, *Hydroxyl Group Adsorption on GaN (0001) Surface: First Principles and XPS Studies*, J. Electron. Mater. **48**, 2430 (2019).
- [147] M. Sato, Y. Imazeki, T. Takeda, M. Kobayashi, S. Yamamoto, I. Matsuda, J. Yoshinobu, Y. Nakano, and M. Sugiyama, *Atomistic-Level Description of GaN/Water Interface by a Combined Spectroscopic and First-Principles Computational Approach*, J. Phys. Chem. C **124**, 12466 (2020).
- [148] D. Franke, A. Luisa da Rosa, M. Lorke, and T. Frauenheim, *Electronic and Optical Properties of Functionalized GaN-(10 $\bar{1}$ 0) Surfaces using Hybrid-Density Functionals*, Phys. Stat. Sol. B **256**, 1800455 (2019).
- [149] Ernst Ruska-Centre for Microscopy and Spectroscopy with Electrons (ER-C), *FEI Titan G2 80-200 Crewley*, Journal of large-scale research facilities **2**, A43 (2016).

-
- [150] K. Besocke and H. Wagner, *Adsorption of W on W(110): Work-Function Reduction and Island Formation*, Phys. Rev. B **8**, 4597 (1973).
- [151] C. J. Fall, N. Binggeli, and A. Baldereschi, *Theoretical maps of work-function anisotropies*, Phys. Rev. B **65**, 045401 (2001).
- [152] S. Loth, M. Wenderoth, R. G. Ulbrich, S. Malzer, and G. H. Döhler, *Connection of anisotropic conductivity to tip-induced space-charge layers in scanning tunneling spectroscopy of p-doped GaAs*, Phys. Rev. B **76**, 235318 (2007).
- [153] A. P. Wijnheijmer, J. K. Garleff, M. A. v. d. Heijden, and P. M. Koenraad, *Influence of the tip work function on scanning tunneling microscopy and spectroscopy on zinc doped GaAs*, J. Vac. Sci. Technol. B **28**, 1086 (2010).
- [154] R. Collazo, S. Mita, J. Xie, A. Rice, J. Tweedie, R. Dalmau, and Z. Sitar, *Progress on n-type doping of AlGaN alloys on AlN single crystal substrates for UV optoelectronic applications*, Phys. Status Solidi C **8**, 2031 (2011).
- [155] I. S. Bryan, *Al-rich AlGaN and AlN Growth on Bulk AlN Single Crystal Substrates*, Dissertation, North Carolina State University, 2015.
- [156] I. Bryan, Z. Bryan, S. Washiyama, P. Reddy, B. Gaddy, B. Sarkar, M. H. Breckenridge, Q. Guo, M. Bobea, J. Tweedie, S. Mita, D. Irving, R. Collazo, and Z. Sitar, *Doping and compensation in Al-rich AlGaN grown on single crystal AlN and sapphire by MOCVD*, Appl. Phys. Lett. **112**, 062102 (2018).
- [157] J. I. Pankove and H. Schade, *Photoemission from GaN*, Appl. Phys. Lett. **25**, 53 (1974).
- [158] C. I. Wu, A. Kahn, N. Taskar, D. Dorman, and D. Gallagher, *GaN (0001)-(1 × 1) surface: Composition and electronic properties*, J. Appl. Phys. **83**, 4249 (1998).
- [159] T. Kozawa, T. Mori, T. Ohwaki, Y. Taga, and N. Sawaki, *UV Photoemission Study of AlGaN Grown by Metalorganic Vapor Phase Epitaxy*, Jpn. J. Appl. Phys. **39**, L772 (2000).

- [160] S. P. Grabowski, M. Schneider, H. Nienhaus, W. Mönch, R. Dimitrov, O. Ambacher, and M. Stutzmann, *Electron affinity of $Al_xGa_{1-x}N(0001)$ surfaces*, Appl. Phys. Lett. **78**, 2503 (2001).
- [161] P. G. Moses, M. Miao, Q. Yan, and C. G. Van de Walle, *Hybrid functional investigations of band gaps and band alignments for AlN, GaN, InN, and InGaN*, J. Chem. Phys. **134**, 084703 (2011).
- [162] P. Strak, P. Kempisty, K. Sakowski, and S. Krukowski, *Ab initio determination of electron affinity of polar nitride surfaces, clean and under Cs coverage*, J. Vac. Sci. Technol. A **35**, 021406 (2017).
- [163] V. M. Bermudez, T. M. Jung, K. Doverspike, and A. E. Wickenden, *The growth and properties of Al and AlN films on GaN(0001)-(1 × 1)*, J. Appl. Phys. **79**, 110 (1996).
- [164] C. I. Wu, A. Kahn, E. S. Hellman, and D. N. E. Buchanan, *Electron affinity at aluminum nitride surfaces*, Appl. Phys. Lett. **73**, 1346 (1998).
- [165] C. I. Wu and A. Kahn, *Electronic states at aluminium nitride (0001)-1 × 1 surface*, Appl. Phys. Lett. **74**, 546 (1999).
- [166] P. Reddy, I. Bryan, Z. Bryan, J. Tweedie, S. Washiyama, R. Kirste, S. Mita, R. Collazo, and Z. Sitar, *Charge neutrality levels, barrier heights, and band offsets at polar AlGaN*, Appl. Phys. Lett. **107**, 091603 (2015).
- [167] L. Lymperakis, *private communication*, 2021.
- [168] J. S. Harris, J. N. Baker, B. E. Gaddy, I. Bryan, Z. Bryan, K. J. Mirrielees, P. Reddy, R. Collazo, Z. Sitar, and D. L. Irving, *On compensation in Si-doped AlN*, Appl. Phys. Lett. **112**, 152101 (2018).
- [169] C. Stampfl and C. G. Van de Walle, *Theoretical investigation of native defects, impurities, and complexes in aluminum nitride*, Phys. Rev. B **65**, 155212 (2002).
- [170] D. F. Hevia, C. Stampfl, F. Viñes, and F. Illas, *Microscopic origin of n-type behavior in Si-doped AlN*, Phys. Rev. B **88**, 085202 (2013).

- [171] Y. Taniyasu, M. Kasu, and N. Kobayashi, *Intentional control of n-type conduction for Si-doped AlN and Al_xGa_{1-x}N (0.42 < x < 1)*, Appl. Phys. Lett. **81**, 1255 (2002).
- [172] Y. Shimahara, H. Miyake, K. Hiramatsu, F. Fukuyo, T. Okada, H. Takaoka, and H. Yoshida, *Growth of High-Quality Si-Doped AlGa_xN by Low-Pressure Metalorganic Vapor Phase Epitaxy*, Jpn. J. Appl. Phys. **50**, 095502 (2011).
- [173] F. Mehnke, T. Wernicke, H. Pingel, C. Kuhn, C. Reich, V. Kueller, A. Knauer, M. Lapeyrade, M. Weyers, and M. Kneissl, *Highly conductive n-Al_xGa_{1-x}N layers with aluminum mole fractions above 80%*, Appl. Phys. Lett. **103**, 212109 (2013).

List of own publications

- [P1] Y. Wang, M. Schnedler, Q. Lan, F. Zheng, **L. Freter**, Y. Lu, U. Breuer, H. Eisele, J.-F. Carlin, R. Butté, N. Grandjean, R. E. Dunin-Borkowski, and Ph. Ebert, *Interplay of anomalous strain relaxation and minimization of polarization changes at nitride semiconductor heterointerfaces*, Phys. Rev. B **102**, 245304 (2020).
- [P2] **L. Freter**, Y. Wang, M. Schnedler, J.-F. Carlin, R. Butté, N. Grandjean, H. Eisele, R. E. Dunin-Borkowski, and Ph. Ebert, *Interplay of intrinsic and extrinsic states in pinning and passivation of m-plane facets of GaN n-p-n junctions*, J. Appl. Phys. **128**, 185701 (2020).
- [P3] S. Appelfeller, K. Holtgrewe, M. Franz, **L. Freter**, C. Hassenstein, H.-F. Jirschik, S. Sanna, and M. Dähne, *Continuous crossover from two-dimensional to one-dimensional electronic properties for metallic silicide nanowires*, Phys. Rev. B **102**, 115433 (2020).
- [P4] S. Appelfeller, M. Franz, **L. Freter**, C. Hassenstein, H.-F. Jirschik, and M. Dähne, *Growth and characterization of Tb silicide nanostructures on Si(hhk) substrates*, Phys. Rev. Materials **3**, 126002 (2019).

Acknowledgment

First of all, I would like to thank Prof. Dr. R. E. Dunin-Borkowski for generously offering me the opportunity to prepare my Ph.D. thesis at the Institute for Microstructure Research of the Peter Grünberg Institute at the Forschungszentrum Jülich.

I would like to express my sincere gratitude to Priv.-Doz. Dr. Ph. Ebert for supervising this thesis, for outstanding guidance and support during measurements and data analysis as well as for many scientific discussions.

Furthermore, I would like to thank Prof. Dr. T. Taubner from the I. Physikalisches Institut (IA) der RWTH Aachen for the co-supervision of my Ph.D. thesis.

I would like to thank Prof. Dr. N. Grandjean, Dr. R. Butté, and Dr. J.-F. Carlin from the Institute of Physics, École Polytechnique Fédérale de Lausanne (EPFL), Switzerland, for generously providing me with the binary GaN samples and for their help with the interpretation and assessment of the experimental results.

In addition, I want to thank Dr. L. Zhang from the State Key Laboratory for Crystal Materials at Shandong University, People's Republic of China, for providing the ternary (Al,Ga)N samples.

Moreover, I would like to thank Dr. L. Lymperakis from the Computational Materials Department at the Max-Planck-Institute für Eisenforschung GmbH for the performance of the DFT calculations and fruitful discussions.

I also would like to thank Prof. Dr. H. Eisele from the Institut für Festkörperphysik at the Technische Universität Berlin for valuable scientific discussions.

I would like to thank Dr. M. Schnedler for his tremendous help, especially with the measurements and simulations, and in general for the great support during the whole Ph.D. period.

The scanning electron microscope measurements were done by D. Meertens from ER-C, E. Würtz from PGI-5, and J. Friedrich from PGI-7 at the Forschungszentrum Jülich. For this I would like to express my sincere thanks.

Moreover, I would like to thank U. Breuer from the ZEA-3 at the Forschungszentrum Jülich, for the SIMS measurements.

Furthermore, I would like to express my sincere thankfulness to my colleagues Dr. Q. Lan, Dr. Y. Lu, and K. Ji, and former colleagues Dr. Y. Wang and Dr. V. Portz for the tremendous help and countless hours spent on scientific discussions.

My thanks also go to Prof. Dr. M. Dähne, Dr. S. Appelfeller, M. Franz, Dr. A. Lenz, D. Rosenzweig, for many scientific discussions.

Finally, my thanks also go to my parents, who have always supported me.

Band / Volume 71

Investigating the Interaction between π -Conjugated Organic Molecules and Metal Surfaces with Photoemission Tomography

X. Yang (2021), xviii, 173 pp

ISBN: 978-3-95806-584-0

Band / Volume 72

Three-Dimensional Polymeric Topographies for Neural Interfaces

F. Milos (2021), 133 pp

ISBN: 978-3-95806-586-4

Band / Volume 73

Development, characterization, and application of compliant intracortical implants

K. Srikantharajah (2021), xiv, 155, xv-xvii pp

ISBN: 978-3-95806-587-1

Band / Volume 74

Modelling, implementation and characterization of a Bias-DAC in CMOS as a building block for scalable cryogenic control electronics for future quantum computers

P. N. Vliex (2021), xiv, 107, xv-xxviii pp

ISBN: 978-3-95806-588-8

Band / Volume 75

Development of Electrochemical Aptasensors for the Highly Sensitive, Selective, and Discriminatory Detection of Malaria Biomarkers

G. Figueroa Miranda (2021), XI, 135 pp

ISBN: 978-3-95806-589-5

Band / Volume 76

Nanostraw- Nanocavity MEAs as a new tool for long-term and high sensitive recording of neuronal signals

P. Shokoohimehr (2021), xi, 136 pp

ISBN: 978-3-95806-593-2

Band / Volume 77

Surface plasmon-enhanced molecular switching for optoelectronic applications

B. Lenyk (2021), x, 129 pp

ISBN: 978-3-95806-595-6

Band / Volume 78

Engineering neuronal networks in vitro: From single cells to population connectivity

I. Tihaa (2021), viii, 242 pp

ISBN: 978-3-95806-597-0

Band / Volume 79

Spectromicroscopic investigation of local redox processes in resistive switching transition metal oxides

T. Heisig (2022), vi, 186 pp

ISBN: 978-3-95806-609-0

Band / Volume 80

Integrated Control Electronics for Qubits at Ultra Low Temperature

D. Nielinger (2022), xviii, 94, xix-xxvi

ISBN: 978-3-95806-631-1

Band / Volume 81

Higher-order correlation analysis in massively parallel recordings in behaving monkey

A. Stella (2022), xiv, 184 pp

ISBN: 978-3-95806-640-3

Band / Volume 82

Denoising with Quantum Machine Learning

J. Pazem (2022), 106 pp

ISBN: 978-3-95806-641-0

Band / Volume 83

Hybrid hydrogels promote physiological functionality of long-term cultured primary neuronal cells in vitro

C. Meeßen (2022), x, 120 pp

ISBN: 978-3-95806-643-4

Band / Volume 84

Surface states and Fermi-level pinning on non-polar binary and ternary (Al,Ga)N surfaces

L. Freter (2022), 137 pp

ISBN: 978-3-95806-644-1

Weitere *Schriften des Verlags im Forschungszentrum Jülich* unter
<http://wwwzb1.fz-juelich.de/verlagextern1/index.asp>

Information

Band / Volume 84

ISBN 978-3-95806-644-1